On the mechanisms of superfluidity in atomic nuclei

A. V. Avdeenkov and S. P. Kamerdzhiev*[)]

Physics and Power Engineering Institute State Science Center of the Russian Federation, 249020 Obninsk, Kaluga Region, Russia

A system of equations is obtained for the Cooper gap in nuclei. The system takes two mechanisms of superfluidity into account in an approximation quadratic in the phonon-production amplitude: a Bardeen–Cooper–Schrieffer (BCS)-type mechanism and a quasiparticle–phonon mechanism. These equations are solved for ^{120}Sn in a realistic approximation. If the simple procedures proposed are used to determine the new particle–particle interaction and to estimate the average effect, then the contribution of the quasiparticle–phonon mechanism to the observed width of the pairing gap is 26% and the BCS-type contribution is 74%. This means that at least in semimagic nuclei pairing is of a mixed nature — it is due to the two indicated mechanisms, the first being mainly a surface mechanism and the second mainly a volume mechanism. © *1999 American Institute of Physics.*
[S0021-3640(99)00110-3]

PACS numbers: 21.60.−n, 74.20.Fg, 67.20.+k

In the microscopic theory of ordinary superconductors the Éliashberg theory,[1] in which the interaction of the electrons that leads to pairing is due to the exchange of phonons, describes the mechanism of superconductivity quite well. In the weak electron–phonon interaction limit $g^2 \ll 1$ this mechanism reduces to the well-known Bardeen–Cooper–Schrieffer (BCS) model.

The situation is somewhat different in the microscopic theory of nuclei with pairing (nonmagic nuclei). As a rule, the width of the superfluid gap is determined experimentally or calculated using the BCS equation with a phenomenologically chosen particle–particle (pp) interaction.[2,3] This interaction and therefore the gap are energy-independent. In other words the quasiparticle–phonon interaction (QPI) in the problem of pairing in nuclei is taken into account only effectively — to the extent that the quasiparticle–phonon pairing mechanism can be reduced to the indicated BCS mechanism. This would be justified if $g^2 \ll 1$, where g is the phonon production amplitude, in nuclei. In nuclei with pairing, however, $g^2 > 1$ can occur in each of the two nucleon systems because of the existence of a low-lying 2^+ collective level.[4] In nuclei with pairing the weak inequality $g^2 < 1$ can occur in one of the nucleon systems (semimagic nuclei; see calculations in Ref. 5 for ^{120}Sn). Therefore the quasiparticle–phonon pairing mechanism must be examined explicitly, and it is of interest to study the realistic case $g^2 < 1$ first.

It is well known that the most highly collective low-lying phonons, which make the largest contribution to QPI effects in nuclei, are mainly surface oscillations. For this reason, singling out the quasiparticle–phonon pairing mechanism explicitly will make it possible to answer the old question of whether pairing in nuclei is a volume or surface effect. This question has been discussed in Ref. 6 at the phenomenological level — introducing the ''internal'' F_{in}^{ξ} and ''external'' F_{ex}^{ξ} pp-interaction amplitudes — on the basis of the theory of finite Fermi systems, where it was found that for Sn isotopes pairing is primarily a volume effect. The question of the nature of pairing has been raised in Ref. 7 at the microscopic level.

It has been found that it is important to take into account the QPI in the particle–hole channel in order to gain a quantitative and a qualitative understanding of many nuclear phenomena, above all for describing excitations of nuclei.[3,4,8] A systematic allowance for the QPI in the pp channel, including for the pairing problem, should improve the description of at least the low-lying excitations in odd-mass nuclei (see Ref. 5, where this is shown quantitatively) and in even-even nuclei with pairing. This is especially important now in connection with the advent of qualitatively new experimental possibilities in EUROBALL γ spectrometers, which are now in operation in Europe and the USA.[9]

In Fermi systems with superfluidity it is necessary to use, besides the standard single-particle Green's functions G and $G^{(h)}$, the anomalous single-particle Green's functions $F^{(1)}$ and $F^{(2)}$. For a realistic description the well-known components, i.e., the mean field and pairing, described by a BCS-type equation, should be singled out explicitly, after which corrections to first order in g^2 in all mass operators should be studied. This problem, i.e., the formulation of the gap equations in the g^2 approximation, is studied in the first part of this letter. The first computational results for ^{120}Sn are presented in the second part.

We shall represent each of the complete mass operators in the system of equations for G and F as a sum of two terms, the first being energy-independent and the second energy-dependent

$$\Sigma(\varepsilon)=\widetilde{\Sigma}+M(\varepsilon), \quad \Sigma^{(h)}(\varepsilon)=\widetilde{\Sigma}^{(h)}+M^{(h)}(\varepsilon), \tag{1}$$

$$\Sigma^{(1)}(\varepsilon)=\widetilde{\Sigma}^{(1)}+M^{(1)}(\varepsilon), \quad \Sigma^{(2)}(\varepsilon)=\widetilde{\Sigma}^{(2)}+M^{(2)}(\varepsilon),$$

where $\widetilde{\Sigma}$ and $\widetilde{\Sigma}^{(h)}$ correspond to the mean field and $\widetilde{\Sigma}^{(1)}$ and $\widetilde{\Sigma}^{(2)}$ correspond to pairing, described by a BCS-type mechanism. The quantities M^i contain the QPI explicitly and are taken in the g^2 approximation:

$$M(\varepsilon) = M^{(h)}(-\varepsilon) = \text{}, \tag{2}$$

$$M^{(1)}(\varepsilon) = \text{}, \quad M^{(2)}(\varepsilon) = \text{}, \tag{3}$$

where a circle denotes the phonon production amplitude g and the Green's functions in the mass operators M^i do not contain phonons. Pair phonons are neglected here and below, since their contribution should be small.

In what follows it should be kept in mind that the initial components of the problem are the mean field, described by the phenomenological Woods–Saxon potential, and the

gap width, which satisfies the BCS equation with a phenomenologically chosen *pp* inter-action. At present this approach is the most realistic in the theory of nuclei, especially for describing experiments for nonmagic nuclei.

On account of the phenomenological nature of the input quantities — the single-particle energies ε_λ and the gap widths Δ_λ (λ denotes the single-particle quantum numbers), the energies ε_λ should contain a contribution from the terms M,[10] and the quantities $\Delta_\lambda^{(1),(2)}$ should contain a contribution due to the terms $M^{(1),(2)}$. The latter can be seen from the standard BCS equation with a phenomenological *pp* interaction, written in terms of the Green's functions method,[2]

$$\Delta_\lambda^{(2)} = \Delta_\lambda^{(1)} = \sum_{\lambda'} F_{\lambda\bar{\lambda}\lambda'\bar{\lambda}'}^\xi F_{\lambda'}^{(2)};\tag{4}$$

where $F_{\lambda'}^{(2)}$ is the anomalous Gor'kov–Green's function and F^ξ is the renormalized interaction amplitude, which is irreducible in the *pp* channel. Therefore F^ξ contains diagrams corresponding to phonon exchange, i.e., we can write[7,11] (symbolically)

$$F^\xi = W + gDg,\tag{5}$$

where W is a new *pp* interaction and D is the phonon Green's function. Then, singling out the pole diagram with a phonon in Eq. (5), according to Eq. (4), corresponds to taking $M^{(2)}$ from Eq. (3) into account in Eq. (1). Therefore, in order to avoid taking the quantities M^i into account twice they must be excluded from the phenomenological quantities, i.e., the QPI must be ''removed'' from the latter. These refined quantities are everywhere marked with a tilde.

The system of equations for the single-particle Green's functions in our g^2 approximation has the (symbolic) form[5,12]

$$G = \tilde{G} + \tilde{G}MG - \tilde{F}^{(1)}M^{(h)}F^{(2)} - \tilde{G}M^{(1)}F^{(2)} - \tilde{F}^{(1)}M^{(2)}G,\tag{6}$$

$$F^{(2)} = \tilde{F}^{(2)} + \tilde{F}^{(2)}MG + \tilde{G}^{(h)}M^{(h)}F^{(2)} - \tilde{F}^{(2)}M^{(1)}F^{(2)} + \tilde{G}^{(h)}M^{(2)}G,$$

where $\tilde{G}$ and $\tilde{F}^{(2)}$ are the well-known Gor'kov Green's functions, which, in contrast to the standard case,[2,3] contain $\tilde{\varepsilon}$ and $\tilde{\Delta}$ from which the contributions of the corresponding M^i have been removed.

Next, following Ref. 7 we represent the mass operators M and $M^{(h)}$ as a sum of parts which are even and odd as a function of energy, for example, $M = M_{(e)} + M_{(o)}$. Then, determining the excitations of an odd-mass nucleus as the poles of the Green's functions, we obtain from the system (6) the formal expression for these energies[5]

$$E_{\lambda\eta} = \sqrt{\varepsilon_{\lambda\eta}^2 + \Delta_{\lambda\eta}^2},\tag{7}$$

where

$$\varepsilon_{\lambda\eta} = \frac{\tilde{\varepsilon}_\lambda + M_{(e)\lambda}(E_{\lambda\eta})}{1 + q_{\lambda\eta}} \quad \text{and} \quad \Delta_{\lambda\eta} = \frac{\tilde{\Delta}_\lambda + M_\lambda^{(1,2)}(E_{\lambda\eta})}{1 + q_{\lambda\eta}},\tag{8}$$

and $q_{\lambda\eta} = -M_{(o)\lambda}(E_{\lambda\eta})/E_{\lambda\eta}$. Here the index η is the number of the solution of the system (7)–(8). Here the difference from Ref. 7 lies in the fact that by introducing the unobservable, or refined, quantities $\tilde{\varepsilon}_\lambda$ and $\tilde{\Delta}_\lambda$ we avoid taking the M^i into account twice.

A relation between the phenomenological and refined quantities can be obtained from relations (7) and (8). Since the experimental single-quasi-particle energies which we are using should correspond to the dominant (having the maximum spectroscopic factor) levels, the refinement should be such that after the Dyson equations (6) are solved one solution should correspond to an experimental value and the level should remain dominant. These experimental single-quasi-particle energies serve as input data for our entire problem. Using this condition and relations (8) we obtain

$$\varepsilon_\lambda = \frac{\widetilde{\varepsilon}_\lambda + M_{(e)\lambda}(E_\lambda)}{1 + q_\lambda(E_\lambda)}, \quad \Delta_\lambda \equiv \Delta_\lambda^{(1,2)} = \frac{\widetilde{\Delta}_\lambda + M_\lambda^{(1,2)}(E_\lambda)}{1 + q_\lambda(E_\lambda)}, \tag{9}$$

where $E_\lambda = \sqrt{\varepsilon_\lambda^2 + \Delta_\lambda^2}$. The energies $\widetilde{\varepsilon}_\lambda$ and ε_λ in Eqs. (7)–(9) are measured from the corresponding chemical potential $\widetilde{\mu}$ or μ. Solving these nonlinear equations, we can find the refined $\widetilde{\varepsilon}_\lambda$ and $\widetilde{\Delta}_\lambda$, if the phenomenological ε_λ and Δ_λ are known.

We shall now obtain an equation for $\widetilde{\Delta}_\lambda$. For this, since in the limit of no QPI ($M^i = 0$) $\Sigma^{(1,2)}$ becomes the standard BCS gap, and generalizing the corresponding analysis in the theory of finite Fermi systems[2] [see Eq. (4)], we write the mass operator as

$$\Sigma^{(1,2)} = \bar{F}^\xi F^{(1,2)}, \tag{10}$$

where $F^{(1,2)}$ satisfies the system of the equations (6). Here $\bar{F}^\xi$ is the amplitude, which is irreducible in the pp channel and should differ from $F^{(\xi)}$ in Eq. (4), since the Green's functions in Eqs. (4) and (10) are different. It can also be represented as a sum of two parts, similar to Eq. (5),

$$\bar{F}^\xi = \bar{W} + gDg. \tag{11}$$

The interaction $\bar{W}$ is assumed to be energy-independent. The Green's function $F^{(2)}$ in Eq. (10) must also be taken in the g^2 approximation [first iteration in Eq. (6)]:

$$F^{(2)} \approx \widetilde{F}^{(2)} + \widetilde{F}^{(2)} M \widetilde{G} + \widetilde{G}^{(h)} M^{(h)} \widetilde{F}^{(2)} - \widetilde{F}^{(2)} M^{(1)} \widetilde{F}^{(2)} + \widetilde{G}^{(h)} M^{(2)} \widetilde{G}. \tag{12}$$

From relations (10)–(12), dropping terms of order higher than $g^{(2)}$, we obtain

$$\Sigma^{(2)}(\varepsilon) = W \widetilde{F}^{(2)} + gDg \widetilde{F}^{(2)} + W(\widetilde{F}^{(2)} M \widetilde{G} + \widetilde{G}^{(h)} M^{(h)} \widetilde{F}^{(2)}$$

$$- \widetilde{F}^{(2)} M^{(1)} \widetilde{F}^{(2)} + \widetilde{G}^{(h)} M^{(2)} \widetilde{G}) \equiv \bar{\Delta} + M^{(2)}. \tag{13}$$

Comparing Eqs. (1) and (13) we see that $\bar{\Delta} = \widetilde{\Delta}^{(2)}$, i.e., the refined $\widetilde{\Delta}^{(2)}$ introduced above satisfies the nonlinear equation

$$\widetilde{\Delta}^{(2)} = W(\widetilde{F}^{(2)} + W \widetilde{F}^{(2)} M \widetilde{G} + \widetilde{G}^{(h)} M^{(h)} \widetilde{F}^{(2)} - \widetilde{F}^{(2)} M^{(1)} \widetilde{F}^{(2)} + \widetilde{G}^{(h)} M^{(2)} \widetilde{G}). \tag{14}$$

The terms with M^i in Eq. (14) give the desired contribution of the QPI to $\widetilde{\Delta}$, and the term $\widetilde{\Delta}_{\text{BCS}} \equiv \bar{W} \widetilde{F}^{(2)}$ describes the BCS pairing mechanism but with an interaction $\bar{W}$ that is different from $F^{(\xi)}$ in Eq. (4).

Therefore two problems must be solved in order to take the QPI into account completely (in the g^2 approximation) in the problem of pairing in nuclei: 1) $\widetilde{\Delta}_\lambda$ must be found from the system of equations (9), having determined first the quantities ε_λ and Δ_λ from

experiment, and 2) Eq. (14) must be solved for $\widetilde{\Delta}_\lambda$ or, more precisely, knowing these quantities, we must find the interaction $\bar{W}$ and thereby determine the contribution of terms with and without phonons to $\widetilde{\Delta}_\lambda$.

We have performed the corresponding calculations for the semimagic ^{120}Sn nucleus. First, using an iterative fitting procedure, the phenomenological ε_λ and Δ_λ were determined, starting from existing experimental data for the neighboring ^{119}Sn and ^{121}Sn nuclei (see Ref. 5). The equation (4) was solved using the phenomenological pp interaction obtained in Ref. 6: $F^\xi = -C_0/\ln(c_p/\xi)$, where ξ is the cutoff parameter for summation in the range $\xi - \mu < \varepsilon_\lambda < \xi + \mu$. To solve the system (9) and Eq. (14) we used 21 of the most collective 2^+, 3^-, 4^+, 5^-, and 6^+ phonons with energy not exceeding the neutron binding energy, which we calculated for ^{120}Sn on the basis of the theory of finite Fermi systems[2] (see Ref. 5 for more detailed discussion). On account of computational difficulties in solving the indicated nonlinear equations, the calculations were performed for eight single-particle neutron levels from $1g9/2$ to $3p3/2$ near the Fermi surface. However, this restriction is quite reasonable, since the contribution of the QPI is greatest precisely for such levels.

Determining the parameters of the new interaction $\bar{W}$ in Eq. (14) is a separate and very complicated problem, even if $\bar{W}$ is found from the condition that the quantities $\widetilde{\Delta}_\lambda$ obtained from the system (9) are identical to the values obtained by solving Eq. (14). For this reason, here we used the simplest method. The interaction $\bar{W}$ was taken in the same functional form[6] as in Eq. (4), but the parameter c_p was determined from the condition that the average values $\bar{\bar{\Delta}}$ found by solving the system (6) and Eq. (14) are the same. The averaging was done according to the formula

$$\bar{\bar{\Delta}} = \frac{\Sigma_j \widetilde{\Delta}_\lambda (2j+1)}{\Sigma_j (2j+1)}. \tag{15}$$

We have obtained the following results. The contribution of $\bar{\bar{\Delta}}_{\text{BCS}}$, which characterizes the BCS mechanism with the new interaction $\bar{W}$, is 74% of the average phenomenological gap, which is 1.42 MeV. Therefore the contribution of the quasiparticle–phonon pairing mechanism is 26%. The contribution from the retarded pp interaction due to phonon exchange (the quantity $(\bar{\Delta} - \bar{\bar{\Delta}})/\bar{\Delta}$) is 31%, and the average contribution to $\bar{\bar{\Delta}}$ from diagrams with the QPI which appear in Eq. (14) is -5%. The latter result is obvious: Just as in the case of the particle–hole channel,[8] the contribution of terms corresponding to diagrams with a ''transverse phonon'' (phonon exchange diagram) and with ''inserts'' (self-energy diagram) are opposite in sign. However, the contribution of diagrams with ''inserts'' is small in our case.

The main result of our calculation is that pairing in semimagic nuclei is of a mixed nature. The BCS mechanism with the refined pp interaction makes the largest contribution to the gap width, while the contribution of the quasiparticle–phonon mechanism, which is mainly of a surface nature, is smaller. If the simple recipes proposed are used to determine a new pp interaction and to estimate the effect by averaging according to Eq. (15), then the QPI contribution will be 26% of the gap observed for ^{120}Sn. In any case the result obtained must be taken into account in the microscopic description of modern

experiments studying low-lying excitations in nonmagic nuclei. For odd-mass nuclei this will be shown in Ref. 5 on the basis of a more phenomenological approach than in the present work, where only the system of equations (9) was solved.

S. K. thanks B. Mottelson and G. M. Éliashberg for a discussion of the results obtained in this work.

[1] G. M. Éliashberg, Zh. Éksp. Teor. Fiz. **38**, 966 (1960) [Sov. Phys. JETP **11**, 696 (1960)]; J. P. Carbotte, Rev. Mod. Phys. **62**, 1027 (1990).

[2] A. B. Migdal, *Theory of Finite Fermi Systems and Applications to Atomic Nuclei*, translation of 1st Russian edition (Interscience, New York, 1967) [Russian original, 2nd edition, Nauka, Moscow, 1983].

[3] V. G. Solov'ev, *Theory of Atomic Nuclei — Quasiparticles and Phonons* (Énergoatomizdat, Moscow, 1989).

[4] A. Bohr and B. Mottelson, *Nuclear Structure*, Vol. 2 (Benjamin, New York, 1975) [Russian translation, Mir, Moscow, 1977].

[5] A. V. Avdeenkov and S. P. Kamerdzhiev, Yad. Fiz. **62**, No. 4, 610 (1999) [Phys. At. Nucl. **62**, 563 (1999)].

[6] M. V. Zverev and É. E. Sapershteĭn, Yad. Fiz. **39**, 1390 (1985) [Sov. J. Nucl. Phys. **39**, 878 (1985)].

[7] S. G. Kadmenskiĭ, and P. A. Luk'yanovich, Yad. Fiz. **49**, 384 (1989) [Sov. J. Nucl. Phys. **49**, 238 (1989)].

[8] S. P. Kamerdzhiev, G. Ya. Tertychnyĭ, and V. I. Tselyaev, Fiz. Élemen. Chastits At. Yadra **28**, 333 (1997) [Phys. Part. Nuclei **28**, 134 (1997)].

[9] Progr. Part. Nucl. Phys. **38**, edited by A. Faessler (Pergamon Press, New York, 1997).

[10] S. P. Kamerdzhiev, JETP Lett. **30**, 500 (1979); Yad. Fiz. **38**, 316 (1983) [Sov. J. Nucl. Phys. **38**, 188 (1983)].

[11] F. J. W. Hahne, W. D. Heiss, and C. A. Engelbrecht, Ann. Phys. **104**, 251 (1977).

[12] S. P. Kamerdzhiev, Yad. Fiz. **60**, No. 3, 572 (1997) [Phys. At. Nucl. **60**, 497 (1997)].

Translated by M. E. Alferieff

Flavored multiskyrmions

V. B. Kopeliovich

Institute for Nuclear Research, 117312 Moscow, Russia

W. J. Zakrzewski

Department of Mathematical Sciences, University of Durham, DH1 3LE, UK

Static properties of multiskyrmions with baryon numbers up to 8 are calculated on the basis of the recently given rational map Ansätze. The spectra of baryonic systems with strangeness, charm, and bottom are considered within a ''rigid oscillator'' version of the bound state soliton model. It is suggested that the recently observed negatively charged nuclear fragment can be considered as a quantized strange multiskyrmion with $B=6$ or 7. In agreement with previous observations, baryonic systems with charm or bottom have a better chance of being bound by the strong interactions than do strange baryonic systems. © *1999 American Institute of Physics.* [S0021-3640(99)00210-8]

PACS numbers: 12.39.Dc

1. The topological soliton models, and the Skyrme model among them, are attractive because of their simplicity and the possibility that they may give a good description of various properties of low-energy baryons. The models of this kind provide also a very good framework within which to investigate the possible existence of nuclear matter fragments with unusual properties, such as their flavor being different from u and d quarks. In addition to being important by itself, this issue can have consequences in astrophysics and cosmology. It is well known that the relativistic many-body problem cannot be solved directly using the existing methods, and the chiral soliton approach may make it possible to overcome some of these difficulties.

The description of skyrmions with large baryon numbers is complicated because the explicit form of the fields is not known. The recent remarkable observation[2] that the fields of the $SU(2)$ skyrmions can be approximated accurately by rational map Ansätze giving values of masses close to their exact values has considerably simplified their study. Similar Ansätze have also been recently presented for $SU(N)$ skyrmions (which are not embeddings of $SU(2)$ fields).[3]

Here we use the $SU(2)$ rational map Ansätze as the starting points for calculating the static properties of bound states of skyrmions, which are needed for their quantization in the space of $SU(3)$ collective coordinates. The energy and baryon number densities of the $B=3$ configuration have tetrahedral symmetry, those for $B=4$ have octahedral (cubic) symmetry,[4] those for $B=5$ — D_{2d} symmetry, for $B=6$ — D_{4d} symmetry, for $B=7$ — dodecahedral symmetry, for $B=8$ — D_{6d} symmetry,[5,2] etc. A minimization with the help

of a three-dimensional variational $SU(3)$ program[6] lowers the energies of these configurations by a few hundred MeV and shows that they are local minima in the $SU(3)$ configuration space. The knowledge of the ''flavor'' moment of inertia and the Σ term then allows us to estimate the flavor excitation energies. The mass splittings of the lowest states with different values of strangeness, charm, or bottom are calculated within the rigid oscillator version of the bound-state approach. The binding energies of baryonic systems with different flavors are also estimated.

2. Let us consider simple $SU(3)$ extentions of the Skyrme model:[1] we start with $SU(2)$ skyrmions (with flavor corresponding to (u,d) quarks) and extend them to various $SU(3)$ groups, (u,d,s), (u,d,c), or (u,d,b). We take the Lagrangian density of the Skyrme model, which in its well-known form depends on parameters F_π, F_D, and e and can be written in the following way:[7]

$$
\mathcal{L} = \frac{F_\pi^2}{16}\,\mathrm{Tr}\,l_\mu l^\mu + \frac{1}{32e^2}\,\mathrm{Tr}[l_\mu, l_\nu]^2 + \frac{F_\pi^2 m_\pi^2}{16}\,\mathrm{Tr}(U + U^\dagger - 2) + \frac{F_D^2 m_D^2 - F_\pi^2 m_\pi^2}{24}
$$

$$
\times \mathrm{Tr}(1 - \sqrt{3}\lambda_8)(U + U^\dagger - 2) + \frac{F_D^2 - F_\pi^2}{48}\,\mathrm{Tr}(1 - \sqrt{3}\lambda_8)(U l_\mu l^\mu + l_\mu l^\mu U^\dagger). \quad (1)
$$

where $U \in SU(3)$ is a unitary matrix incorporating chiral (meson) fields, and $l_\mu = U^\dagger \partial_\mu U$. In this model F_π is fixed at the physical value: $F_\pi = 186\,\mathrm{MeV}$. M_D is the mass of a K, D or B meson.

The flavor symmetry breaking in the Lagrangian is of the usual form, and has proved sufficient for describing the mass splittings of the octet and decuplets of baryons.[7] The Wess–Zumino term, not shown here, plays an important role in the quantization procedure, but it does not contribute to the static masses of classical configurations.[8]

We begin our calculations with $U \in SU(2)$, as was mentioned above. The classical mass of $SU(2)$ solitons, in the most general case, depends on 3 profile functions: f, α, and β. Here we use the following general parametrization of U_0 for an $SU(2)$ soliton: $U_0 = c_f + s_f \boldsymbol{\tau} \cdot \mathbf{n}$ with $n_z = c_\alpha$, $n_x = s_\alpha c_\beta$, $n_y = s_\alpha s_\beta$, $s_f = \sin f$, $c_f = \cos f$, etc.

The masses of solitons, moments of inertia, Γ and $\bar{\Gamma}$ are presented in Table I.

The flavor moment of inertia enters directly in the quantization procedure,[9–17] and for arbitrary $SU(2)$ skyrmions is given by[15,17]

$$
\Theta_F = \frac{1}{8}\int (1 - c_f)\left[F_D^2 + \frac{1}{e^2}((\boldsymbol{\partial}f)^2 + s_f^2(\boldsymbol{\partial}\alpha)^2 + s_f^2 s_\alpha^2(\boldsymbol{\partial}\beta)^2)\right]d^3\mathbf{r}. \quad (2)
$$

It is simply connected with $\Theta_F^{(0)}$ for the flavor symmetric case: $\Theta_F = \Theta_F^{(0)} + (F_D^2/F_\pi^2 - 1)\Gamma/4$, where Γ is defined in (3) below. The isotopic moments of inertia are the components of the corresponding tensor of inertia,[9,10] in our case this tensor of inertia is close to the unit matrix multiplied by Θ_T. The quantization procedure uses the quantities Γ (or the Σ term), which determines the contribution of the mass term to the classical mass of the solitons, and $\bar{\Gamma}$:

$$
\Gamma = \frac{F_\pi^2}{2}\int (1 - c_f)d^3\mathbf{r}, \quad (3)
$$

TABLE I.

B	$M_{\text{cl.}}$	$\Theta_F^{(0)}$	Θ_T	Γ	$\tilde{\Gamma}$	ω_s	ω_c	ω_b	$\Delta\epsilon_s$	$\Delta\epsilon_c$	$\Delta\epsilon_b$
1	1.702	2.04	5.55	4.83	15.6	0.309	1.542	4.82	—	—	—
3	4.80	6.34	14.4	14.0	26.7	0.289	1.504	4.75	-0.041	-0.01	0.03
4	6.20	8.27	16.8	18.0	31.4	0.283	1.493	4.74	-0.020	0.019	0.06
5	7.78	10.8	23.5	23.8	35.3	0.287	1.505	4.75	-0.027	0.006	0.05
6	9.24	13.1	25.4	29.0	38.2	0.287	1.504	4.75	-0.019	0.017	0.05
7	10.6	14.7	28.7	32.3	44.4	0.282	1.497	4.75	-0.017	0.021	0.06
8	12.2	17.4	33.4	38.9	46.9	0.288	1.510	4.77	-0.018	0.014	0.02

Characteristics of the bound states of skyrmions with baryon numbers up to $B=8$. The classical mass $M_{\text{cl.}}$ of solitons is in GeV, the moments of inertia Γ and $\tilde{\Gamma}$ are in GeV^{-1}, the excitation frequencies ω_F for flavor F are in GeV. The parameters of the model are $F_\pi=186$ MeV, $e=4.12$. The accuracy of the calculations is better than 1% for the masses and a few % for the other quantities. The $B=1$ quantities are shown for comparison. $\Delta\epsilon_{s,c,b}$, in GeV, are the changes of binding energies of the lowest baryonic system with flavor s, c, or b, $|F|=1$, in comparison with usual (u,d) nuclei (see Eq. (14)).

$$\tilde{\Gamma} = \frac{1}{4}\int c_f[(\boldsymbol{\partial}f)^2 + s_f^2(\boldsymbol{\partial}\alpha)^2 + s_f^2 s_\alpha^2(\boldsymbol{\partial}\beta)^2]d^3\mathbf{r}. \tag{4}$$

3. To quantize the solitons in $SU(3)$ configuration space, in the spirit of the bound-state approach to the description of strangeness proposed in Refs. 11 and 12 and used in Refs. 13 and 14, we consider the motion, in collective coordinates, of the meson fields incorporated into the matrix U:

$$U(r,t) = R(t)U_0(O(t)\mathbf{r})R^\dagger(t), \quad R(t) = A(t)S(t), \tag{5}$$

where U_0 is the $SU(2)$ soliton embedded into $SU(3)$ in the usual way (into the upper left-hand corner), $A(t) \in SU(2)$ describes $SU(2)$ rotations, $S(t) \in SU(3)$ describes rotations in the "strange," "charm." or "bottom" directions, and $O(t)$ describes rigid rotations in real space;

$$S(t) = \exp(i\mathcal{D}(t)), \quad \mathcal{D}(t) = \sum_{a=4,\ldots7} D_a(t)\lambda_a, \tag{6}$$

λ_a are Gell-Mann matrices of the (u,d,s), (u,d,c) or (u,d,b) $SU(3)$ groups. The (u,d,c) and (u,d,b) $SU(3)$ groups are quite analogous to the (u,d,s) group. For the (u,d,c) group a simple redefinition of hypercharge should be made. For the (u,d,s) group, $D_4=(K^+ + K^-)/\sqrt{2}$, $D_5=i(K^+ - K^-)/\sqrt{2}$, etc. And for the (u,d,c) group $D_4=(D^0 + \bar{D}^0)/\sqrt{2}$, etc.

The angular velocities of the isospin rotations are defined in the standard way: $A^\dagger \dot{A} = -i\boldsymbol{\omega\tau}/2$. We shall not consider the ordinary spatial rotations explicitly here because the corresponding moments of inertia for baryonic systems are much greater than the isospin moments of inertia, and for the lowest possible values of the angular momentum J the corresponding quantum correction is either exactly zero (for even B) or small.

The field D is small in magnitude, at most of order $1/\sqrt{N_c}$, where N_c is the number of colors in QCD. Therefore, an expansion of the matrix S in D can be made safely. To the lowest order in field D the Lagrangian of the model (1) can be written as

$$L = -M_{cl,B} + 4\Theta_{F,B}\dot{D}^\dagger\dot{D} - \left[\Gamma_B\left(\frac{F_D^2}{F_\pi^2}m_D^2 - m_\pi^2\right)\right.$$

$$\left. + \tilde{\Gamma}_B(F_D^2 - F_\pi^2)\right]D^\dagger D - i\frac{N_c B}{2}(D^\dagger\dot{D} - \dot{D}^\dagger D). \tag{7}$$

Here and below D is the doublet K^+, K^0 (D^0, D^-, or B^+, B^0). We have kept the standard notation for the moment of inertia of the rotation into the ''flavor'' direction $\Theta_F = \Theta_s$, Θ_c or Θ_b (Refs. 10 and 15) (the index c denotes the charm quantum number, except in N_c). The contribution proportional to $\tilde{\Gamma}_B$ is suppressed in comparison with the term $\sim\Gamma$ by the small factor $\sim F_D^2/m_D^2$, and is more important for strangeness. The term proportional to $N_c B$ in (7) arises from the Wess–Zumino term in the action and is responsible for the difference of the excitation energies of strangeness and antistrangeness (flavor and antiflavor in the general case).[13,14]

Following the canonical quantization procedure, we write the Hamiltonian of the system, including the terms of order N_c^0, in the form:[11,12]

$$H_B = M_{cl,B} + \frac{1}{4\Theta_{F,B}}\Pi^\dagger\Pi + \left(\Gamma_B\bar{m}_D^2 + \tilde{\Gamma}_B(F_D^2 - F_\pi^2) + \frac{N_c^2 B^2}{16\Theta_{F,B}}\right)D^\dagger D$$

$$+ i\frac{N_c B}{8\Theta_{F,B}}(D^\dagger\Pi - \Pi^\dagger D); \tag{8}$$

$\bar{m}_D^2 = (F_D^2/F_\pi^2)m_D^2 - m_\pi^2$. The momentum Π is canonically conjugate to the variable D. Equation (8) describes an oscillator-type motion of the field D in the background formed by the (u,d) $SU(2)$ soliton. After diagonalization, which can be done explicitly following Refs. 13 and 14, the normal-ordered Hamiltonian can be written as

$$H_B = M_{cl,B} + \omega_{F,B}a^\dagger a + \bar{\omega}_{F,B}b^\dagger b + O(1/N_c), \tag{9}$$

where $a^\dagger$, $b^\dagger$ are the creation operators for the strangeness (i.e., antikaons) and anti-strangeness (flavor and antiflavor) quantum numbers, and $\omega_{F,B}$, $\bar{\omega}_{F,B}$ are the frequencies of flavor (antiflavor) excitations. D and Π are connected with a and b in the following way:[13,14]

$$D^i = (b^i + a^{\dagger i})/\sqrt{N_c B\mu_{F,B}}, \quad \Pi^i = \sqrt{N_c B\mu_{F,B}}(b^i - a^{\dagger i})/2i \tag{10}$$

with $\mu_{F,B} = [1 + 16(\bar{m}_D^2\Gamma_B + (F_D^2 - F_\pi^2)\tilde{\Gamma}_B)\Theta_{F,B}/(N_c B)^2]^{1/2}$. For the lowest states the values of D are small, $D \sim [16\Gamma_B\Theta_{F,B}\bar{m}_D^2 + N_c^2 B^2]^{-1/4}$, and increase with increasing flavor number $|F|$ as $(2|F|+1)^{1/2}$. As was noted in Ref. 14, deviations of the field D from the vacuum decrease with increasing mass m_D, as well as with increasing number of colors N_c, and the method works for any m_D (and also for charm and bottom quantum numbers).

The excitation frequencies ω and $\bar{\omega}$ are:

$$\omega_{F,B}=N_c B(\mu_{F,B}-1)/8\Theta_{F,B}, \quad \bar\omega_{F,B}=N_c B(\mu_{F,B}+1)/8\Theta_{F,B}. \tag{11}$$

As was observed in Ref. 15, the difference $\bar\omega_{F,B}-\omega_{F,B}=N_c B/4\Theta_{F,B}$ coincides, to leading order in N_c, with the expression obtained in the collective-coordinates approach.[16]

The flavor symmetry breaking in the flavor decay constants, i.e., the fact that $F_K/F_\pi\simeq 1.22$ and $F_D/F_\pi=1.7\pm 0.2$ (we take $F_D/F_\pi=1.5$ and $F_B/F_\pi=2$) leads to an increase in the flavor excitation frequencies, in better agreement with data for charm and bottom.[18] It also leads to some increase of the binding energies of baryonic systems.[15]

The behavior of static characteristics of multiskyrmions and flavor excitation frequencies shown in Table I is similar to that obtained in Ref. 19 for toroidal configurations with $B=2,3,4$. The flavor inertia increases with B almost proportionally to B. The frequencies ω_F are smaller for $B\geqslant 3$ than for $B=1$.

4. The terms of order N_c^{-1} in the Hamiltonian, which depend on the angular velocities of rotations in the isospin and ordinary spaces and which describe the zero-mode contributions are not crucial but are still important for numerical estimates of the spectra of baryonic systems.

In the rigid oscillator model the states predicted do not correspond to the definite $SU(3)$ or $SU(4)$ representations. How this can be remedied was shown in Ref. 14. For example, the state with $B=1$, $|F|=1$, $I=0$ should belong to the octet of (u,d,s), or (u,d,c), $SU(3)$ group, if $N_c=3$.

Here we consider quantized states of baryonic systems which belong to the lowest possible $SU(3)$ irreps (p,q), $p+2q=3B$, viz., $p=0$, $q=3B/2$ for even B, and $p=1$, $q=(3B-1)/2$ for odd B. For $B=3$, 5, and 7 they are 35-, 80-, and 143-plets, and for $B=4$, 6, and 8 they are 28-, 55- and 91-plets. Since we are interested in the lowest energy states, here we discuss the baryonic systems with the lowest allowed angular momentum, i.e., $J=0$, for $B=4$, 6, and 8. For odd B the quantization of the baryonic system meets with some difficulties, but the correction to the energy of quantized states due to the nonzero angular momentum is small and decreases with increasing B, since the corresponding moment of inertia increases in proportion to $\sim B^2$. Moreover, the J-dependent correction to the energy cancels out in the quantities of interest, which are the energy differences of flavored and flavorless states.

For the energy difference between the state with flavor F belonging to the (p,q) irrep and the ground state with $F=0$ and the same angular momentum and (p,q), we obtain:

$$\Delta E_{B,F}=|F|\omega_{F,B}+\frac{\mu_{F,B}-1}{4\mu_{F,B}\Theta_{F,B}}[I(I+1)-T_r(T_r+1)]+\frac{(\mu_{F,B}-1)(\mu_{F,B}-2)}{4\mu_{F,B}^2\Theta_{F,B}}I_F(I_F+1), \tag{12}$$

$T_r=p/2$ is the quantity analogous to the "right" isospin T_r in the collective-coordinates approach,[9,10] and $\mathbf{T}_r=\mathbf{I}_{bf}-\mathbf{I}_F$. Clearly, the binding energy of multiskyrmions cancels out in Eq. (12). For the states with maximal isospin $I=T_r+|F|/2$ the energy difference can be simplified to:

$$\Delta E_{B,F}=|F|\left[\omega_{F,B}+T_r\frac{\mu_{F,B}-1}{4\mu_{F,B}\Theta_{F,B}}+\frac{(|F|+2)}{8\Theta_{F,B}}\frac{(\mu_{F,B}-1)^2}{\mu_{F,B}^2}\right]. \tag{13}$$

This difference depends on the flavor moment of inertia but not on Θ_T. In the case of antiflavor excitations we have the same formulas, with the substitution $\mu \to -\mu$. For the lowest $SU(3)$ irreps one has $T_r = 0$ for even B and $T_r = 1/2$ for odd B. It follows from (12) and (13) that when some nucleons are replaced by flavored hyperons in baryonic systems the binding energy of the system changes by

$$\Delta\epsilon_{B,F} = |F| \left[\omega_{F,1} - \omega_{F,B} - \frac{3(\mu_{F,1}-1)}{8\mu_{F,1}^2\Theta_{F,1}} - T_r\frac{\mu_{F,B}-1}{4\mu_{F,B}\Theta_{F,B}} - \frac{(|F|+2)}{8\Theta_{F,B}}\frac{(\mu_{F,B}-1)^2}{\mu_{F,B}^2} \right]. \quad (14)$$

For strangeness Eq. (14) is negative, indicating that stranglets should have binding energies smaller than those of nuclei, or can be unbound. Since $\Theta_{F,B}$ increases with increasing B and m_D, this leads to stronger binding with increasing B and ''flavor'' mass, in agreement with Ref. 15. For charm and bottom expression (14) is positive for $B \geqslant 3$; see Table I for the case $|F| = 1$.

The nuclear fragments with sufficiently large values of strangeness (or bottom) can be found in experiments as fragments with negative charge Q, according to the well known relation $Q = T_3 + (B+S)/2$ (similarly for the bottom number). One event of a long lived nuclear fragment with mass about 7.4 GeV was reported in Ref. 20. Using the above formulas it is not difficult to establish that this fragment can be the state with $B = -S = 6$, or $B = 7$ and strangeness $S = -3$. Greater values of strangeness are not excluded.

As in the $B = 1$ case,[21] the absolute values of the masses of multiskyrmions are controlled by the poorly known loop corrections to the classic masses, or the Casimir energy. And as was done for the $B = 2$ states,[16] the renormalization procedure is necessary in order to obtain physically reasonable values of the masses. This generates an uncertainty of around several tens of MeV, as the binding energy of the deuteron is 30 MeV instead of the measured value 2.23 MeV, so ~ 30 MeV characterizes the uncertainty of our approach.[16,17] But this uncertainty is cancelled in the binding energy differences $\Delta\epsilon$ shown in Table I.

5. Using rational map Ansätze as starting configurations, we have calculated the static characteristics of bound skyrmions with baryon numbers up to 8. The excitation frequencies for different flavors — strangeness, charm, and bottom — have been calculated using a rigid-oscillator version of the bound-state approach of the chiral soliton models. This variant of the model overestimates the mass splitting of strange hyperons when flavor symmetry breaking in the decay constant F_K is included, but it works better for c and b flavors.[18] Our previous conclusion that baryonic systems with charm and bottom have better chances to be bound with respect to strong decay than do strange baryonic systems[15] is reinforced by the present investigation. This conclusion takes place also in the case of flavor symmetry, $F_D = F_\pi$.

Consideration of baryonic systems with ''mixed'' flavors is possible in principle but would be technically more involved. Our results agree qualitatively with the results of Ref. 22, where the strangeness excitation frequencies were calculated within the bound-state approach. However, there is a difference in the behavior of the excitation frequencies: we have found that they decrease when the baryon number increases from $B = 1$, thus increasing the binding energy of the corresponding baryonic systems.

The charmed baryonic systems with $B = 3, 4$ were considered in Ref. 23 within a potential approach. The $B = 3$ systems were found to be very near the threshold, and the

$B = 4$ system was found to be stable against strong decay, with a binding energy of $\sim 10\,\mathrm{MeV}$. Further experimental searches for baryonic systems with flavor different from u and d could shed more light on the dynamics of heavy flavors in baryonic systems.

[1] T. H. R. Skyrme, Proc. R. Soc. London, Ser. A **260**, 127 (1961); Nucl. Phys. **31**, 556 (1962).

[2] C. Houghton, N. Manton, and P. Suttcliffe, Nucl. Phys. B **510**, 507 (1998).

[3] T. Ioannidou, B. Piette, and W. J. Zakrzewski, Preprint DTP98/51 UKC98/42.

[4] E. Braaten, S. Townsend, and L. Carson, Phys. Lett. B **235**, 147 (1990).

[5] R. A. Battye and P. M. Sutcliffe, Phys. Lett. B **391**, 150 (1997); Phys. Rev. Lett. **79**, 363 (1997).

[6] V. B. Kopeliovich, B. Schwesinger, and B. E. Stern, JETP Lett. **62**, 185 (1995).

[7] B. Schwesinger, H. Weigel, Phys. Lett. B **267**, 438 (1991); H. Weigel, Int. J. Mod. Phys. A **11**, 2419 (1996).

[8] E. Witten, Nucl. Phys. B **223**, 422; 433 (1983).

[9] G. S. Adkins, C. R. Nappi, and E. Witten, Nucl. Phys. B **228**, 552 (1983); G. S. Adkins and C. R. Nappi, Nucl. Phys. B **233**, 109 (1984); G. Guadagnini, Nucl. Phys. B **236**, 35 (1984).

[10] R. L. Jaffe and C. L. Korpa, Nucl. Phys. B **258**, 468 (1985); A. P. Balachandran *et al.*, Nucl. Phys. B **256**, 525 (1985).

[11] C. G. Callan and I. R. Klebanov, Nucl. Phys. B **262**, 365 (1985).

[12] N. Scoccola *et al.*, Phys. Lett. B **201**, 425 (1988); C. G. Callan, K. Hornbostel, and I. R. Klebanov, Phys. Lett. B **202**, 269 (1988); N. Scoccola *et al.*, Nucl. Phys. A **505**, 497 (1989).

[13] D. Kaplan and I. R. Klebanov, Nucl. Phys. B **335**, 45 (1990).

[14] K. M. Westerberg and I. R. Klebanov, Phys. Rev. D **50**, 5834 (1994); I. R. Klebanov and K. M. Westerberg, Phys. Rev. D **53**, 2804 (1996).

[15] V. B. Kopeliovich, JETP Lett. **67**, 896 (1998); http://xxx.lanl.gov/abs/hep-ph/9805296.

[16] V. B. Kopeliovich, B. Schwesinger, and B. E. Stern, Nucl. Phys. A **549**, 485 (1992); V. B. Kopeliovich, Phys. Lett. B **259B**, 234 (1991).

[17] V. B. Kopeliovich, Nucl. Phys. A **639**, 75c (1998); Zh. Éksp. Teor. Fiz. **112**, 1941 (1997) [JETP **85**, 1060 (1997)]; Yad. Fiz. **56**, No. 8, 160 [Phys. At. Nucl. **56**, 1084 (1993)].

[18] D. O. Riska and N. N. Scoccola, Phys. Lett. B **265**, 188 (1991); M. Bjornberg *et al.*, Nucl. Phys. A **539**, 662 (1992).

[19] V. B. Kopeliovich and B. E. Stern, JETP Lett. **45**, 203 (1987); NORDITA-preprint 89-34, Copenhagen (1989).

[20] S. Kabana *et al.*, J. Phys. G **23**, 2135 (1997).

[21] B. Moussalam, Ann. Phys. (N.Y.) **225**, 264 (1993); H. Wallizer, Phys. Lett. B **432**, 15 (1998); N. Scoccola and H. Wallizer, http://xxx.lanl.gov/abs/hep-ph/9805340; Phys. Rev. D **58**, 094037 (1998).

[22] M. Schvellinger and N. N. Scoccola, Phys. Lett. B **430**, 32 (1998).

[23] B. F. Gibson *et al.*, Phys. Rev. C **27**, 2085 (1983).

The effect of γ radiation on the determination of the antineutrino angular distribution from experiments on the β decay of polarized neutrons

G. G. Bunatian*)

Joint Institute for Nuclear Research, 141980 Dubna, Moscow Region, Russia

In experiments on the β decay of polarized neutrons where only the electron and proton momentum distributions are observed and the γ radiation is not registered, the asymmetry factor B of the antineutrino angular distribution cannot be obtained rigorously — the value of B is only estimated on the average by taking into consideration the expectation (mean) value $\langle B \rangle$ and the rms deviation ΔB. The resulting unavoidable ambiguities in the determination of B amount to several percent, which is significant for the present-day experimental attempts to obtain B to very high precision $\sim (0.1-1)\%$. © *1999 American Institute of Physics.* [S0021-3640(99)00310-2]

PACS numbers: 23.40.Bw, 13.30.Ce, 14.20.Dh

Recently there has been a great deal of interest in high-precision measurement of the neutron β-decay characteristics, first, the lifetime τ (Ref. 1), and, if the neutron is polarized, the asymmetry factors A and B, respectively, of the electron[2] and antineutrino[3] angular distributions with respect to the neutron polarization vector $\boldsymbol{\xi}$. The rigorous determination of the β-decay characteristics $\tau, A, B, \ldots$ is well understood nowadays to be of fundamental importance for the general elementary particle theory (see, e.g., Refs. 4–7).

The electron and antineutrino momentum distribution[4,5]

$$d\mathbf{W}(\varepsilon,\mathbf{p},\mathbf{n}_\nu,\boldsymbol{\xi}) = d\mathbf{w}\frac{d\mathbf{n}_\nu}{4\pi}(g_V^2 + 3g_A^2)\{1 + (\mathbf{v}\boldsymbol{\xi})A(g_V,g_A,\varepsilon)$$

$$+ B(g_V,g_A,\varepsilon)(\mathbf{n}_\nu\boldsymbol{\xi}) + a(g_V,g_A,\varepsilon)(\mathbf{n}_\nu\mathbf{v})\} \tag{1}$$

is usually what haunts us whenever we consider the β decay process. In Eq. (1) we have

$$d\mathbf{w} = \frac{\widetilde{G}^2}{2\pi^3}\varepsilon p\,\omega_\nu^2 d\varepsilon(d\mathbf{n}_e/4\pi), \quad \mathbf{n}_e = \mathbf{p}/p, \quad \mathbf{v} = \mathbf{p}/\varepsilon, \quad \mathbf{n}_\nu = \mathbf{p}_\nu/\omega_\nu,$$

where $\widetilde{G}$ stands for the effective β-decay amplitude[4,5] and $\varepsilon, \omega_\nu, \mathbf{p}, \mathbf{p}_\nu$ are the electron and antineutrino energies and momenta, respectively; a system of units with $h = c = 1$ is adopted. But so far as antineutrino registration is unfeasible, Eq. (1), immediately as it stands, is useless for obtaining the value of B from experiment. Since an experiment for
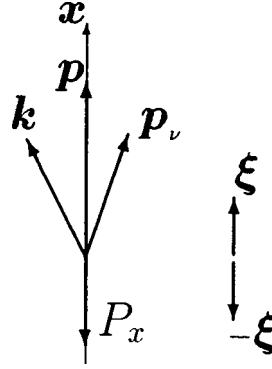
FIG. 1.

obtaining the antineutrino angular distribution without registering the antineutrino itself is expounded thoroughly in Ref. 3, here we only recall that in its ideal scheme, which is sufficient for our purposes, the registered electron momentum $\mathbf{p}$ is directed strictly along the $\mathbf{x}$ axis (see Fig. 1), the at-rest neutron polarization vector $\boldsymbol{\xi}$ is also directed exactly along or opposite the $\mathbf{x}$ axis direction, and the proton momentum projection on the $\mathbf{x}$ axis, P_x, is registered in coincidence with the electron momentum $\mathbf{p}$, while the components of the proton momentum $\mathbf{P}$ perpendicular to $\mathbf{x}$ are not observed at all, nor is the γ radiation. If for a moment we leave aside the γ radiation and neglect the kinetic energy of the proton on account of its very large mass, the antineutrino energy $\omega_{\nu 0}$ and the cosine of the angle between the $\mathbf{x}$ axis and the direction of the antineutrino emission are clearly given by

$$\omega_{\nu 0}=\Delta-\varepsilon, \quad y_0\equiv\cos\Theta_{\nu x}=(-P_x-|\mathbf{p}|)/\omega_{\nu 0}, \tag{2}$$

with the corresponding momentum distribution taking the form

$$d\mathbf{W}^z(P_x,\mathbf{p})=dP_x\frac{d\mathbf{w}}{2\omega_{\nu 0}}w^z(P_x,\mathbf{p}),$$

$$w^z(P_x,\mathbf{p})=(g_V^2+3g_A^2)[1+Azv+B_0y_0z+ay_0v]. \tag{3}$$

In (3) and hereafter, the value $z=+$ stands for neutron polarization along the $\mathbf{x}$ axis and $z=-$ for the opposite direction. We have appended a subscript 0 on B to stress that it is the value that would be obtained if the γ radiation were turned off. In the experiment of Ref. 3 the distribution

$$d\mathbf{W}^z_{\exp}(P_x,\mathbf{p})=W^z_{\exp}(P_x,\mathbf{p})\cdot d\mathbf{p}\,dP_x \tag{4}$$

was obtained. Using Eqs. (1)–(4), for which the γ radiation has been left aside, one would infer the equation

$$W^z_{\exp}(P_x,\mathbf{p})=f_0(\omega_{\nu 0})(1+zAv)+f_0(\omega_{\nu 0})y_0(zB_0+av), \tag{5}$$

and, consequently, one would arrive at the following expression, in terms of $W^z_{\exp}$ (4), for the coefficient multiplying $(\boldsymbol{\xi}\cdot\mathbf{n}_\nu)=zy_0$ in Eqs. (1) and (5):

$$B_0 = \frac{1}{zy_0f_0}[W_{\exp}^z - f_0(1+zAv) - f_0avy_0], \quad f_0 = \frac{\widetilde{G}^2\omega_{\nu 0}}{16\pi^4}(g_V^2 + 3g_A^2). \tag{6}$$

Accordingly,[3] $B_0 = 0.9821 \pm 0.004$.

However, the experiment of Ref. 3 deals with the β-decay probability for given $P_x, \mathbf{p}$ values, involving γ radiation with all the allowed momenta $\mathbf{k}$. In describing each single event, the expressions for $y_0, \omega_{\nu 0}$ in (2) will be replaced (see Fig. 1) as follows:

$$y_0 \rightarrow y(\omega) = \cos\Theta_{\nu x} = \frac{-P_x - |\mathbf{p}| - x\omega}{\omega_\nu}, \quad x = \cos\Theta_{\gamma x}, \tag{7}$$

$$f_0 \rightarrow f(\omega) = \frac{\widetilde{G}^2\omega_\nu}{16\pi^4}(g_V^2 + 3g_A^2), \quad \omega_{\nu 0} \rightarrow \omega_\nu(\omega) = \Delta - \varepsilon - \omega,$$

where $\omega = |\mathbf{k}|$ is the γ-ray energy, and $\Theta_{\gamma x}$ stands for the angle of the γ radiation direction relative to the $\mathbf{x}$ axis. It is natural to estimate the quantity B in (1) via the expectation value $\langle B \rangle$ expressed in terms of the expectation values $\langle yf \rangle, \langle f \rangle$, which are to be calculated by averaging $f(\omega), f(\omega)y(\omega,x)$ over the momentum distribution $W_\gamma^z(P_x, \mathbf{p}, \mathbf{k})$ of the γ radiation accompanying the decay event with given $P_x, \mathbf{p}, z$. Each single decay event with a given $\mathbf{k}$ value enters into the experimental $W_{\exp}^z(P_x, \mathbf{p})$ value with its own weight, its own probability $W_\gamma^z(P_x, \mathbf{p}, \mathbf{k})d\mathbf{k}$, which is the probability of γ radiation with a given momentum $\mathbf{k}$ accompanying β decay with the given $P_x, \mathbf{p}$ values. Consequently, Eq. (5) is replaced by a new relation in which the experimentally observed quantity $W_{\exp}^z(P_x, \mathbf{p})$ is equated to the β-decay probability averaged with the weight $W_\gamma^z(P_x, \mathbf{p}, \mathbf{k})$, namely:

$$W_{\exp}^z(P_x, \mathbf{p}) = \frac{\int d\mathbf{k} W_\gamma^z(P_x, \mathbf{p}, \mathbf{k})f(\omega)[1 + zAv + z\langle B \rangle^z y(\omega,x) + avy(\omega,x)]}{\int d\mathbf{k} W_\gamma^z(P_x, \mathbf{p}, \mathbf{k})}$$

$$= \langle f \rangle^z(1 + zAv) + \langle yf \rangle^z(z\langle B \rangle^z + av), \tag{8}$$

where the familiar notation of averaging is introduced:

$$\langle F \rangle^z(P_x, \mathbf{p}) = \frac{\int_0^{\Delta-\varepsilon} d\omega^2 \int_{x_1}^{x_2} dx F(P_x, \mathbf{p}, \omega, x) \int_0^{2\pi} d\phi W_\gamma^z(P_x, \mathbf{p}, \omega, x, \phi)}{\int_0^{\Delta-\varepsilon} d\omega^2 \int_{x_1}^{x_2} dx \int_0^{2\pi} d\phi W_\gamma^z(P_x, \mathbf{p}, \omega, x, \phi)}. \tag{9}$$

Here the limits x_1, x_2 emerge merely from kinematics of the process under consideration, the quantities to be averaged, $f(\omega), f(\omega)y(\omega,x)$, being independent of the azimuth ϕ of the γ radiation (see Fig. 1).

Thus we have derived Eq. (9) to replace the former equation (5). In the absence of an immediate one-to-one correspondence between the distribution (8) involving $\langle B \rangle^z$ and the antineutrino angular distribution (1) involving B, the quantity $\langle B \rangle^z$ is seen, nevertheless, to be relevant for our goal, which is to estimate, on the average, the value of B in (1):

$$\langle B\rangle^z = z[(1+zAv)(f_0 - \langle f\rangle^z) + y_0 f_0(av + zB_0)]/\langle yf\rangle^z - zav. \tag{10}$$

To judge with full confidence the accuracy and even the very validity of the afore-mentioned estimation of B in terms of $\langle B\rangle^z$, let us visualize the distributions of the quantities $f(\omega), f(\omega)y(\omega,x)$ around their mean or expectation values $\langle f\rangle, \langle fy\rangle$, that is, let us evaluate the rms deviations of $f(\omega), f(\omega)y(\omega,x)$. In short, in addition to the quantities $\langle f\rangle, \langle fy\rangle$ themselves, we must calculate the mean square deviations of $f(\omega), f(\omega)y(\omega,x)$ from their expectation values $\langle f\rangle, \langle fy\rangle$ (i.e., the variances of these quantities):

$$\langle(\Delta f)^2\rangle^z = \langle f^2\rangle^z - (\langle f\rangle^z)^2, \quad \langle(\Delta(yf))^2\rangle^z = \langle(yf)^2\rangle^z - (\langle yf\rangle^z)^2,$$

$$\langle\Delta(f\cdot yf)\rangle^z = \langle f\cdot yf\rangle^z - \langle f\rangle^z\cdot\langle yf\rangle^z. \tag{11}$$

Accordingly, the attainable accuracy

$$\Delta B^z \equiv \sqrt{\langle(\Delta B^z)^2\rangle} = \sqrt{\langle B^2\rangle^z - (\langle B\rangle^z)^2}$$

of the B value estimation (10) is expressed in the usual way (see, for instance, Ref. 8) in terms of the quantities (11) and the derivatives

$$\partial\langle B\rangle^z/\partial\langle f\rangle^z, \quad \partial\langle B\rangle^z/\partial\langle yf\rangle^z.$$

Thus the ambiguities in estimating the true value of B from the expectation values $\langle B\rangle^{\pm}$ stem from the difference between the quantities $\langle B\rangle^+$ and $\langle B\rangle^-$ themselves and from the emergence of an rms deviation $\Delta B^{\pm}$.

Upon integrating over $d\phi$ in (9), the γ radiation distribution takes the form[9]

$$\omega^2 d\omega dx d\mathbf{p} dP_x \int_0^{2\pi} d\phi W_\gamma^z(P_x,\mathbf{p},\omega,x,\phi)$$

$$= \left(\frac{e\tilde{G}}{2\sqrt{2}}\right)^2 \frac{8}{(2\pi)^7} \frac{1}{4\varepsilon^2} \frac{\varepsilon_\nu}{[1-xv]^2} \frac{1}{m}\left(\frac{m}{\omega}\right)^{(1-o)} dx d\omega dP_x d\mathbf{p}\{(1-x^2)\varepsilon v[v(\varepsilon+\omega)$$

$$\times(g_V^2+3g_A^2)+y(\omega+v^2\varepsilon)(g_V^2-g_A^2)] + \omega^2[(g_V^2+3g_A^2)+yx(g_V^2-g_A^2)](1-vx)$$

$$+2zg_A[(1-x^2)\varepsilon v[(g_V-g_A)(v^2\varepsilon+\omega)+(g_V+g_A)vy(\varepsilon+\omega)] + \omega^2(1-vx)$$

$$\times[(g_V-g_A)x+(g_V+g_A)y]]\}, \tag{12}$$

where

$$o = \frac{2\alpha}{\pi}\left[\frac{1}{v}ln\left(\frac{\varepsilon+|\mathbf{p}|}{m}\right)-1\right].$$

It should be noted that it is the presence of the quantity o in Eq. (13) that governs the true infrared ($\omega\to0$) behavior of $W_\gamma^z(P_x,\mathbf{p},\omega,x,\phi)$ (see Refs. 4,9,10).

It is pertinent to present the calculated quantities $(B^{\pm}-B_0)/B_0$, $\Delta B^{\pm}/\langle B\rangle^{\pm}$ as functions of the electron energy ε and of the quantity y_0 (2), as was done in Ref. 3. Here the dependence on ε proves to be rather smooth, whereas the dependence on y_0, in contrast, becomes strong, as is seen in Figs. 2 and 3, which typify the results of the calculations.
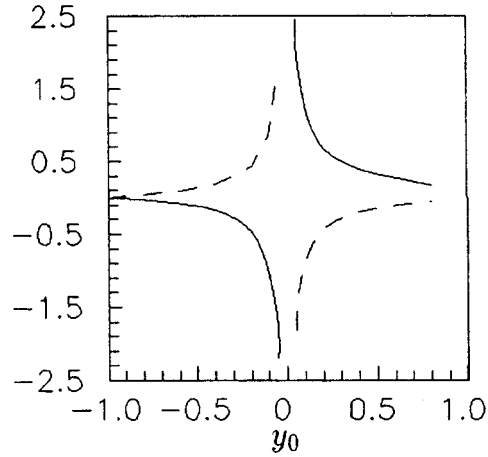
FIG. 2. The y_0 dependence of the quantity $(\langle B \rangle^z - B_0)/B_0$, in %, at the value $\varepsilon = 1$ MeV. The solid line stands for $z = +$, the dashed line for $z = -$.

The expectation value $\langle B \rangle^z$ is relevant for ascertaining the true value of B in (1) when the distributions of the values of $f(\omega), f(\omega)y(\omega,x)$ are sharp enough, that is, when, at given $P_x, \mathbf{p}$, the ratios $\Delta f/\langle f \rangle, \Delta(fy)/\langle fy \rangle$ and, hence, $\Delta B/\langle B \rangle$ turn out to be substantially smaller than (i.e., negligible in comparison with) the desired accuracy of determination of B (Ref. 3). The magnitude of the ratio $\Delta B/\langle B \rangle$ sets the bound on the precision of obtaining the value of B (1) from the processing[3] of the experimental data (4). Yet, when at certain $P_x, \mathbf{p}$ the distributions of $f(\omega), f(\omega)y(\omega,x)$ around $\langle f \rangle, \langle fy \rangle$ turn out to be so smoothed that $\Delta f/\langle f \rangle \sim 1, \Delta(fy)/\langle fy \rangle \sim 1$, and, consequently, $\Delta B/\langle B \rangle \sim 1$, there will apparently be no reason at all to estimate the quantity B (1) in terms of $\langle B \rangle^z$. In that case, the antineutrino kinematics, the antineutrino angular distribution (1), cannot be reconstructed from the experimentally observed[3] distribution (4) even on the average. Of course, it is no wonder that the values in Figs. 2 and 3 increase sharply as $y_0 \to 0$, the physical reason for such behavior of $\langle B \rangle, \Delta B$ being quite visible. Indeed, when $y_0 \approx 0$,
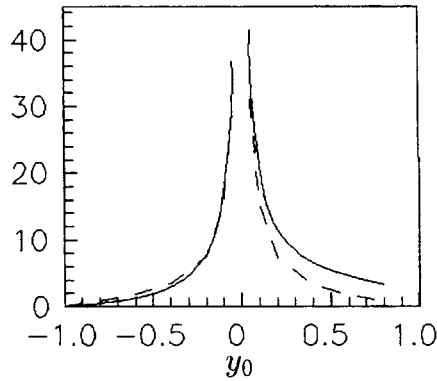

FIG. 3. The same as in Fig. 2, but for the quantity $\Delta B^z/\langle B \rangle^z$.

that is $|\mathbf{p}| + P_x \approx 0$, the inclusion of the term $x\omega$ in $y(\omega, x)$ (7) gives rise to appreciable values of the ratios $(y - y_0)/y_0, \Delta y/\langle y \rangle$ at any ω, even a very tiny one. In this case, any γ radiation absolutely destroys the antineutrino kinematics that would hold in the absence of electromagnetic interactions. In turn, the values of $(\langle B \rangle^{\pm} - B_0)/B_0, \Delta B^{\pm}/\langle B \rangle^{\pm}$ increase significantly and can even get arbitrary large at $|y_0| \to 0$. Of course, under such circumstances one can say nothing about the expectation (mean) values themselves. By processing all the experimental data beyond these small $|y_0|$ values, we can claim to acquire a semiquantitative estimate of B to an accuracy of a few percent. At best, when only events with $|y_0| \approx 0.8 - 1.0$ are taken into account, an accuracy better than 1% is thought to be attainable in recovering the antineutrino asymmetry coefficient B.

Thus there is, alas, no justification for glossing over the effect of γ radiation on the determination of B and touting the achievement of very high accuracy $\approx 0.4\%$ in the measurement of B, as proclaimed in Ref. 3.

*)e-mail: bunat@cv.jinr.dubna.su

[1] J. Byrne *et al.*, Europhys. Lett. **33**, 187 (1996).

[2] P. Liaud *et al.*, Nucl. Phys. A **612**, 53 (1997).

[3] I. A. Kuznetsov *et al.*, JETP Lett. **60**, 311 (1994); I. A. Kuznetsov *et al.*, Phys. Rev. Lett. **75**, 794 (1995); A. P. Serebrov *et al.*, Zh. Éksp. Teor. Fiz. **113**, 1963 (1998) [JETP **86**, 1074 (1998)].

[4] V. B. Berestetskiĭ, E. M. Lifshitz, and L. P. Pitaevskiĭ, *Relativistic Quantum Field Theory*, Pergamon Press, Oxford, 1971 [Russ. original, Part II, Nauka, Moscow, 1971].

[5] E. D. Commins and P. H. Bucksbaum, *Weak Interactions of Leptons and Quarks*, Cambridge University Press, Cambridge, 1983.

[6] M. Kobajashi and T. Maskawa, Prog. Theor. Phys. **49**, 625 (1973).

[7] A. P. Serebrov and N. V. Romanenko, JETP Lett. **55**, 503 (1992); B. R. Hostein and S. B. Treiman, Phys. Rev. D **16**, 2369 (1977).

[8] L. D. Landau and E. M. Lifshitz, *Statistical Physics*, Pergamon Press, London, 1958 [Russ. original, Gostekhizdat, Moscow, 1951].

[9] G. G. Bunatian, Yad. Fiz. **62**, 697 (1999) [Phys. At. Nucl. **62**, 648 (1999)]; /aps1999mar11_005.

[10] D. R. Yennie, S. C. Frautschi, and H. Suura, Ann. Phys. (N.Y.) **13**, 379 (1961).

On the ''supercollimation'' of x-ray beams in rough interfacial channels

T. A. Bobrova and L. I. Ognev*)

Nuclear Fusion Institute, Kurchatov Institute Russian Research Center, 123182 Moscow, Russia

The transmission of x rays through rough submicron narrow channels is investigated by numerical simulation with diffraction and decay of coherence taken into account. It is found that transmission is strongly increased for directions within the diffraction limit λ/d (d is the channel width). For larger angles strong roughness scattering results in rapid decay of coherence and absorption of the x-ray beams. When the coherent part is a significant portion of the transmitted beam, its divergence is also within the diffraction limit, which can be an order of magnitude smaller than the Fresnel angle of total external reflection. The effects are explained with the statistical theory of x-ray scattering in a rough transitional layer. Such ''supercollimation'' can be used for fine angular discrimination of x radiation and for the production of very narrow diffraction-quality x-ray beams. © *1999 American Institute of Physics.* [S0021-3640(99)00410-7]

PACS numbers: 41.50.+h, 07.85.−m

Monitoring of x-ray beams by capture into a narrow dielectric channel is used in waveguide x-ray laser physics,[1] in the production of thin x-ray probe beams,[2] and other applications based on the total external reflection effect. The minimum angle of divergence of the beam in this case is limited by the Fresnel angle ϑ_F, and roughness scattering can only degrade this parameter. In this letter we consider the role of diffraction, which can be important for narrow beams, especially when the roughness is high. Scattering from surfaces with high roughness requires a special approach because small-perturbation methods fail.[3] X-ray scattering at rough surfaces is usually investigated within the well-known Andronov–Leontovich approach,[4] but for very small angles of incidence the ''parabolic equation'' model for slowly varying scalar amplitudes $A(x,z)$ of the electric field vector should be used. Within this model, scattering and absorption do not disappear in the small grazing angle limit that results from the Andronov–Leontovich approach.[4] In this case large-angle scattering is neglected, so that

$$\partial^2 A(x,z)/\partial z^2 \ll k \cdot \partial A(x,z)/\partial z,$$

and, because the beam is narrow,

$$\partial^2 A(x,z)/\partial z^2 \ll \partial^2 A(x,z)/\partial x^2,$$

where z and x are the coordinates along and across the channel. Here consideration will
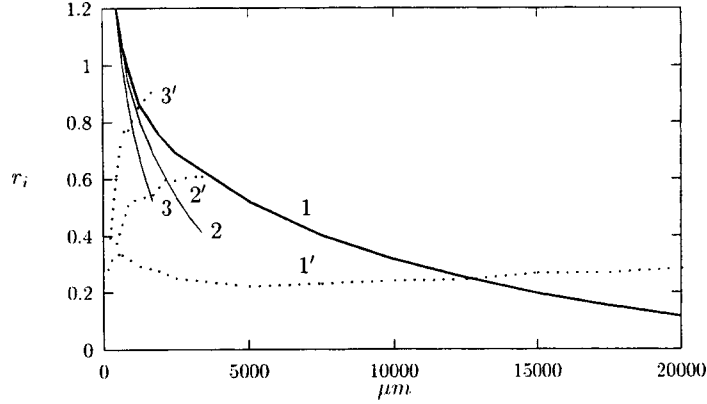
FIG. 1. Evolution of the total integral normalized intensity of the beam r_{tot} and normalized incoherent part $r_{part} = r_{inc}/r_{tot}$ for different angles of incidence ϑ. $\vartheta = 0$, r_{tot} (curve 1), r_{part} (curve $1'$); $\vartheta_F/10$ (curves 2 and $2'$); $\vartheta_F/5$ (curves 3 and $3'$).

be restricted to two-dimensional channels (gaps), although the same approach can be applied to capillaries. The assumption results in the "parabolic equation" of quasioptics:

$$2ik\frac{\partial A}{\partial z} = \Delta_{\perp}A + k^2\frac{\varepsilon - \varepsilon_0}{\varepsilon_0}A, \tag{1}$$

$$A(x, z=0) = A_0(x),$$

where $k = \sqrt{\varepsilon_0}(\omega/c)$. (Here ε_0 is the dielectric permittivity of air, and ε_1 is the dielectric permittivity of glass.) The evolution of the channeled x-ray beam was calculated by direct integration of the "parabolic" equation.[5] The dielectric permittivity on the rough boundary, with the random shape $x = \xi(z)$, was represented as $\varepsilon(x,z) = \varepsilon_1 + (\varepsilon_0 - \varepsilon_1)H(x - \xi(z))$, where $H(x)$ is a step function. The distribution of roughness heights is assumed to be normal. It is known from the results of Ref. 4 that at grazing incidence the effect of scattering is very small. Therefore special surfaces are needed to observe scattering effects in the gap interface at a reasonable distance. In the calculations we used roughness amplitudes up to 400 Å. The results of direct simulation of scattering with the model rough surface by integration of Eq. (1), calculated for an x-ray energy $E = 10$ keV, channel width $d = 0.5$ μm, $\sigma = 400$ Å, and roughness correlation length $z_{corr} = 5$ μm and averaged over 40 realizations, are shown in Fig. 1 as the incoherent part r_{inc} normalized to the initial value of the total intensity of the beam r_{tot}, where

$$r_i = \int_{-\infty}^{\infty} I_i(x)dx \Big/ \int_{-d/2}^{d/2} I_0(x)dx.$$

The initial angles of incidence were $\vartheta = 0$, $3 \cdot 10^{-4}$, and $6 \cdot 10^{-4}$ rad.

Angular spectra of the coherent and incoherent parts of the wave amplitude averaged over 40 realizations are shown in Fig. 2.

Statistical averaging of Eq. (1) gives for the last term the expression (the angle brackets correspond to averaging)

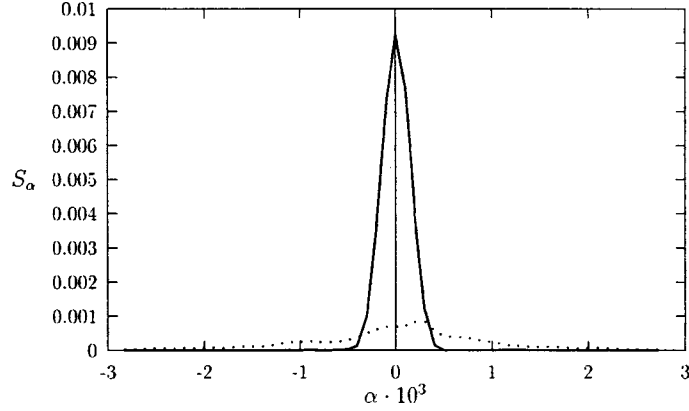$$k^2\chi(x,z)\langle A(x,z)\rangle + k^2\langle\delta\varepsilon'\cdot A(x,z)\rangle,$$

FIG. 2. Angular spectra of coherent (solid curve) and incoherent (dots) components of the x-ray beam after transmission through a 2 cm rough gap.

where

$$\chi(x,z)=(\langle\varepsilon(x)\rangle-\varepsilon_0)/\varepsilon_0, \quad \delta\varepsilon'(x,z)=(\varepsilon(x,z)-\langle\varepsilon(x)\rangle)/\varepsilon_0.$$

The first term in the sum corresponds to absorption of the x-ray beam and the last term to decay of coherence due to incoherent scattering. Assuming that the variation of $A(x,z)$ over the roughness correlation length z_{corr} is small and that $\langle\delta\varepsilon(x,z)\rangle=0$, we can use the statistical method of Tatarsky (see Ref. 6), which is valid for δ-correlated fluctuating media. Thus

$$\langle\delta\varepsilon'(x,z)\cdot A(x,z)\rangle=\langle A(x,z)\rangle(-ik/4)\int_{-\infty}^{\infty}\langle\delta\varepsilon'(x,z)\delta\varepsilon'(x,z')\rangle dz'.$$

The same generalization of the method to include stratified media has been used in the case of electron channeling in single crystals.[7] Thus the coefficient multiplying $\langle A(x,z)\rangle$ has the meaning of a ''scattering potential'' that causes decay of coherence and can be written as

$$W(x)=(-ik/4)\int_{-\infty}^{\infty}\langle\delta\varepsilon'(x,z)\delta\varepsilon'(x,z')\rangle dz'=-\frac{k}{4}\frac{(\varepsilon_0-\varepsilon_1)^2}{\pi(\varepsilon_0)^2}$$

$$\times\int_{-\infty}^{+\infty}dz'\int_{-\infty}^{x/\sigma}\exp(-\xi^2)d\xi\int_{x/\sigma}^{x/\sigma-R(z')\xi/(1-R^2(z'))^{1/2}}\exp(-\eta^2)d\eta, \tag{2}$$

where $R(z)$ is the autocorrelation coefficient, and σ is the variance of the $\xi(z)$ distribution. Thus the coherent part of the amplitude $A(x,z)$ can be calculated from the statistically averaged equation

$$2ik\partial\langle A(x,z)\rangle/\partial z-\Delta_\perp\langle A(x,z)\rangle-k^2\chi(x)\langle A(x,z)\rangle-ik^2W(x)\langle A(x,z)\rangle=0, \tag{3}$$

and

$$\langle A(x,z=0)\rangle=A_0(x).$$

It can be shown that the value of $W(x)$ in the middle of the transitional layer ($x=0$) does not depend on σ and is nearly proportional to the roughness correlation length
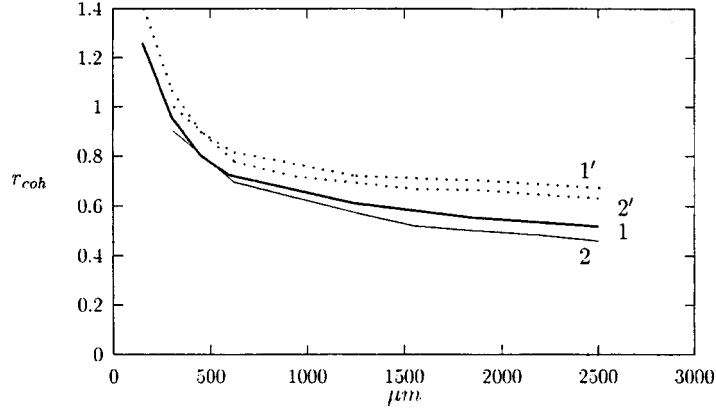
FIG. 3. Decay of the coherent part of the radiation, r_{coh}, calculated with statistical averaging (solid curves) and in the transitional layer model (2) with the assumption (4) (dashed curves), $\vartheta = 0$. $z_{corr} = 5$ μm (curves 1 and $1'$); $z_{corr} = 2$ μm (curves 2 and $2'$); $\sigma = 400$ Å.

z_{corr}. The same is true for $x = d$. This results in a weak dependence of the phase shifts of the incoherently scattered wave on the value of σ, unlike the case for the higher angles of incidence of the beam which have usually been investigated in experiments.

The inner double integrals in Eq. (2) can be simplified for small R, and an approximation for $W(x)$ can be written as

$$W(x) \approx -\frac{k}{4} \frac{(\varepsilon_0 - \varepsilon_1)^2}{\pi(\varepsilon_0)^2} \int_{-\infty}^{\infty} dz' \int_{-\infty}^{0} \exp(-\xi^2) d\xi$$

$$\times \int_{0}^{-R(z')\xi/(1-R^2(z'))^{1/2}} \exp(-\eta^2) d\eta \cdot \exp\left(-\frac{x^2}{\sigma^2}\right) \tag{4}$$

with a clear dependence on the vertical coordinate x.

The results for the coherent part of the beam obtained by averaging the solution of equation (1) and integrating Eq. (3) with approximation (4) are shown in Fig. 3.

The decay of coherence can be described with attenuation coefficients β_l. The attenuation coefficients can be found as overlap integrals,

$$\beta_l = -\frac{k}{2} \int \varphi_l^*(x)[\text{Im}(\chi(x)) + W(x)]\varphi_l(x) dx,$$

where the eigenfunctions $\varphi_j(x)$ are solutions of the equations

$$\Delta_\perp \varphi_j(x) = k[2k_{jz} - k\text{Re}(\chi(x))]\varphi_j(x).$$

It can be shown for lower channeled modes that the incoherent scattering attenuation coefficient is proportional to σ (see the discussion above about the dependence of $W(x)$ on σ):

$$\beta_{\text{scatter}} \sim k^2 (\varepsilon_0 - \varepsilon_1)^2 \sigma \int_{-\infty}^{\infty} dz' \int_{-\infty}^{0} \exp(-\xi^2/2) d\xi$$

$$\times \int_{0}^{-R(z')\xi/(1-R^2(z'))^{1/2}} \exp(-\eta/2^2) d\eta.$$

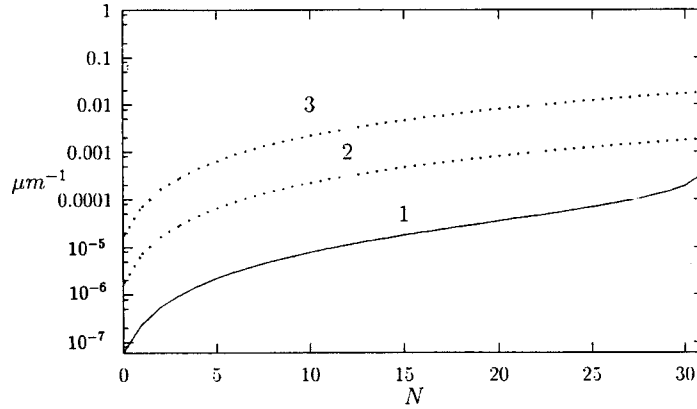FIG. 4. Dependence of the attenuation coefficients for incoherent scattering $\beta_{scatter}$ (dashed lines *2*, *3*) and absorption β_{absorp} (solid line *1*) on the mode number *N*; $\sigma = 100$ Å, $z_{corr} = 2$ μm (curve *2*); $\sigma = 400$ Å, $z_{corr} = 5$ μm (curve *3*). The center of mode *N* corresponds to $\vartheta_N \approx 1.24 \cdot 10^{-4} \cdot N$.

The results for the attenuation coefficients $[\mu m^{-1}]$ for various wave modes are shown in Fig. 4 separately for absorption and incoherent scattering within a 0.5 μm quartz glass channel. The angle of incidence ϑ_N corresponding to the center of the *N*th mode ($N \geqslant 1$) is $\vartheta_N = \lambda/2d \cdot (N + 1/2)$.

It is seen from Fig. 4 that the effect of incoherent scattering for given correlation length is an order of magnitude higher than the effect of real absorption. Coherence effects for modes number "1" and higher will decay after several millimeters of channel length. And decreasing the correlation length will result in a nearly proportional decrease of the incoherent scattering. The rate of coherence decay of the "0" mode agrees well with the results shown in Fig. 3.

The "supercollimation effect" can be measured as the strong sharpening of the angular dependence of the transmission of x rays through an interface, to below the Fresnel angle of total external reflection. Such "supercollimation" can be used for fine angular discrimination of x radiation and for the production of very narrow diffraction-quality x-ray beams for use as probes and also of high-quality soft x-ray beams for x-ray laser amplifiers.

*e-mail: ognev@nfi.kiae.su

[1] S. V. Kukhlevsky, G. Lubkovics, K. Negrea, and L. Kozma, Pure Appl. Opt. **6**, 97 (1999).
[2] S. A. Hoffman, D. J. Thiel, and D. H. Bilderback, Nucl. Instrum. Methods Phys. Res. A **347**, 384 (1994).
[3] S. S. Fanchenko and A. A. Nefedov, Phys. Status Solidi B **212/1**, R3 (1999).
[4] A. V. Vinogradov, N. N. Zorev, I. V. Kozhevnikov, and I. G. Yakushkin, Zh. Éksp. Teor. Fiz. **89**, 2124 (1985) [Sov. Phys. JETP **62**, 1225 (1985)].
[5] T. A. Bobrova and L. I. Ognev, Phys. Status Solidi B **203/2**, R11 (1997).
[6] V. Holý and K. T. Gabrielyan, Phys. Status Solidi B **140**, 39 (1987).
[7] L. I. Ognev, Radiat. Eff. Defects Solids **25**, 81 (1993).

Development of Rayleigh–Taylor and Richtmyer–Meshkov instabilities in three-dimensional space: topology of vortex surfaces

N. A. Inogamov

L. D. Landau Institute of Theoretical Physics, Russian Academy of Sciences, 142432 Chernogolovka, Moscow Region, Russia

A. M. Oparin

Institute of Computer-Aided Design, Russian Academy of Sciences, 123056 Moscow, Russia

The evolution of the boundary of a liquid during the development of mixing instabilities is studied. The vortex filaments, which transport liquid masses, are generators of the boundary surface. There is a fundamental difference between two-dimensional (2D) and three-dimensional (3D) motions. In the first case the vortices are rectilinear in planar geometry ($2D_p$) and ring-shaped in axisymmetric geometry ($2D_a$). In the second case the vortices are very complicated. Spatially periodic (''single-mode'') solutions, which are important in mixing theory, are investigated. These solutions describe one-dimensional chains of alternating bubbles and jets in $2D_p$ geometry and planar (two-dimensional) arrays or lattices of bubbles and jets in 3D geometry. An analytical description is obtained for the basic types of arrays (rectangular, hexagonal, and triangular). The analysis agrees with the results of numerical simulation. © *1999 American Institute of Physics.* [S0021-3640(99)00510-1]

PACS numbers: 47.20.−k, 47.32.Cc, 47.55.Dz

It is well known that hydrodynamic instabilities play a large role in astrophysics, in inertial confinement fusion, and in the physics of explosions. An idea of the present status of the research can be obtained from Refs. 1–16. Bubbles and jets form at the unstable interface between liquids with different densities. The bubbles (jets) are columns of a light (heavy) substance penetrating into a heavy (light) substance. At the late stages a subharmonic instability of the periodic solutions increases the characteristic mixing scale and leads to an inversion cascade.[3–5,8,10,11,17]

In Layzer's model,[18] to the three-dimensional (3D) generalization of which the present letter is devoted, a parabolic approximation of the boundary near the top of a bubble is used. This makes it possible to obtain a system of dynamical equations for the velocity and curvature of a bubble.[7,8,11–13,16] The solutions of the system describe the transition from an initial weakly perturbed state into a strongly nonlinear state (into a

stationary state or a stationary point), where the instability ''saturates'' as a result of compensation by nonlinear terms. Exact analytical solutions of the Layzer system in the two-dimensional (2D) geometry have been obtained recently.[7,11–13,16] In Ref. 11 the exact solution is written out for a square array. In what follows the 3D nonstationary solutions are presented for a wide class of different arrays. We note that the problem of stationary points for the Rayleigh–Taylor instability (RTI) has been studied in Refs. 9, 11, 12, and 15 (square array) and in Ref. 15 (hexagonal array). Of course, the problem of the RT stationary state is narrower than the complete formulation, where the RTI, the Richtmyer–Meshkov instability (RMI), and a nonstationary transition having a stationary state as a limit of temporal evolution, are studied. Higher-order Layzer approximations where the surface is approximated not by a parabola ($N=1$) but by a polynomial of degree $2N$ ($N>1$) are analyzed in Refs. 7 and 12. A three-dimensional numerical simulation is given in Refs. 10 and 19–22.

We shall study an incompressible, nonviscous liquid with an infinite density ratio at the boundary along lines similar to Refs. 1, 2, 7–9, 11–13, and 15–17. The vorticity is concentrated at the boundary, and the motion inside the liquid is potential. The equations of motion have the form

$$\nabla^2\varphi=0,\quad \eta_t=\varphi_z|_\eta-\eta_x\varphi_x|_\eta-\eta_y\varphi_y|_\eta,\quad -2\varphi_t|_\eta=\varphi_x^2|_\eta+\varphi_y^2|_\eta+\varphi_z^2|_\eta+2g\,\eta,\quad (1)$$

where $z=\eta(x,y,t)$ is the boundary of the liquid, the liquid occupies the region $z>\eta$, $\mathbf{g}=\{0,-g\}$ is the acceleration of gravity, $g=0$ for RMI and $g=1$ for RTI, and $\varphi(x,y,z,t)$ is the 3D velocity potential ($\mathbf{v}=\nabla\varphi$), whose spectral decomposition has the form

$$\varphi=-\frac{1}{2}\sum_{n=0}^\infty\sum_{m=0}^\infty\frac{a_{nm}}{q_{nm}}\cos nx\,\cos mqy\,\exp(-q_{nm}z),\quad q_{nm}=\sqrt{n^2+m^2q^2},\quad (2)$$

$$\varphi=-\frac{1}{6}\sum_{n=0}^\infty\sum_{m=0}^\infty\frac{a_{nm}}{q_{nm}}(c_nc_m^++s_ns_m^++c_nc_m^-+s_ns_m^-+c_n^+c_m^--s_n^+s_m^-)e_{nm},\quad (3)$$

$$c_n=\cos nx,\quad c_n^\pm=\cos n\xi^\pm,\quad s_n=\sin nx,\quad s_n^\pm=\sin n\xi^\pm,\quad \xi^\pm=\frac{x\pm\sqrt{3}y}{2},$$

$$e_{nm}=\exp(-q_{nm}z),\quad q_{nm}=\sqrt{n^2-nm+m^2}.$$

The series (2) refers to a rectangular array, a particular case of which is a square array when the edge length ratio for the rectangle $q=1$, and the series (3) refers to hexagonal and triangular arrays.

In Layzer's model the expansions (2) and (3) are truncated at the first terms. The potentials of the hexagonal (φ_6), square (φ_4), triangular (φ_3), and rectangular (φ_2) arrays of bubbles have the form

$$\varphi_6=-\frac{a(t)}{3}(c+c^++c^-)e^{-z},\quad c=\cos x,\quad c^\pm=\cos\xi^\pm,\quad (4)$$

$$\varphi_4=-\frac{a(t)}{2}(\cos x+\cos y)e^{-z},\quad (5)$$

$$\varphi_3 = \frac{a(t)}{6}(c - \sqrt{3}s + c^+ + \sqrt{3}s^+ + c^- + \sqrt{3}s^-)e^{-z}, \quad s = \sin x, \quad s^{\pm} = \sin \xi^{\pm}, \quad (6)$$

$$\varphi_2 = -\frac{\hat{a}(t)}{2}\cos x \, e^{-z} - \frac{\hat{b}(t)}{2q}\cos qx \, e^{-qz}. \tag{7}$$

The tops of the bubbles in all cases lie at the center $x=y=0$, $a>0$ in Eqs. (4)–(5), $a<0$ in Eq. (6), and $\hat{a}>0$ and $\hat{b}>0$ in Eq. (7).

The principal curvatures of the surface η at the top of a bubble are the same for a hexagon, square, and triangle. For this reason the expansion of the boundary of the liquid near the top has the form

$$\eta(x,y,t) = \eta_0(t) - K(t)\frac{\Delta}{2}, \quad \Delta = x^2 + y^2. \tag{8}$$

For a rectangle the principal curvatures are different. Correspondingly,

$$\eta(x,y,t) = \eta_0(t) - Kx^2/2 - Qy^2/2. \tag{9}$$

Expanding the potentials (4)–(7) in powers of the small deviations x^2 and y^2 from the top of the bubble, substituting these expansions and the expansions (8) and (9) into the boundary conditions (1), and retaining only terms which are quadratic in x and y, we arrive at the following system of dynamical equations:

$$\dot{K} = \frac{1-4K}{2}W, \quad \dot{W} = -\frac{W^2 - 4gK}{2(1-2K)}, \tag{10}$$

$$\dot{K} = (1-3K)a - qKb, \tag{11}$$

$$\dot{Q} = -Qa + q(q-3Q)b, \tag{12}$$

$$(1-K)\dot{a} - K\dot{b} = -a^2 + gK, \tag{13}$$

$$-Q\dot{a} + (q-Q)\dot{b} = -q^2b^2 + gQ. \tag{14}$$

The system (10) is universal. It describes hexagonal, square, and triangular arrays of bubbles. The system (11)–(14) refers to a rectangular array. In Eqs. (10) $W = \dot{\eta}_0$ is the rise velocity of a bubble, and in Eqs. (11)–(14) this velocity is $a+b$.

The system (10) can be easily integrated for $g=0$ (RMI). Its solution has the form

$$\sqrt{\frac{1-2K}{1-4K}} - 1 - \frac{1}{\sqrt{2}}\ln\frac{\sqrt{2(1-2K)} + \sqrt{1-4K}}{\sqrt{2}+1} = W_0 t,$$

$$\frac{W_0}{W} - 1 + \frac{1}{2\sqrt{2}}\ln\left(\frac{\sqrt{2}+1}{\sqrt{2}-1}\frac{\sqrt{2}W_0 - W}{\sqrt{2}W_0 + W}\right) = W_0 t.$$

Analysis of the systems (10) and (11)–(14) shows that they describe a transition from an initial state with a small perturbation amplitude into a stationary state as

$t \to \infty$. The stationary state is a node where all trajectories converge. This is easy to show for Eqs. (10) by constructing the phase plane (K, W). For the system (10)–(14) this follows from an analysis of the stability of stationary states.

We now give the stationary solutions. For $g = 1$ (RTI) we have

$$K = 1/4, \quad W = 1. \tag{15}$$

For $g = 0$ (RMI) we have

$$K = 1/4, \quad W = 1/t. \tag{16}$$

The stationary states (15) and (16) correspond to hexagonal, square, and triangular arrays of bubbles.

The case of a rectangular array is more complicated. We shall consider the RTI. Let $\dot{K} = \dot{Q} = \dot{a} = \dot{b} = 0$ in Eqs. (11)–(14). We eliminate the unknowns $a > 0$, $b > 0$ using Eqs. (13) and (14) and Q using Eqs. (11) and (12). As a result we arrive at an equation for K. This equation has the form

$$8K^2 - [6 + (q - 1)/3]K + 1 = 0.$$

Comparing with the case of a square $q = 1$, we find that only the root

$$K(q) = (q + 17 - r)/48, \quad r = + \sqrt{q^2 + 34q + 1}, \tag{17}$$

is physically meaningful. The other unknown functions are given by the expressions

$$Q(q) = \frac{q - 1}{3} + K(q), \quad a(q) = + \sqrt{K(q)}, \quad b(q) = + \frac{\sqrt{Q(q)}}{q}. \tag{18}$$

The stationary state (17) and (18) is unique in the physically meaningful region.

Let us consider the RMI. In this case, in the stationary state the curvatures K and Q are constant, while the amplitudes are $a = \alpha/t$ and $b = \beta/t$. Substituting these relations into the system (11)–(14), we arrive at an algebraic system for the unknowns K, Q, α, and β. Eliminating the unknowns β and α and then Q, we obtain the equation

$$24(3 - q)K^3 + (q^2 + 46q - 75)K^2 + 2(13 - 11q)K + 3(q - 1) = 0 \tag{19}$$

for the desired function $K(q)$. The physically meaningful root is selected by the condition $K(1) = 1/4$, signifying that the case of a square array (16) is reached as $q \to 1$. Let $K(q)$ be this root. The remaining functions can be expressed in terms of it. We have

$$Q = \frac{1 - 3K}{3 - 8K}q, \quad \alpha = 1 - \frac{1}{q} + \left(\frac{3}{q} - 1\right)K, \quad \beta = \frac{1 - 3K}{qK}\alpha, \quad w = \alpha + \beta. \tag{20}$$

The velocity of the bubbles is w/t. The root $K(q)$ exists in the segment $1 < q < 1.26$. For $q > 1.26$ Eq. (19) does not possess the required real roots. Therefore the physically correct solution in the parabolic approximation is limited to this segment.

We shall now investigate the stability of the solutions (17),(18) and (19),(20). We linearize the system (11)–(14) around the stationary states. We write

$$K(t) = K + \delta K\, e^{\lambda t}, \quad Q(t) = Q + \delta Q\, e^{\lambda t}, \quad a(t) = a + \delta a\, e^{\lambda t}, \quad b(t) = b + \delta b\, e^{\lambda t}$$

for the RTI and

$$K(t)=K+\delta K\, t^{\lambda}, \quad Q(t)=Q+\delta Q\, t^{\lambda}, \quad a(t)=\frac{\alpha+\delta\alpha\, t^{\lambda}}{t}, \quad b(t)=\frac{\beta+\delta\beta\, t^{\lambda}}{t}$$

for the RMI. The matrices M for the eigenvalues λ have the form

$-\lambda-3a-qb$	0	$1-3K$	$-qK$
0	$-\lambda-a-3qb$	$-Q$	q^2-3qQ
1	0	$-(1-K)\lambda-2a$	$K\lambda$
0	1	$Q\lambda$	$-(q-Q)\lambda-2q^2b$

in the RTI case and

$-\lambda-3\alpha-q\beta$	0	$1-3K$	$-qK$
0	$-\lambda-\alpha-3q\beta$	$-Q$	q^2-3qQ
$\alpha+\beta$	0	$(1-K)(\lambda-1)+2\alpha$	$K(1-\lambda)$
0	$\alpha+\beta$	$Q(1-\lambda)$	$(q-Q)(\lambda-1)+2q^2\beta$

in the RMI case. In these matrices K, Q, a, b (RTI) and K, Q, α, β (RMI) are given by expressions (17),(18) and (19),(20), respectively. Calculation of the characteristic equations $\det M=0$ shows that the solutions (17),(18) and (19),(20) are stable.

We shall now compare the hexagonal, square, and triangular arrays. From the universal system (10) follows the unexpected conclusion that for the same initial values of the curvature and velocity the trajectories describing the evolution of these different bubble arrays will be identical. Specifically, the limiting bubble velocities and curvatures are the same.

For the same wave number k, the area per bubble in the hexagonal, square, and triangular arrays is

$$S_6=\frac{8\,\pi^2}{\sqrt{3}\,k^2}=\frac{2}{\sqrt{3}}S_4, \quad S_4=\frac{4\,\pi^2}{k^2}, \quad \text{and}\quad S_3=\frac{4\,\pi^2}{\sqrt{3}\,k^2}=\frac{1}{\sqrt{3}}S_4.$$

We require the areas to be the same. Then the wave numbers of the arrays are in the ratio

$$k_6:k_4:k_3=\sqrt{\frac{S_6}{S_4}}:1:\sqrt{\frac{S_3}{S_4}}=\frac{\sqrt{2}}{3^{1/4}}:1:\frac{1}{3^{1/4}}\approx1.07:1:0.76.$$

The radii R_6, R_4, and R_3 for RTI and RMI are in the opposite ratio (the radius R_6 is shortest). With respect to the rate of the transient process the arrays fall into the sequence 6, 4, and 3, i.e., the transition to the triangular array is slowest. But in return the maximum bubble velocity in this array is highest. These velocities are in the ratio

$$w_6:w_4:w_3=(S_4/S_6)^{1/4}:1:(S_4/S_3)^{1/4}=(1/\sqrt{k_6}):(1/\sqrt{k_4}):(1/\sqrt{k_3})$$

$$=(3^{1/8}/2^{1/4}):1:3^{1/8}\approx0.97:1:1.15$$

for RTI and $(1/k_6):(1/k_4):(1/k_3)$ for RMI.

Let us compare the analytical results with the numerical results. The complete system of Euler equations for a compressible nonviscous medium written in the divergent form[23,24] was integrated. A quasimonotonic mesh–characteristic scheme of second-order approximation was used. Monotonicity is attained by combining schemes with central and oriented differences. A similar hybrid method has been used for numerical simulation
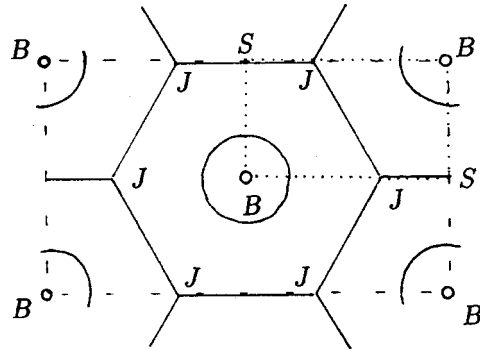
FIG. 1. Hexagonal array, symmetry planes BB, BJ, and JJ, tops of the bubbles B and jets J. For a triangular array the bubbles and jets change places.

of flows of an incompressible liquid.[25] The computational scheme does not employ artificial viscosity or smoothing or a flow-limiting procedure. The scheme possesses helpful qualities, such as conservativeness, monotonicity, and a high order of approximation. The monotonicity requirement gives nonlinear dissipation, which smooths the short-wavelength disturbances with wavelength of the order of several grid steps. The integration region is a rectangular parallelepiped, on whose lateral boundaries the symmetry
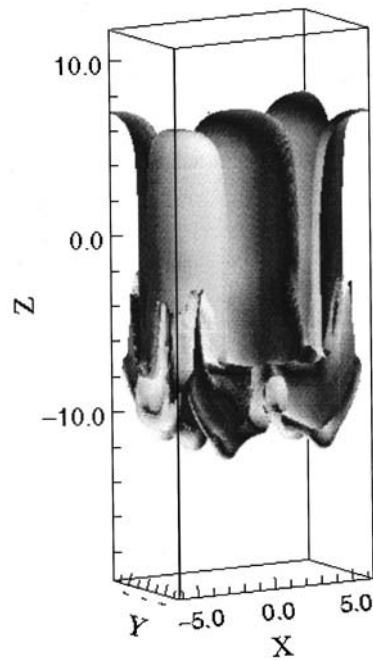
FIG. 2. Topology of the interface η, hexagonal array, and a transverse section of this region — the rectangle $BBBB$, shown by the fine dashes in Fig. 1.
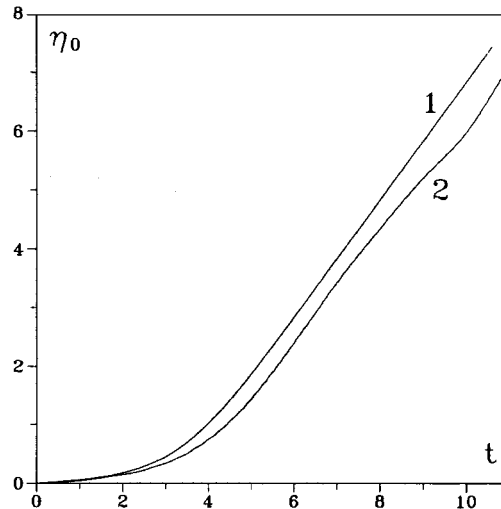
FIG. 3. Comparison of the analytical calculation (curve *1*) and the theoretical simulation (curve *2*).

conditions hold and on whose bottom and top boundaries the impenetrability conditions hold. The transverse section $BSBS$ for a hexagonal array is shown in Fig. 1 (dots).

Square and rectangular arrays with $q = \sqrt{2}$ 2, and 4 and a hexagonal array were studied. The agreement with theory is good. The form of the surface at time $t = 11$ for a hexagonal initial perturbation with a small amplitude $a(0) = 0.05$ and $g = 1$ is shown in Fig. 2. The figure was obtained by adding four working parallelepipeds (the rectangles $BSBS$ and $BBBB$ in Fig. 1). The formation of a periodic structure of rounded finger-shaped bubbles and topologically complicated vortex formations in the region of interaction of jets of heavy liquid, falling from above (the density ratio $\mu = 1/10$), with the underlying light liquid can be seen. Figure 3 shows the time dependence of the bubble displacement $\eta_0(t)$ for the hexagonal array shown in Fig. 2. As we can see, the agreement between the analytical and numerical results is good.

[1] S. W. Haan, Phys. Fluids B **3**, 2349 (1991).
[2] N. A. Inogamov, JETP Lett. **55**, 521 (1992).
[3] S. Atzeni, A. Guerrieri, Europhys. Lett. **22**, 603 (1993).
[4] D. L. Youngs, Laser Part. Beams **12**, 725 (1994).
[5] J. F. Haas, I. Galametz, L. Houas *et al.*, Chocs. Num. **14**, 15 (1995).
[6] R. L. Holmes, J. W. Grove, and D. H. Sharp, J. Fluid Mech. **301**, 51 (1995).
[7] N. A. Inogamov, Zh. Éksp. Teor. Fiz. **107,** 1596 (1995) [JETP **80**, 890 (1995)].
[8] U. Alon, J. Hecht, D. Ofer, and D. Shvarts, Phys. Rev. Lett. **74**, 534 (1995).
[9] N. A. Inogamov and S. I. Abarzhi, Physica D **87**, 339 (1995).
[10] M. M. Marinak, R. E. Tipton, B. A. Remington *et al.*, Inertial Confinement Fusion **5**, 168 (1995).
[11] N. A. Inogamov, *Proceedings of the 6th International Workshop on the Physics of Compressible Turbulent Mixing*, edited by G. Jourdan and L. Houas, Institut Universitaire des Systemes Thermiques Industriels, Printed in France by Imprimerie Caractere, Marseille, 1997, 208.

[12] N. A. Inogamov, Laser Part. Beams **15**, 53 (1997).

[13] K. O. Mikaelian, Phys. Rev. Lett. **80**, 508 (1998).

[14] M. M. Marinak, S. G. Glendinning, R. J. Wallace *et al.*, Phys. Rev. Lett. **80**, 4426 (1998).

[15] S. I. Abarzhi, Phys. Rev. Lett. **81**, 337 (1998).

[16] Q. Zhang, Phys. Rev. Lett. **81**, 3391 (1998).

[17] S. I. Anisimov, A. V. Chekhlov, A. Yu. Dem'yanov, and N. A. Inogamov, Russ. J. Comp. Mech. **1**, 5 (1993).

[18] D. Layzer, Astrophys. J. **122**, 1 (1955).

[19] Yu. M. Davydov and M. S. Panteleev, Zh. Prikl. Mekh. Tekh. Fiz. **1**, 117 (1981).

[20] T. Yabe, H. Hoshino, and T. Tsuchiya, Phys. Rev. A **44**, 2756 (1991).

[21] D. L. Youngs, Phys. Fluids A **3**, 1312 (1991).

[22] X. L. Li, Phys. Fluids **8**, 336 (1996).

[23] O. M. Belotserkovskiĭ, *Numerical Simulation in the Mechanics of Continuous Media* [in Russian] (Fizmatlit, Moscow, 1994).

[24] O. M. Belotserkovskiĭ, *Numerical Experiments in Turbulence: From Order to Chaos* [in Russian] (Nauka, Moscow, 1994).

[25] O. M. Belotserkovskiĭ, V. A. Gushchin, and V. N. Kon'shin, Zh. Vychisl. Mat. Mat. Fiz. **27**, 594 (1987).

Translated by M. E. Alferieff

The correction-to-scaling exponent in dilute systems

R. Folk*[)]

Institute for Theoretical Physics, University of Linz, A-4040 Linz, Austria

Yu. Holovatch

Institute for Condensed Matter Physics, Ukrainian Academy of Sciences, UA-290011 Lvov, Ukraine

T. Yavors'kii

Ivan Franko Lvov State University, UA-290005 Lvov, Ukraine

The leading correction-to-scaling exponent ω for the three-dimensional (3D) dilute Ising model is calculated in the framework of the field theoretic renormalization group approach. Both in the minimal subtraction scheme and in the massive field theory (resummed four-loop expansion) excellent agreement with recent Monte Carlo calculations (H. G. Ballesteros *et al.*, Phys. Rev. B **58**, 2740 (1998)) is achieved. The expression of ω as a series in a $\sqrt{\varepsilon}$ expansion up to $\mathcal{O}(\varepsilon^2)$ does not permit a reliable estimate for $d=3$. © *1999 American Institute of Physics.* [S0021-3640(99)00610-6]

PACS numbers: 75.10.Hk, 64.60.Ak, 05.50.+q

From renormalization group (RG) theory one knows that in the asymptotic region the values of the critical exponents are universal and scaling laws between them hold. There the couplings of the model Hamiltonian describing the critical system have reached their fixed-point values. In the nonasymptotic region deviations from the fixed-point values are present. They die out according to a universal power law governed by the correction-to-scaling exponent ω. For example, for the zero-field susceptibility the approach from above to the critical temperature T_c is characterized by the so-called Wegner expansion[1]

$$\chi \simeq \Gamma_0 \tau^{-\gamma}(1 + \Gamma_1 \tau^{\omega/\nu} + \Gamma_2 \tau^{2\omega/\nu} + \dots), \tag{1}$$

where $\tau = (T - T_c)/T_c$ and the Γ_i are the nonuniversal amplitudes, and γ and ν are the asymptotic values of the susceptibility and correlation-length critical exponents. The smaller the exponent ω, the larger is the region where corrections to the asymptotic power laws have to be taken into account. Even further away from the fixed point it is necessary to consider the complete nonlinear crossover functions. This exponent has been calculated with high accuracy for the $O(n)$ symmetric model (in particular for the three-dimensional (3D)-Ising model, see Table I), but is much less known for the corresponding diluted model. As a result of a 3D calculation of the field theoretic functions within

TABLE I. Values of correction-to-scaling exponent ω as obtained from different methods in dilute and pure 3D Ising models

Method	Dilute	Pure
scaling field	0.42 Ref. 10	0.87 Ref. 10
ε expansion	see text	0.814 ± 0.018 Ref. 23
massive RG, $d=3$	0.372	0.799 ± 0.011 Ref. 23
min. sub. RG, $d=3$	0.390	0.791
MC	0.37 ± 0.06 Ref. 8	0.8 ± 0.1 Ref. 16, 0.8–0.85 Ref. 24 0.87 ± 0.09 Ref. 25

Note: For the accuracy of our values see text and Fig. 1.

the minimal subtraction scheme[2] and a thorough analysis of different methods for calculating critical exponents,[3] we are able to present accurate values of the correction-to-scaling exponent for weakly diluted quenched 3D Ising model.

Ascertaining the implications of quenched dilution for the critical behavior is a long-standing problem attracting theoretical, experimental, and numerical efforts. In the 3D Ising model quenched disorder causes the asymptotic critical exponents to differ from the pure values.[4,5] In principle this statement should hold for arbitrary weak dilution. But in order to observe this change one must approach close enough to the critical point. The width of the corresponding region turns out to be dilution dependent.

In particular, Monte Carlo (MC) calculations of the critical exponents in the dilute 3D Ising model are more difficult to perform than for the pure model, since they require much larger lattice sizes.[6] Even on the larger lattices the exponents were found to be nonuniversal and continuously varying with dilution, i.e., they were effective exponents.[7] It became clear that a correction-to-scaling analysis is unavoidable and indeed has led to universal exponents.[8] Without it one still obtains concentration-dependent effective exponents.[9]

The value of the correction-to-scaling exponent ω found in MC calculations from an analysis invoking the first correction term in (1) turned out to be[8]

$$\omega = 0.37 \pm 0.06. \tag{2}$$

Thus it is almost half as large as its corresponding value in the pure model (see Table I), and this smallness of ω in the dilute case explains its importance for an analysis of the asymptotic critical behavior. It is therefore highly desirable to have an independent quantitative theoretical prediction for the value of the correction-to-scaling exponent in the dilute system.

In theoretical calculations the value of ω found by a scaling-field RG analysis[10] is $\omega = 0.42$. So far field theoretical RG studies have concentrated mainly on the asymptotic values of the leading exponents. Correction-to-scaling exponents have been calculated within the massive RG in the two-loop approximation in Ref. 11 ($\omega = 0.450$) and within the minimal subtraction scheme in the three-loop approximation in Ref. 12 ($\omega = 0.366$). Here, we improve this value in the massive RG scheme up to four-loop order, with the result

$$\omega = 0.372 \tag{3}$$

in excellent agreement with (2). In the minimal subtraction scheme we obtain $\omega = 0.390$, which lies within the bandwidth of MC accuracy.

The critical behavior of the quenched weakly dilute Ising model in the Euclidian space of $d = 4 - \varepsilon$ dimensions is governed by a Hamiltonian with two couplings:[13]

$$\mathcal{H}(\phi) = \int d^d R \left\{ \frac{1}{2} \sum_{\alpha=1}^{n} [|\nabla \phi_\alpha|^2 + m_0^2 \phi_\alpha^2] - \frac{v_0}{4!} \left(\sum_{\alpha=1}^{n} \phi_\alpha^2 \right)^2 + \frac{u_0}{4!} \sum_{\alpha=1}^{n} \phi_\alpha^4 \right\}, \tag{4}$$

in the replica limit $n \to 0$. Here ϕ_α are the components of order parameter; $u_0 > 0$, $v_0 > 0$ are bare couplings; m_0 is the bare mass.

We describe the long-distance properties of the model (4) in the vicinity of the phase transition point using a field-theoretical RG approach. The results presented in this paper are obtained on the basis of two different RG schemes: the normalization conditions of massive renormalized theory at fixed[14] $d = 3$, and the minimal subtraction scheme.[15] The last approach allows both fixed $d = 3$ calculations[16] and an ε expansion.

In the RG method the change of the couplings u and v under renormalization is described by two β functions

$$\beta_u(u,v) = \mu \left(\frac{\partial u}{\partial \mu} \right)_0, \quad \beta_v(u,v) = \mu \left(\frac{\partial v}{\partial \mu} \right)_0, \tag{5}$$

where μ corresponds to the mass in the massive field theory approach and to the scale parameter in the minimal subtraction scheme. The subscript in (5) indicates that the derivatives are taken at constant unrenormalized parameters. The β functions differ for different RG schemes and in consequence the fixed-point coordinates u^*, v^*, defined by the simultaneous zeros of both β functions, are scheme dependent. The asymptotic critical exponents as well as the correction-to-scaling exponent do not depend on the RG scheme and take universal values.

The correction-to-scaling exponent ω is defined by the smallest eigenvalue of the matrix of derivatives of the β functions

$$\begin{pmatrix} \dfrac{\partial \beta_u}{\partial u} & \dfrac{\partial \beta_u}{\partial v} \\ \dfrac{\partial \beta_v}{\partial u} & \dfrac{\partial \beta_v}{\partial v} \end{pmatrix} \tag{6}$$

taken at the stable fixed point. For the stable fixed point both eigenvalues of this matrix have a positive real part.

Our results for the correction-to-scaling exponent are based on the known high-order expansions for the functions β_u and β_v. In the massive scheme they are known in the four-loop approximation.[17] In the minimal subtraction scheme one can obtain these functions in the five-loop approximation in the replica limit from those of a cubic model.[2] In the limiting case of the pure model only the coupling u is present. The corresponding β-function results from putting $v = 0$ in $\beta_u(u,v)$, and the correction-to-scaling exponent is simply the derivative $\partial \beta_u(u,0)/\partial u$ taken at the stable fixed point u^*. Note that for the

pure model the β functions in the massive scheme are known in the six-loop approximation,[18] and the five-loop results for the RG functions in the minimal subtraction scheme[19] agree with those recovered from Ref. 2.

It is known that the series obtained in the perturbational RG approach are at best asymptotic (for the dilute model see, however, Ref. 20). An appropriate resummation procedure has to be applied to the β functions in order to obtain reliable information. The choice of the resummation procedure depends on the information about the high-order behavior of the series expansion. This information is not available for the case of the β functions (5). In this situation we have used in our analysis several resummation procedures. In particular we tried Padé–Borel resummation[18] for resolvent series[21] as well as the Chisholm–Borel resummation technique.[11,22] Simple Padé tables were analyzed as well. In that case special attention was paid to the choice of the fitting parameter (in the Borel–Leroy transform). We observed the standard ''benchmarks,'' namely, fastest convergence of the perturbation theory results and reproducibility of the best accuracy known for the exponent values of the pure model. Moreover, different forms of the approximants were tried and analyzed on the basis of a model function.[3]

The steps which we follow in the calculation of the correction-to-scaling exponent ω are the following: First the β functions (5) are resummed and the system of equations for the fixed points, $\beta_u(u^*,v^*)=0$, $\beta_v(u^*,v^*)=0$, is solved. Then the matrix of derivatives (6) is calculated for the resummed β functions. The stability of the fixed points is checked. The fixed point with both $u^*\neq0$ and $v^*\neq0$ is the stable one at $d=3$, and the smallest eigenvalue gives the desired correction-to-scaling exponent. Note that the eigenvalues might be complex, in which case both have the same positive real part defining ω.

In Fig. 1 we present our results for the exponent ω obtained in successive orders of perturbation theory in the number of loops. To perform the resummation, the Borel transforms of the truncated lth-order perturbation theory expansion for the β functions were presented in the form of $[(l-1)/1]$ rational approximants of two variables.[22] This form of rational approximants appeared to give the most reliable results. The four-loop results for the exponent ω obtained in the two RG schemes are given in the second column of Table I. The behavior of ω in successive numbers of loops shown in Fig. 1. The uncertainty in ω may be estimated by taking the difference between the four-loop and three-loop results. In all cases it gives a typical accuracy of lower then 10%. Although the two RG schemes lead to comparable values for ω, the convergence of the values in the massive scheme is much faster. Note that the result for ω combined with the corresponding four-loop results for the asymptotic critical exponents[17,26] confirms the conjectured inequality for the random-model critical exponents, $-\nu\omega<\alpha<0$, where α is the specific-heat exponent.[27]

As was noted above, five-loop results for the minimal subtraction scheme are available.[2] In particular applying the resummation scheme[28] to the pure Ising model case, $v=0$, we get the following values for ω with increasing number of loops, starting from two loops: $\omega=0.566$; 0.852; 0.756; 0.791. This leads to an improvement in accuracy of the previously calculated $d=3$ five-loop value[16] (see the third column of Table I).

The degeneracy of the dilute Ising model β functions at the one-loop level leads to the $\sqrt{\varepsilon}$ expansion.[13,29] For the critical exponents this expansion is known[30] up to $\mathcal{O}(\varepsilon^2)$. Starting from the five-loop results of Ref. 2 in the replica limit, we get the following
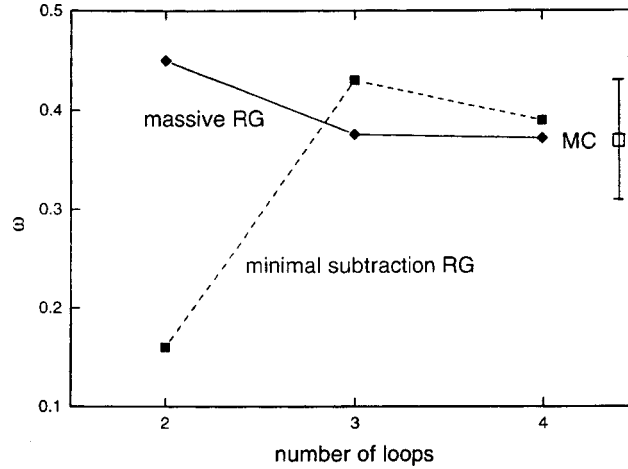
FIG. 1. Correction-to-scaling exponent ω of the dilute 3D Ising model for increasing number of loops. The open square with error bar shows the region of accuracy of the MC data,[8] the filled squares show our values in the minimal subtraction RG scheme, and the filled diamonds our values in the massive RG scheme.

expansions[31] for the eigenvalues ω_1 and ω_2 of the stability matrix (5) at the fixed point $u^* \neq 0$, $v^* \neq 0$:

$$\omega_1 = 2\,\varepsilon + 3.704011194\,\varepsilon^{3/2} + 11.30873837\,\varepsilon^2, \tag{7}$$

$$\omega_2 = 0.6729265850\,\varepsilon^{1/2} - 1.925509085\,\varepsilon - 0.5725251806\,\varepsilon^{3/2} - 13.93125952\,\varepsilon^2.$$

From naively adding the successive perturbational contributions one observes that ω_2 becomes negative already in the three-loop approximation ($\sim \varepsilon$), and therefore *no stable fixed point* exists in the strict $\sqrt{\varepsilon}$ expansion. Even the resummation procedures we applied above do not change this picture.[26] This can be considered as indirect evidence that the $\sqrt{\varepsilon}$ expansion is not Borel summable, as may be expected from Ref. 20. A physical reason might be the existence of the Griffith singularities caused by the zeros of the partition function of the pure system.[32] The fixed-d approach, both within the massive[14] and minimal subtraction[15,16] schemes, seems to be the only reliable way to study the critical behavior of the model by means of the RG technique.

We acknowledge valuable correspondence with Alan J. McKane and Victor Martín-Mayor.

*)e-mail: folk@tphys.uni-linz.ac.at

[1] F. J. Wegner, Phys. Rev. B **5**, 4529 (1972).
[2] H. Kleinert and V. Schulte-Frohlinde, Phys. Lett. B **342**, 284 (1995).
[3] Details will be published elsewhere.
[4] A. B. Harris, J. Phys. C **7**, 1671 (1974).
[5] J. T. Chayes, L. Chayes, D. S. Fisher *et al.*, Phys. Rev. Lett. **57**, 2999 (1986).
[6] D. P. Landau, Phys. Rev. B **22**, 2450 (1980); J. Marro, A. Labarta, and J. Tejada, Phys. Rev. B **34**, 347 (1986).

[7] J.-S. Wang and D. Chowdhury, J. Phys. France **50**, 2905 (1989); J.-S. Wang, M. Wöhlert, H. Mühlenbein *et al.*, Physica A **166**, 173 (1990); H.-O. Heuer, Europhys. Lett. **12**, 551 (1990); H.-O. Heuer, Phys. Rev. B **42**, 6476 (1990); H.-O. Heuer, J. Phys. A **26**, L333 (1993).

[8] H. G. Ballesteros, L. A. Fernández, V. Martín-Mayor *et al.*, Phys. Rev. B **58**, 2740 (1998).

[9] S. Wiseman and E. Domany, Phys. Rev. Lett. **81**, 22 (1998); Phys. Rev. E **58**, 2938 (1998).

[10] K. E. Newman and E. K. Riedel, Phys. Rev. B **25**, 264 (1982).

[11] J. Jug, Phys. Rev. B **27**, 609 (1983).

[12] H. K. Janssen, K. Oerding, and E. Sengespeick, J. Phys. A **28**, 6073 (1995).

[13] G. Grinstein and A. Luther, Phys. Rev. B **13**, 1329 (1976); T. C. Lubensky, Phys. Rev. B **11**, 3573 (1975).

[14] G. Parisi, *Proceedings of the Cargèse Summer School 1973* (unpublished); J. Stat. Phys. **23**, 49 (1980).

[15] G. t'Hooft and M. Veltman, Nucl. Phys. B **44**, 189 (1972).

[16] R. Schloms and V. Dohm, Europhys. Lett. **3**, 413 (1987); Nucl. Phys. B **328**, 639 (1989).

[17] I. O. Mayer, A. I. Sokolov, and B. N. Shalaev, Ferroelectrics **95**, 93 (1989); I. O. Mayer, J. Phys. A **22** 2815 (1989).

[18] G. B. Baker, B. G. Nickel, and D. I. Meiron, Phys. Rev. B **17**, 1365 (1978).

[19] H. Kleinert, J. Neu, V. Schulte-Frohlinde *et al.*, Phys. Lett. B **272**, 39 (1991); Phys. Lett. B **319**, 545(E) (1993).

[20] A. J. Bray, T. McCarthy, M. A. Moore *et al.*, Phys. Rev. B **36**, 2212 (1987); A. J. McKane, Phys. Rev. B **49**, 12003 (1994).

[21] P. J. S. Watson, J. Phys. A **7**, L167 (1974).

[22] J. S. R. Chisholm, Math. Comput. **27**, 841 (1973).

[23] R. Guida and J. Zinn-Justin, J. Phys. A **31**, 8103 (1998).

[24] C. F. Baillie, R. Gupta, K. A. Hawick *et al.*, Phys. Rev. B **45**, 10438 (1992).

[25] H. G. Ballesteros, L. A. Fernández, V. Martín-Mayor *et al.*, J. Phys. A **32**, 1 (1999).

[26] R. Folk, Yu. Holovatch, and T. Yavors'kii, J. Phys. Stud. **2**, 213 (1998) and unpublished.

[27] A. Aharony, A. B. Harris, and S. Wiseman, Phys. Rev. Lett. **81**, 252 (1998).

[28] In this case the Padé–Borel resummation based on the $[(l-1)/1]$ Padé approximant for the Borel transform is recovered.

[29] D. E. Khmel'nitskii, Zh. Éksp. Teor. Fiz. **68**, 1960 (1975) [Sov. Phys. JETP **41**, 981 (1975)].

[30] B. N. Shalaev, S. A. Antonenko, and A. I. Sokolov, Phys. Lett. A **230**, 105 (1997).

[31] Up to $\mathcal{O}(\varepsilon)$ we recover the result of C. Jayaprakash and H. J. Katz, Phys. Rev. B **16**, 3987 (1977), the $\sqrt{\varepsilon}$ term is twice as large as in B. N. Shalaev, Zh. Éksp. Teor. Fiz. **73**, 2301 (1977) [Sov. Phys. JETP **46**, 1204 (1977)].

[32] R. B. Griffith, Phys. Rev. Lett. **23**, 17 (1969).

On the role of the Coulomb interaction in the mechanism of *d*-wave Cooper pairing of charge carriers in high-T_c superconductors

É. A. Pashitskiĭ, V. I. Pentegov, and A. V. Semenov

Institute of Physics, Ukrainian National Academy of Sciences, 252650 Kiev, Ukraine

E. Abraham

Heriot-Watt University, Edinburgh, UK

The question of the effect of the structure of the anisotropic quasi-two-dimensional electron spectrum of high-T_c superconductors on the character of the screening of the Coulomb interaction and the symmetry of the superconducting order parameter is studied. Calculations of the polarization operator of electrons are performed on the basis of the single-particle band spectrum extracted from angle-resolved photoemission spectroscopy data. It is shown that the static screened Coulomb repulsion has a minimum at small momentum transfers. This corresponds to an effective electron–electron attraction in the $d_{x^2-y^2}$-wave channel of Cooper pairing of the charge carriers on account of their interaction with the long-wavelength charge-density fluctuations. This attraction together with the anisotropic electron–phonon interaction increase the critical superconducting transition temperature T_c with increasing hole density and can give quite high values of T_c while at the same time suppressing the isotope effect, in qualitative agreement with the experimental data for underdoped hole-type cuprate metal-oxide compounds. © *1999 American Institute of Physics.* [S0021-3640(99)00710-0]

PACS numbers: 74.20.Mn, 74.72.−h

1. As numerous angle-resolved photoelectron spectroscopy experiments (ARPES method) show,[1–4] in the quasi-two-dimensional band spectrum of layered crystals of optimally doped hole-type cuprate metal-oxide compounds (MOCs), so-called ''flat'' bands, or extended saddle features (SFs), with anomalously weak dispersion in the direction of the principal crystallographic axes *a* and *b* in the plane of the conducting CuO_2 layers, are observed near the Fermi level. As a result, the Fermi velocity $\mathbf{v}_F(\mathbf{k})$ on a closed cylindrical Fermi surface (FS) centered at a corner of the first Brillouin zone (BZ) can be strongly anisotropic in the $a-b$ plane, and the density of states (DOS) near extended SFs can possess logarithmic or square-root Van Hove singularities (VHSs).[5,6]

It can be shown that a strong anisotropy of the single-electron spectrum and of $\mathbf{v}_F(\mathbf{k})$ in the plane of the layers leads to anomalies in the collective electron spectrum,

specifically, the existence of a weakly damped branch of collective electron-density oscillations with quasiacoustic dispersion that is similar to the acoustic plasmon branch in multiband metals.[7,8]

Indeed, let us consider the long-wavelength limit ($q_\parallel \to 0$) of the random-phase approximation (RPA), in which the electron polarization operator (PO) at zero temperature ($T=0$) can be represented as

$$\Pi(\mathbf{q}_\parallel, \omega) = -\frac{1}{2\pi^2} \int d^2 k_\parallel \delta(E(\mathbf{k}_\parallel) - E_F) \frac{\mathbf{q}_\parallel \cdot \mathbf{v}(\mathbf{k}_\parallel)}{\omega - \mathbf{q}_\parallel \cdot \mathbf{v}(\mathbf{k}_\parallel) + i\eta} (\eta \to 0^+), \tag{1}$$

where $\mathbf{q}_\parallel$ is the longitudinal momentum transfer in the $a-b$ plane, $\mathbf{v}((\mathbf{k}_\parallel) = \nabla_{\mathbf{k}_\parallel} E(\mathbf{k}_\parallel)$ is the group velocity of quasiparticles with a 2D dispersion law $E(\mathbf{k}_\parallel)$, and the Fermi energy E_F in the argument of the δ function determines the position of the Fermi level relative to the conduction-band bottom. As an example, we shall consider a simple model of a 2D metal with a cylindrical FS with a circular cross section and Fermi velocity anisotropy $\mathbf{v}_F(\varphi)$, whose dependence on the angle φ between the Fermi momentum $\mathbf{k}_F$ and the crystallographic a axis for C_{4v} symmetry of the spectrum can be approximated by the step function

$$\mathbf{v}_F(\varphi) = \begin{cases} \mathbf{v}_1, & 0 < \varphi \leq \varphi_0; \\ \mathbf{v}_2, & \varphi_0 < \varphi \leq \pi/4, \end{cases} \tag{2}$$

where the angle φ_0 lies in the range $0 < \varphi_0 < \pi/4$. Performing the integration in Eq. (1), for $\mathbf{v}_1 \ll \omega/q \ll \mathbf{v}_2$ and $\varphi_0 = \pi/8$ we obtain the following expression for the real part of the PO:

$$\mathrm{Re}\Pi(\mathbf{q}_\parallel, \omega) \approx \frac{k_F}{2\pi\mathbf{v}_1} \left(1 - \frac{q_\parallel^2 \mathbf{v}_1 \cdot \mathbf{v}_2}{2\omega^2} \right). \tag{3}$$

In the limit $q_\parallel \to 0$ the zeros of $\mathrm{Re}\Pi(\mathbf{q}_\parallel, \omega)$ coincide with the zeros of the real part of the permittivity $\epsilon(\mathbf{q}, \omega) = 1 + V_c(\mathbf{q})\Pi(\mathbf{q}, \omega)$, and they therefore determine the dispersion of the collective electron-density oscillations. Therefore it follows from Eq. (3) that even for a simply connected FS with quite strong anisotropy of the spectrum ($\mathbf{v}_1 \ll \mathbf{v}_2$) there can exist a collective branch with acoustic dispersion,

$$\omega_{pl}(q_\parallel) \approx q_\parallel \sqrt{\mathbf{v}_1 \cdot \mathbf{v}_2/2}, \tag{4}$$

corresponding to quasineutral electron-density oscillations with opposite phases on the sections of the FS with different Fermi velocity and similar to the acoustic plasmon branch in metals with a multiply connected FS.[7,8]

Figure 1 shows the dependence of the real and imaginary parts of the PO (1) on the ratio $\omega/q_\parallel$ for $\mathbf{v}_2/\mathbf{v}_1 = 5$. The acoustic plasmon branch corresponds to a zero of $\mathrm{Re}\Pi(\omega/q_\parallel)$ at the point where $\mathrm{Im}\Pi(\omega/q_\parallel)$ is minimum. The spectral function of the charge-density fluctuations

$$S_{pl}(\mathbf{q}, \omega) = -\frac{1}{\pi} \mathrm{Im}\epsilon^{-1}(\mathbf{q}, \omega) \tag{5}$$

possesses a low-frequency (LF) peak as well as a high-frequency (HF) plasma peak and depends linearly on ω as $\omega \to 0$ (see inset in Fig. 1).

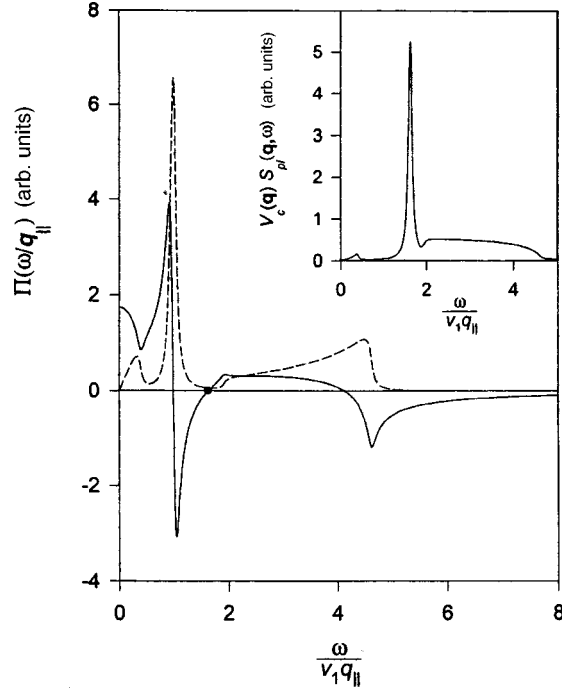FIG. 1. Real and imaginary parts of the polarization operator in the long-wavelength limit $\mathbf{q}_\parallel \to 0$ as a function of $\omega/q_\parallel$ for $q_\parallel$ directed along the a axis with the Fermi velocity ratio $\mathbf{v}_2/\mathbf{v}_1 = 5$ and $\varphi_0 = \pi/8$ [see Eq. (2)]. The filled dot shows the position of the zero of $\mathrm{Re}\Pi(\omega/q_\parallel)$, determining an acoustic plasmon. Inset: corresponding low-frequency peak of the spectral function $S_{pl}(\mathbf{q}, \omega)$ of charge-density fluctuations, multiplied by the Coulomb matrix element.

2. On the basis of the Kramers–Kronig relation for $\epsilon^{-1}(\mathbf{q}, \omega)$ the matrix element of the static ($\omega = 0$) screened Coulomb repulsion between electrons can be represented as

$$\widetilde{V}_c(\mathbf{q}) = \frac{V_c(\mathbf{q})}{\epsilon(\mathbf{q},0)} = V_c(\mathbf{q})\left[1 - 2\int_0^\infty \frac{d\omega}{\omega} S_{pl}(\mathbf{q},\omega)\right], \tag{6}$$

where V_c is the matrix element of the unscreened Coulomb interaction in a layered crystal with spacing d between the layers and is calculated in the plane-wave approximation as

$$V_c(\mathbf{q}) = \frac{2\pi e^2 d}{q_\parallel} \frac{\sinh q_\parallel d}{\cosh q_\parallel d - \cos q_z d}, \tag{7}$$

where q_z is the transverse momentum transfer (along the c axis). Since the acoustic plasmon branch and the corresponding LF peak in $S_{pl}(\mathbf{q}, \omega)$ exist for small $q_\parallel$ (the width of this region is determined by the size of the extended SFs with a high DOS), while the existence region of the undamped HF-plasmon branch and the corresponding peak in $S_{pl}(\mathbf{q}, \omega)$ is also limited on the high-momentum side $q_\parallel \lesssim k_F$, it follows from Eq. (6) that the static screened Coulomb repulsion should be suppressed for small $q_\parallel$ all the more strongly, the greater the contribution of LF and HF peaks in the spectral function to the
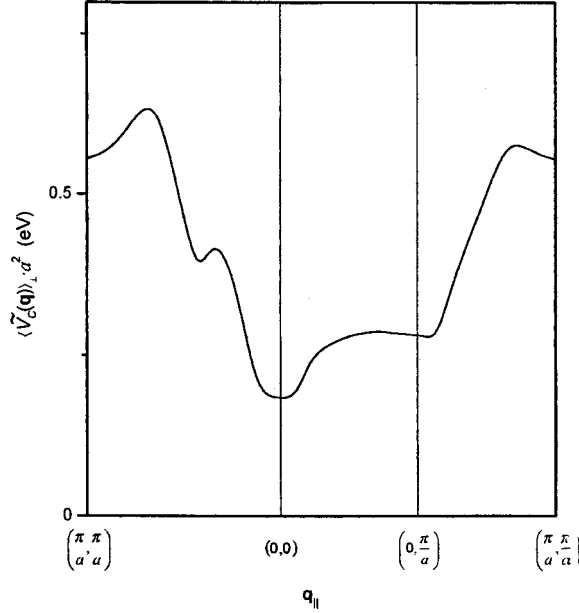
FIG. 2. Matrix element of the screened Coulomb interaction $\tilde{V}_c(\mathbf{q})$, averaged over q_z in the range $(-\pi/d, \pi/d)$, as a function of $\mathbf{q}_\parallel$ along the principal directions in the BZ.

integral over ω is. Figure 2 shows $\tilde{V}_c(\mathbf{q}) \equiv V_c(\mathbf{q})(1 + V_c(\mathbf{q})\Pi(\mathbf{q},0))^{-1}$ as a function of $\mathbf{q}_\parallel$. This function was calculated for the upper (antibonding) branch of the empirical band spectrum, extracted in Ref. 4 from ARPES data for a $YBa_2Cu_3O_{7-\delta}$ crystal, under the condition that the Fermi level lies near extended SFs (Fig. 3). We note that in this case, on account of the high DOS the condition $V_c(\mathbf{q})\Pi(\mathbf{q},0) \gg 1$ holds in the entire volume of the BZ, so that to a high degree of accuracy $\tilde{V}_c(\mathbf{q}_\parallel) \approx 1/\Pi(\mathbf{q}_\parallel,0)$. This makes it possible to neglect the difference of expression (7) from the exact Coulomb matrix element calculated using Bloch functions.

As we can see, the screened Coulomb interaction $\tilde{V}_c(\mathbf{q})$ possesses a minimum for small $\mathbf{q}_\parallel$, which, similarly to the repulsion maximum at the corner of the BZ for $\mathbf{q}_\parallel = (\pi/a, \pi/a)$ (Ref. 9) or the attraction maximum at the center of the BZ for $\mathbf{q}_\parallel = 10$ (Ref. 10), leads to an effective electron–electron attraction in the d-wave channel of Cooper pairing.

Near the critical temperature $(T \to T_c)$ the linearized equation for the anisotropic gap $\Delta(\mathbf{k}_\parallel, \omega)$ on the cylindrical FS, taking the retarded interaction of electrons with phonons and with charge-density fluctuations into account in the tight-binding approximation,[11] can be written in the form
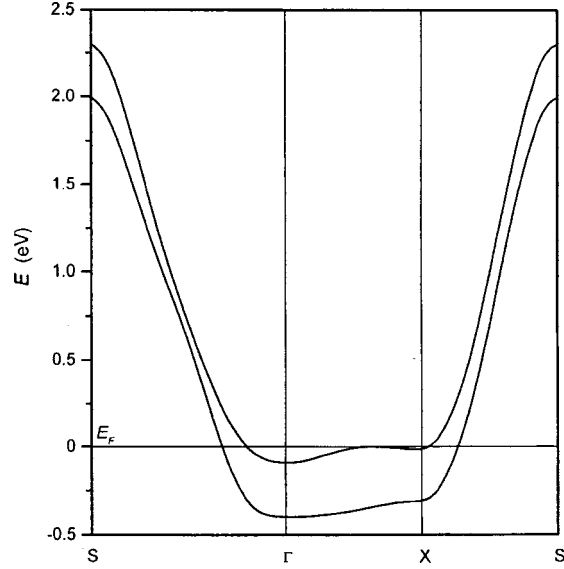
FIG. 3. Empirical dispersion law obtained in Ref. 4 for the lower (bonding) and upper (antibonding) branches of the band spectrum along the principal directions in the BZ.

$$(1+\lambda_{\mathrm{ph}}(\mathbf{k}_\parallel))\Delta(\mathbf{k}_\parallel,0) = -\int \frac{d^2 k'_\parallel}{(2\pi)^2} \int_{-\infty}^{\infty} \frac{d\omega}{2\pi} \mathrm{Im}\left[\frac{\Delta(\mathbf{k}'_\parallel,\omega)}{\omega^2 - \xi^2(\mathbf{k}'_\parallel) + i\eta}\right]$$

$$\times \left\{ \int_0^{\infty} d\Omega [\langle g_{\mathrm{ph}}^2(\mathbf{k},\mathbf{k}';\Omega)\rangle_\perp S_{\mathrm{ph}}(\Omega)\langle V_c(\mathbf{k}-\mathbf{k}')S_{pl}(\mathbf{k}-\mathbf{k}';\Omega)\rangle_\perp]\right.$$

$$\times \left[\frac{\tanh(\omega/2T_c)+\coth(\Omega/2T_c)}{\Omega+\omega-i\eta} + \frac{\tanh(\omega/2T_c)-\coth(\Omega/2T_c)}{\Omega-\omega+i\eta}\right]$$

$$\left. -\langle V_c(\mathbf{k}-\mathbf{k}')\rangle_\perp \tanh\frac{\omega}{2T_c}\right\}. \tag{8}$$

Here $\xi(\mathbf{k}_\parallel) \equiv E(\mathbf{k}_\parallel) - E_F$ is the quasiparticle energy, measured from the Fermi level E_F; g_{ph} is the matrix element of the electron–phonon interaction (EPI); $S_{\mathrm{ph}}(\Omega)$ is the photon spectral function; λ_{ph} is the dimensionless EPI constant determining the normalization effects:

$$\lambda_{\mathrm{ph}}(\mathbf{k}_\parallel) = \int \frac{d^2 k'_\parallel}{(2\pi)^2} [W_{\mathrm{ph}}(\mathbf{k}_\parallel,\mathbf{k}'_\parallel)]\delta(\xi(\mathbf{k}'_\parallel)), \tag{9}$$

$$W_{\mathrm{ph}}(\mathbf{k}_\parallel,\mathbf{k}'_\parallel) = 2\int_0^{\tilde{\Omega}_{\mathrm{ph}}} \frac{d\Omega}{\Omega} \langle g_{\mathrm{ph}}^2(\mathbf{k},\mathbf{k}';\Omega)\rangle_\perp S_{\mathrm{ph}}(\Omega); \tag{10}$$

$\tilde{\Omega}_{\mathrm{ph}}$ is the maximum frequency of the phonon spectrum; and, the brackets $\langle\ldots\rangle_\perp$ denote averaging over the transverse component of the momentum along the c axis.

Since the characteristic frequencies in $S_{ph}(\Omega)$ and $S_{pl}(\mathbf{k}_{\parallel} - \mathbf{k}'_{\parallel};\Omega)$ are much higher than T_c, the low-frequency range $\omega \ll \Omega$ makes the main contribution to the integral over ω in Eq. (8), so that ω can be neglected in the denominators $[\Omega \pm \omega \mp i\eta]^{-1}$. As a result, performing the integration over ω, switching from integration over $\mathbf{k}'_{\parallel}$ to integration over $\xi \equiv \xi(\mathbf{k}'_{\parallel})$ and over the angle φ' between $\mathbf{k}'_{\parallel}$ and the a axis, and using the relation (6) we write Eq. (8) in the angular variables φ and φ':

$$(1 + \lambda_{ph}(\varphi))\Delta(\varphi) = \frac{1}{2}\int_0^{2\pi} d\varphi' \Delta(\varphi') \int_{-E_F}^{E_F} \frac{d\xi}{\xi} \nu(\varphi',\xi)$$

$$\times [W_{ph}(\varphi,\varphi')\theta(\widetilde{\Omega}_{ph} - |\xi|) - \widetilde{V}_c(\varphi,\varphi')]\tanh\frac{\xi}{2T_c}, \qquad (11)$$

where $\nu(\varphi,\xi)$ is the anisotropic DOS, which, when the C_{4v} symmetry of the spectrum is taken into account, can be approximated by the expression

$$\nu(\varphi,\xi) = \nu_+(\xi) + \nu_-(\xi)\cos 4\varphi, \quad \nu_\pm(\xi) = \frac{1}{2}[\nu_1(\xi) \pm \nu_2(\xi)]. \qquad (12)$$

Here $\nu_1(\xi)$ and $\nu_2(\xi)$ correspond to the values of the DOS

$$\nu(\xi) \equiv \frac{k_{\parallel}}{2\pi}|\nabla_{\mathbf{k}_{\parallel}}E(\mathbf{k}_{\parallel})|^{-1}$$

along directions determined by the angles $\varphi = 0$ and $\varphi = \pi/4$. In the integrand in Eq. (11), the functions $\Delta(\varphi',\xi)$, $W_{ph}(\varphi,\varphi',\xi)$, and $\widetilde{V}_c(\varphi,\varphi',\xi)$, which are smooth as a function of ξ, are replaced by their values on the FS ($\xi = 0$).

In the subsequent numerical calculations the spectrum $E(\mathbf{k}_{\parallel})$ corresponding to the upper branch of the empirical band spectrum is used (see Fig. 3). We note that according to the experimental data[4] the Fermi level lies ~ 0.12 eV above extended SFs. However, as noted in Ref. 12, this could be due to the presence of an unneutralized charge on the surface of the sample, giving rise to a substantial shift of the electrochemical potential in near-surface layers; this shift should contribute a systematic error in the ARPES determination of the position of the Fermi level. Recently, such a surface charge has been observed experimentally in small YBaCuO granules.[13] Analysis of other experiments (specifically, inelastic neutron scattering[12]) shows that the VHSs lie much closer to the Fermi level. In this connection, the subsequent calculations are performed for different positions of the Fermi level near extended SFs.

3. Following the method proposed in Ref. 14, we shall solve Eq. (11) by expanding the matrix elements $W_{ph}(\varphi,\varphi')$, $\widetilde{V}_c(\varphi,\varphi')$ and the gap $\Delta(\varphi)$ in Fourier series in φ and φ'. For this, we represent Eq. (11) in the form

$$\Delta(\varphi) = \int_0^{2\pi} \frac{d\varphi'}{2\pi} K(T_c;\varphi,\varphi')\Delta(\varphi'), \qquad (13)$$

where the kernel $K(T_c;\varphi,\varphi')$ corresponds to the integral over ξ in Eq. (11), divided by $(1 + \lambda_{ph}(\varphi))$.

The critical superconducting transition temperature T_c is determined from the condition that the maximum eigenvalue of the kernel $K(T_c;\varphi,\varphi')$ is equal to 1. A numerical

solution of Eq. (13) shows that in the absence of the EPI the screened Coulomb repulsion with a minimum at small $\mathbf{q}_\parallel$ (see Fig. 2), which, as follows from Eq. (6), is due to the interaction of electrons with charge-density fluctuations, can itself give Cooper pairing in the d-wave channel. Here the symmetry of the superconducting gap corresponds to the irreducible B_1 representation of the C_{4v} group:

$$\Delta(\varphi) = \sum_{n=1}^{\infty} a_{4n-2} \cos(4n-2)\varphi, \tag{14}$$

where the first two Fourier coefficients a_2 and a_6 play the main role.

It should be underscored that the quite strong anisotropy of the matrix element $\widetilde{V}_c(\varphi, \varphi')$ is due mainly to the dependence of the screened Coulomb repulsion on the momentum transfer, while the anisotropy of the phonon spectrum and the EPI are determined by the symmetry of the crystal lattice. As noted in Ref. 15, the HF phonon mode with frequency $\Omega_O \approx 600$ cm^{-1}, corresponding to the vibrations of apical oxygen (along the c axis) and giving rise to Cooper pairing with $d_{x^2-y^2}$ symmetry of the superconducting gap, makes a large contribution to the EPI. For this reason, in what follows, together with the isotropic components of the EPI, the presence of an anisotropic component, whose constant was assumed to be $\lambda_{ph}^d = 0.3$ in accordance with the estimates made in Ref. 15, was also taken into account.

At the same time the isotropic EPI constant, which appears in the renormalization factor $Z(0) = 1 + \lambda_{ph}^0$, was chosen as $\lambda_{ph}^0 = 0.44$, so that as the Fermi level approaches extended SFs in the band spectrum, the value of T_c obtained with both the EPI anisotropy and the interaction of electrons with charge-density fluctuations taken into account would be $T_c \approx 100$ K for values of the EPI cutoff and Coulomb interaction energies $\widetilde{\Omega}_{ph} = \Omega_O \approx 900$ K and $E_F \approx 1100$ K, respectively. The dimensionless constant of the anisotropic component of the Coulomb interaction corresponding to the d-wave pairing is $\lambda_c^d = 0.28$.

We note that for the band spectrum considered here the isotropic constant of the screened Coulomb interaction is quite large and is $\mu_c \equiv \lambda_c^0 \approx 0.5 - 0.8$, depending on the position of the Fermi level. Since in the presence case the Bogolyubov–Tolmachev logarithm $\ln(E_F/\widetilde{\Omega}_{ph})$ is small, μ_c does not decrease (in contrast to the Morel–Anderson pseudopotential in ordinary superconductors), so that the isotropic Coulomb repulsion constant is always greater than λ_{ph}^0, and s-wave Coulomb pairing of the charge carriers is impossible.

Figure 4 shows T_c as a function of the position of the Fermi level relative to the conduction-band bottom. The maximum critical temperature $T_c^{max} \approx 110$ K corresponds to the Fermi level position shown in Fig. 3. As we can see, T_c increases monotonically as the Fermi level drops (i.e., as the hole density increases). As the Fermi level drops further (when it lies close to SFs), T_c drops sharply on account of the change in the topology and the decrease in the radius of the FS. This agrees qualitatively with the experimental data for T_c in hole-type cuprate MOCs.

Figure 4 also shows the exponent for the isotope effect $\alpha = \frac{1}{2}\partial \ln T_c / \partial \ln \widetilde{\Omega}_{ph}$ as a function of E_F. This dependence demonstrates a tendency for α to decrease as T_c
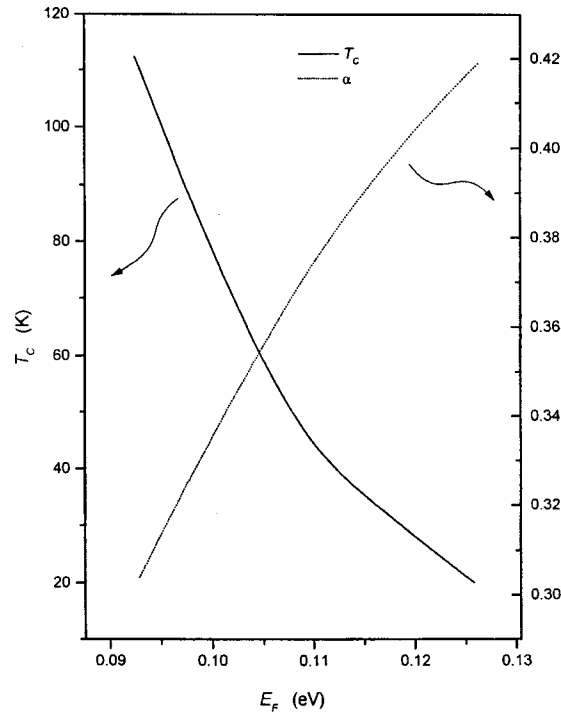
FIG. 4. Critical temperature T_c (solid line) and exponent α of the isotopic shift (dotted line) versus the position of the Fermi level relative to the conduction-band bottom.

increases. This also agrees with existing experimental data[16,17] on the change in T_c when ^{18}O is substituted for ^{16}O.

We can see therefore that the $d_{x^2-y^2}$ symmetry of the superconducting order parameter can be determined to a large degree by the strong suppression of the screened Coulomb repulsion for small momentum transfers as a result of the interaction of electrons with long-wavelength charge-density fluctuations. When this interaction is taken into account together with an anisotropic EPI, the correct density dependences of the critical temperature T_c and exponent α of the isotope effect for high-T_c superconductors are obtained.

We note that a plasmon mechanism due to the Cooper pairing of 2D electrons on account of their interaction with characteristic 2D plasmons having quasiacoustic dispersion was recently proposed in Ref. 18 for the superconductivity observed in Ref. 15. However, such a mechanism is unlikely, since in the limit $q \to 0$ the phase velocity of 2D plasmons is much higher than the electron Fermi velocity, and for $q \gtrsim k_F$ there exists a wide region of strong quantum Landau damping, due to the decay of plasmons into electron–hole pairs, where the electron–electron Coulomb repulsion predominates.

At the same time, as has been shown in Ref. 19, weakly damped 2D surface plasmons with square-root dispersion and relatively low frequency can exist near an interface (heterojunction) between semiconductors with ''light'' electrons and ''heavy'' holes (as, for example, in a GaAs/AlGaAs heterostructure). Interaction with such plasmons (to-

gether with the strong EPI due to the slow SAWs) can give rise to Cooper pairing of degenerate 2D electrons with a sufficiently high DOS (or in a strong QMF, where T_c does not depend on the DOS).

[1] D. S. Dessau, Z.-X. Shen, D. M. King *et al.*, Phys. Rev. Lett. **71**, 2781 (1993).
[2] D. M. King, Z.-X. Shen, D. S. Dessau *et al.*, Phys. Rev. Lett. **73**, 3298 (1994).
[3] K. Gofron, J. C. Campuzano, A. A. Abrikosov *et al.*, Phys. Rev. Lett. **73**, 3302 (1994).
[4] M. C. Schabel, C.-H. Park, A. Matsuura *et al.*, Phys. Rev. B **57**, 6090 (1998).
[5] A. A. Abrikosov, J. C. Campuzano, and K. Gofron, Physica C **214**, 73 (1993).
[6] A. A. Abrikosov, Physica C **214**, 107 (1993); **222**, 191 (1994); **244**, 243 (1995).
[7] D. Pines, Can. J. Phys. **34**, 1379 (1956).
[8] J. Ruvalds, Adv. Phys. **30**, 677 (1981).
[9] P. Monthoux and D. Pines, Phys. Rev. B **47**, 6069 (1993).
[10] G. Varelogiannis, A. Perali, E. Capuletti, and L. Pietronero, Phys. Rev. B **54**, R6877 (1996).
[11] G. M. Éliashberg, Zh. Éksp. Teor. Fiz. **38**, 966 (1960) [Sov. Phys. JETP **11**, 696 (1960)].
[12] A. A. Abrikosov, Phys. Rev. B **57**, 8656 (1998).
[13] R. T. Kao, S. J. Wang, S. P. Chen *et al.*, Phys. Rev. B **58**, 11207 (1998).
[14] T. Moriya, Y. Takahashi, and K. Ueda, J. Phys. Soc. Jpn. **59**, 1905 (1990).
[15] A. Sherman, Phys. Rev. B **55**, 582 (1997).
[16] J. P. Franck, J. Jang, and M. A.-K. Mohamed, Phys. Rev. B **44**, 5318 (1991).
[17] H. J. Bornemann and D. E. Morris, Phys. Rev. B **44**, 5322 (1991).
[18] P. Philips, S. Knysh, and D. Davidovich, Nature (London) **395**, 253 (1998).
[19] É. A. Pashitskiĭ, Zh. Éksp. Teor. Fiz. **56**, 662 (1969) [Sov. Phys. JETP **29**, 362 (1969)].

Translated by M. E. Alferieff

The intra- and intermolecular basis of the zero-shear viscosity in unentangled polymers

N. Fatkullin[*] and R. Kimmich

Universität Ulm, Sektion Kernresonanzspektroskopie, 89069 Ulm, Germany

A general expression for the zero-shear viscosity in unentangled polymers is derived on the basis of chain pair correlations of normal modes and mutual interaction forces. © *1999 American Institute of Physics.*
[S0021-3640(99)00810-5]

PACS numbers: 61.25.Hq, 66.20.+d

It is widely believed that the zero-shear viscosity of concentrated polymer liquids below the critical molecular mass can be treated solely on the basis of intramolecular forces and normal modes. A typical result of this approach is the linear molecular-mass dependence of the viscosity, a finding that is often identified with Rouse chain dynamics.[1] In this letter we show that the neglect of interchain forces and of interchain normal-mode correlations is not compatible with basic physical laws. The fact that the linear molecular-mass dependence of the viscosity apparently predicted by the Rouse model matches the experimental findings may suggest tempting conclusions. However, in the light of the present discussion, the conformity is coincidental and not representative of the real nature of chain dynamics.

The polymer variant of the Green/Kubo linear-response formula for the zero-shear viscosity in liquids reads[2,3]

$$\eta = \frac{V}{k_B T} \int_0^\infty \langle \sigma^{\alpha\beta}(t) \sigma^{\alpha\beta}(0) \rangle \, dt, \tag{1}$$

where V is the sample volume, k_B is Boltzmann's constant, T is the absolute temperature, and $\sigma^{\alpha\beta}(t)$ is an off-diagonal element of the stress tensor, given by

$$\sigma^{\alpha\beta}(t) = -\frac{1}{V} \sum_{i=1}^{N_p} \sum_{n=1}^{N_s} \left[m \, v_{ni}^\alpha(t) v_{ni}^\beta(t) + r_{ni}^\alpha(t) F_{ni}^\beta(t) \right]. \tag{2}$$

The subscript n labels the Kuhn segments within the ith polymer chain, where $n = 1,2,3,\ldots,N_s$ and $i = 1,2,3,\ldots,N_p$. The total number of Kuhn segments per chain is N_s, the total number of polymer chains in the sample is N_p. The quantities $r_{ni}^\alpha(t)$ and $v_{ni}^\alpha(t)$ are the α components of the position and velocity vectors, respectively, of the nth segment in the ith chain at time t. Analogously, $F_{ni}^\beta(t)$ is the β component of the total force vector exerted on the nth segment in the ith chain owing to interactions with all

762

other segments. The velocity-dependent term in Eq. (2) represents the kinetic contribution to the stress. Neglecting this term as usual leads to the well-known Kramers/Kirkwood relation for the stress,

$$\sigma^{\alpha\beta}(t) = -\frac{1}{V} \sum_{i=1}^{N_p} \sum_{n=1}^{N_s} r_{ni}^{\alpha}(t) F_{ni}^{\beta}(t). \tag{3}$$

The total force acting on segment n of chain i may be analyzed into intra- and interchain contributions,

$$\mathbf{F}_{ni}(t) = \mathbf{F}_{ni}^{\text{intra}}(t) + \mathbf{F}_{ni}^{\text{inter}}(t). \tag{4}$$

The intramolecular force mainly arises from entropy elasticity, and can be written in the continuum limit as[1]

$$\mathbf{F}_{ni}^{\text{intra}}(t) = \frac{3k_B T}{b^2} \frac{\partial^2 \mathbf{r}_{ni}(t)}{\partial n^2}, \tag{5}$$

where b is the Kuhn segment length. Newton's second law now tells us that the total force acting on segment n of chain i is related to the segment acceleration according to

$$m\, \mathbf{a}_{ni} \equiv m \frac{d^2}{dt^2} \mathbf{r}_{ni} = \mathbf{F}_{ni}(t). \tag{6}$$

If the many-particle problem of a polymer melt could be solved exactly, the segment accelerations $\mathbf{a}_{ni}$ would be known, and the total force $\mathbf{F}_{ni}(t)$ could be determined via Eq. (6). That is, the stress tensor (3) and the viscosity (1) could then be calculated exactly. In reality, we are restricted to approximations.

We therefore proceed in the following way. The solutions of semiphenomenological equations of motion such as the Rouse equation provide the time dependence of the segment position vector, $\mathbf{r}_{ni}$, so that the accelerations and, hence, the total force vectors (6) can be derived. Using Eqs. (3) and (6), we can rewrite Eq. (1) in the form

$$\eta = \frac{m^2}{k_B T} \frac{1}{V} \sum_{i,n;j,o} \int_0^{\infty} \langle r_{ni}^{\alpha}(t) \ddot{r}_{ni}^{\beta}(t)\, r_{oj}^{\alpha}(0) \ddot{r}_{oj}^{\beta}(0) \rangle \, dt. \tag{7}$$

The position vector of the nth segment is expressed in the usual normal-mode representation,

$$\mathbf{r}_{ni}(t) = \mathbf{X}_{i0}(t) + 2 \sum_{p=1}^{N_s - 1} \mathbf{X}_{ip}(t) \cos\left(\frac{\pi n p}{N_s}\right), \tag{8}$$

where the subscripts indicate the normal mode p of chain i. Substituting Eq. (8) into Eq. (7) and summing up over all segments, i.e., the terms in the sum with the subscripts n and o for the segments of the chains i and j, respectively, gives

$$\eta = \frac{m^2}{k_B T} \frac{1}{V} \sum_{i,j} \int_0^{\infty} \left\langle \left[X_{0i}^{\alpha}(t)\ddot{X}_{0i}^{\beta}(t) + 2N_s \sum_{p=1}^{N_s - 1} X_{pi}^{\alpha}(t)\ddot{X}_{pi}^{\beta}(t) \right] \right.$$

$$\left. \times \left[X_{0j}^{\alpha}(0)\ddot{X}_{0j}^{\beta}(0) + 2N_s \sum_{p'=1}^{N_s - 1} X_{p'j}^{\alpha}(0)\ddot{X}_{p'j}^{\beta}(0) \right] \right\rangle \, dt. \tag{9}$$

Apart from the noncritical approximations mentioned so far, Eq. (9) is an exact result. It obviously correlates normal modes of single chains as well as of pairs of chains i,j. Let us now discuss three levels of treatments of different physical relevance and accuracy.

Treatment 1. Ignoring all intermolecular correlations implied in Eq. (1) and all intermolecular forces in Eq. (4) and considering solely the intrachain force given by Eq. (5) leads to a fictitious result that is usually believed to represent the Rouse version of the shear viscosity,[1]

$$\eta_{\text{intraforce}} = \frac{1}{36} \frac{\zeta}{b} N_s ,$$
(10)

where ζ is the friction coefficient of a Kuhn segment. This is an expression very familiar to polymer scientists. However, there is no physical justification to replace the total force on a segment by just the intramolecular entropy elasticity contribution. The coincidence of the chain length dependence suggested by Eq. (10) with experimental data measured in polymer melts below the critical molecular weight[4] must therefore be considered to be coincidental. The neglect of inertial forces in the Rouse equation of motion does not justify doing so in evaluating the Green/Kubo formula given in Eq. (1). Inertial forces are small relative to the other force terms in that equation, and therefore do not matter very much for the intrachain relaxation modes to be derived in the frame of the Rouse model. However, the Green/Kubo formula given in Eq. (1) is explicitly based on the total force acting on a segment. Seeking an approximate solution of an equation of motion and deriving an expression for the stress tensor are two different things which should not be intermingled. The neglect of the total force in the evaluation of the Green/Kubo formula would simply mean that the viscosity takes the value zero. According to Newton's second law, the total force on a particle is equal to the inertial force. Vanishing total force therefore would mean constant velocity, in contradiction to viscous behavior.

Treatment 2. A somewhat more consistent attempt is to ignore all interchain correlations but to take all forces acting on a segment into account via Newton's second law. With this strategy, Eq. (9) becomes

$$\eta_{\text{intracorr}} = \frac{m^2}{k_B T} \frac{N_p}{V} \int_0^\infty dt \bigg\{ \langle X_0^\alpha(t) X_0^\alpha(0) \rangle \langle \ddot{X}_0^\beta(t) \ddot{X}_0^\beta(0) \rangle$$
$$+ 4 N_s^2 \sum_{p=1}^{N_s-1} \langle X_p^\alpha(t) X_p^\alpha(0) \rangle \langle \ddot{X}_p^\beta(t) \ddot{X}_p^\beta(0) \rangle \bigg\}$$
$$= \frac{1}{9} \frac{m^2 c}{k_B T N_s} \int_0^\infty dt \bigg\{ \langle \mathbf{X}_0(t) \mathbf{X}_0(0) \rangle \langle \ddot{\mathbf{X}}_0(t) \ddot{\mathbf{X}}_0(0) \rangle$$
$$+ 4 N_s^2 \sum_{p=1}^{N_s-1} \langle \mathbf{X}_p(t) \mathbf{X}_p(0) \rangle \langle \ddot{\mathbf{X}}_p(t) \ddot{\mathbf{X}}_p(0) \rangle \bigg\} ,$$
(11)

where the chain number subscripts are now irrelevant, and have therefore been omitted. The quantity $c \equiv N_p N_s / V = \text{const}$ is the Kuhn segment number density. The correlation function terms in Eq. (11) can be evaluated using the stationarity relation

$$\langle \dot{A}(t) B(0) \rangle = -\langle A(t) \dot{B}(0) \rangle .$$
(12)

That is,

$$\langle \ddot{\mathbf{X}}_p(t) \cdot \ddot{\mathbf{X}}_p(0) \rangle = \left\langle \frac{d^4}{dt^4} \mathbf{X}_p(t) \cdot \mathbf{X}_p(0) \right\rangle = \frac{d^4}{dt^4} \langle \mathbf{X}_p(t) \cdot \mathbf{X}_p(0) \rangle. \tag{13}$$

Inserting the well-known Rouse normal-mode solutions[1] gives

$$\langle \ddot{\mathbf{X}}_p(t) \cdot \ddot{\mathbf{X}}_p(0) \rangle = \left(\frac{1}{\tau_p} \right)^4 \langle X_p^2(0) \rangle \exp\left\{ -\frac{t}{\tau_p} \right\}. \tag{14}$$

The relaxation time of the normal mode p is given by $\tau_p = \tau_s N^2/p^2$, where $\tau_s = \zeta b^2/(3\pi^2)k_B T$ is the Rouse relaxation time of a Kuhn segment. Furthermore, $\langle X_p^2(0) \rangle = Nb^2/(2\pi^2 p^2)$.

Inserting Eq. (14) into Eq. (11) now leads to entirely unrealistic results. For example, the first term on the right-hand side of Eq. (11), which is the zeroth mode, refers to the absolute position of the center of mass of a chain. Designating the linear dimension of the sample by L and considering the thermodynamic limit, this suggests that $\eta \propto L^2 \to \infty$. The origin of this singularity is that the treatment is restricted to single-chain mode correlations. It is readily conceivable that the viscous behavior is generally based on motions of molecules relative to each other. That is, intermolecular interactions, and in the case of polymers, intermolecular mode correlations are therefore crucial. The neglect of intermolecular phenomena is not permissible.

It is also of interest to note that a calculation of the contribution of all intrachain modes to the viscosity in analogy with Treatment 1 leads to an expression which is independent of the molecular mass, in contrast to Eq. (10) obtained in Treatment 1. In practice this contribution can be safely neglected, since the effects of intra- and intermolecular forces on the Rouse dynamics tend to compensate each other.

Treatment 3. A correct result for the zero-shear viscosity can only be expected if all interactions and all mode correlations are taken into account. That is, Eq. (9) must be examined in full. This in particular refers to the two-chain mode correlations implied in this equation. As the zero-shear viscosity is determined by motions of the centers of mass of the polymer chains, we consider the center-of-mass contribution to the stress tensor, Eq. (3),

$$\sigma_{\mathrm{cm}}^{\alpha\beta}(t) = -\frac{1}{V} \sum_{i=1}^{N_p} \sum_{n=1}^{N_s} X_{ni}^{\alpha}(t) F_{ni}^{\beta}(t), \tag{15}$$

in terms of the normal-mode representation (8). The total force exerted on chain i by all the other chains is

$$\mathbf{F}_i(t) = \sum_{n,i;o,j} \mathbf{F}_{n,i;o,j}(t) \quad (j \neq i), \tag{16}$$

where $\mathbf{F}_{n,i;o,j}(t)$ is the force exerted by segment o of chain $j \neq i$ on segment n of chain i. Using Newton's third law, $\mathbf{F}_{n,i;o,j}(t) = -\mathbf{F}_{o,j;n,i}(t)$, and summing up over all segments n and o converts Eq. (15) into

$$\sigma_{cm}^{\alpha\beta}(t) = -\frac{1}{2V} \sum_{i \neq j} (X_{0i}^{\alpha}(t) - X_{0j}^{\alpha}(t)) F_{ij}^{\beta}(t), \tag{17}$$

where $F_{ij}^{\beta}(t)$ is the total force exerted on chain j by chain i. Inserting Eq. (17), which was first established in Ref. 5, into Eq. (1) results in the expression for the true zero-shear viscosity of polymers,

$$\eta = \frac{1}{4k_BTV} \sum_{i \neq j} \int_0^{\infty} dt \langle (X_{0i}^{\alpha}(t) - X_{0j}^{\alpha}(t)) F_{ij}^{\beta}(t) (X_{0i}^{\alpha}(0) - X_{0j}^{\alpha}(0)) F_{ij}^{\beta}(0) \rangle. \tag{18}$$

Equation (18) relates the normal modes of order $p = 0$ of two chains i and j and the mutual total forces. It is therefore of an intrinsically intermolecular character. Its further evaluation requires the knowledge of interchain mode correlations and forces for which no theoretical treatment is available so far. However, it is obvious that the singularity that has appeared in Treatment 2 does not occur any more: This expression now depends on the difference of the zeroth order normal modes $X_{0i}^{\alpha}(t) - X_{0j}^{\alpha}(t)$ rather than on the normal modes $X_{0i}^{\alpha}(t)$ themselves in Treatment 2. That is, the absolute position of the center of mass does not enter any more.

Equation (18) tells us that the zero-shear viscosity of concentrated polymer liquids is based on many-chain correlations and interactions even for molecular masses below the critical value, $M < M_c$. This finding is supported by recent computer simulations by Loriot and Weiner,[6–8] which also reveal that the main contribution to stress arises from interchain interactions. We conclude that single-chain formalisms cannot describe viscoelastic phenomena. That is, even for relatively simple systems such as unentangled polymers and contrary to the impression one gets from the literature, we are far from a satisfactory theoretical description of viscous behavior.

*)On leave from Kazan State University, Department of Physics, Kazan 420008, Russia/Tatarstan.

[1] M. Doi and S. F. Edwards, *The Theory of Polymer Dynamics*, Clarendon Press, Oxford, 1986.
[2] P. Résibois and M. De Leener, *Classical Kinetic Theory of Fluids*, Wiley, New York, 1977.
[3] *Progress in Liquid Physics*, Ed. C. A. Croxton, Wiley, New York, 1978.
[4] I. D. Ferry, *Viscoelastic Properties of Polymers*, Wiley, New York, 1980.
[5] M. Fixman, J. Chem. Phys. **42**, 3831 (1965).
[6] G. Loriot and J. H. Weiner, J. Polym. Sci., Part B: Polym. Phys. **36**, 143 (1998).
[7] M. Fixman, J. Chem. Phys. **95**, 1410 (1991).
[8] J. Gao and J. H. Weiner, Science **266**, 748 (1994).

First-sound rarefaction and compression waves in superfluid He-II

V. B. Efimov, G. V. Kolmakov, E. V. Lebedeva, L. P. Mezhov-Deglin, and A. B. Trusov

Institute of Solid-State Physics, Russian Academy of Sciences, 142432 Chernogolovka, Moscow Region, Russia

The evolution of the form of first-sound waves, excited in superfluid He-II by a pulsed heater, with increasing power Q of the perturbing heat pulse is investigated. In liquid compressed to 13.3 atm, a first-sound rarefaction wave (wave of heating) is observed, which transforms into a compression wave and then into a compression shock wave as Q increases, i.e., the change in the conditions of heat transfer at a solid–He-II interface can be judged according to the change in the form of the sound wave. It follows from our measurements that in He-II compression waves are excited at pressures $P \geqslant 1$ atm primarily as a result of the thermal expansion of a normal He-I liquid layer arising at the He-II–heater interface for power Q above a critical level. © *1999 American Institute of Physics.* [S0021-3640(99)00910-X]

PACS numbers: 67.40.Mj

The present letter is devoted to the study of the evolution of the form of first-sound waves excited by a source of short (0.3–10 μs) thermal disturbances in superfluid helium (He-II) at pressures $P \geqslant 1$ atm with increasing power of the heat pulse. It is well known[1–3] that a pulsed heater in He-II excites together with second-sound waves (entropy waves or temperature waves) ordinary first-sound waves (density waves). Since the thermal expansion coefficient of He-II is negative at temperatures above 1.2 K, $\beta = -(1/\rho)(\partial\rho/\partial T)_s < 0$ (here ρ is the density of the liquid), a rarefaction wave ($\delta\rho = \rho\beta\delta T_1 < 0$ for $\delta T_1 > 0$) corresponds to a wave of heating propagating with amplitude $\delta T_1 > 0$ and first-sound velocity away from the heater in He-II. At low heat flux density Q the energy in the first-sound wave is much less than the energy in the second-sound wave. For this reason, the amplitude δT_1 of temperature oscillations in a quasiadiabatic first-sound wave can be much smaller than the amplitude δT_2 of the second-sound wave. In a linear approximation (for small Q), using the relations presented in Refs. 1–3, it can be estimated that at saturated-vapor pressure $P \sim P_{SVP} \leqslant 0.05$ atm and temperature $T = 1.9$ K the amplitude ratio is $\delta T_1/\delta T_2 \simeq 2 \times 10^{-4}$. Therefore a first-sound rarefaction wave with amplitude $\delta T_1 < 0.2$ mK should correspond to a second-sound linear wave with amplitude $\delta T_2 < 1$ mK. As a rule this falls outside the resolution of detectors of short heat pulses (bolometers). The amplitude of linear waves in He-II cannot be increased substantially by increasing the power Q of the perturbing heat pulse, since as Q increases, the second-sound linear wave rapidly transforms into a shock wave, and instead of a wave of heating (rarefaction) the bolometer detects the arrival of a first-sound wave of cooling,

i.e., a compression wave (for $\delta T_1 < 0$, $\delta\rho > 0$). For this reason, most previously published works (see, for example, Refs. 4–6 and the references cited there) have reported the observation of first-sound compression shock waves produced in He-II by powerful short heat pulses.

As will be shown below, by increasing the pressure in He-II to $P = 13.3$ atm we were able to detect simultaneously the propagation of second-sound linear waves and first-sound rarefaction waves for small Q. It was found that as Q increases, a rarefaction wave transforms into a compression (cooling) wave and then into a shock sound wave with a discontinuity (jump of temperature and pressure) at the front of the traveling pulse.

The construction of the experimental apparatus is similar to that described previously in Ref. 7, which is devoted to nonlinear second-sound waves in He-II. The measurements were performed in a 0.3 cm in diameter and 2.9 cm long cylindrical waveguide, filled with a superfluid liquid, in the pressure range 1–13.3 atm at temperatures $T > 1.2$ K. A film heater, connected with a generator of rectangular electric pulses, and a superconducting rhenium bolometer[8] were placed on the waveguide faces. The ac signal from the bolometer was amplified and stored in the memory of a digital oscilloscope. The average power density of the emitted heat pulses in the waveguide can be estimated from the relation $Q = U^2/RS \cong 0.11U^2$ W/cm^2, where U is the voltage on the heater, R is the resistance of the heater, and S is the cross sectional area of the waveguide. The power density Q of the pulsed heat flux in the waveguide was varied from 0.1 to 150 W/cm^2, and the duration τ of the perturbing pulse was varied in steps $\tau = 0.3, 1, 3$, and 10 μs.

Just as in Refs. 4 and 5, only a first-sound compression wave ($\delta T_1 < 0$, $\delta\rho > 0$) could be observed in He-II at low pressures. As an example, Fig. 1 shows oscillograms describing the evolution of the form of a first-sound compression wave in He–II at $T = 2.013$ K and $P = 1.05$ atm with an increase in the power density of a heat pulse with fixed duration $\tau = 0.3$ μs (a) and 10 μs (b). The voltage on the oscillograph screen ($\delta U \sim \delta T_1$) is indicated along the ordinate, i.e., in all plots the signal amplitudes are measured in relative units. A $\delta U \sim 0.001$ V noise level corresponds to $\delta T_1 \sim 5 \times 10^{-6}$ K. The sweep time is measured in μs. The numbers on the plots indicate the electric voltage U on the heater. The repetition frequency of the perturbing pulses is 10 Hz. We note that for small U and perturbing pulse durations $\tau \geq 1$ μs the duration of the detected compression wave is close to that of the perturbing pulse. For $U > 18$ V the bolometer detects the appearance of a shock wave with a discontinuity at the front of the traveling pulse. Similar dependences have been observed in He-II at pressures 2–9 atm.

Figures 1c and 1d show oscillograms describing the evolution of the form of first-sound pulses in He-II at $P = 13.3$ atm and $T = 1.895$ K with heat pulse durations $\tau = 0.3$ μs (c) and 10 μs (d). Increasing the pressure substantially changed not only the form but also the polarity of the detected first-sound waves. For small U the bolometer detects the arrival of a wave of heating (rarefaction wave, $\delta T_1 > 0$, $\delta\rho < 0$), whose width is close to τ for $\tau \geq 1$ μs, while the amplitude increases approximately as U^2. As U increases, the wave of heating transforms into a wave of cooling (compression wave, $\delta T_1 < 0$, $\delta\rho > 0$) and then into a shock compression wave, immediately after which long-period oscillations are observed. Similar oscillations were observed at pressures below and above the critical pressure $P_{cr} = 2.26$ atm, i.e., they can be attributed to transient processes at the heater–He-II interface.
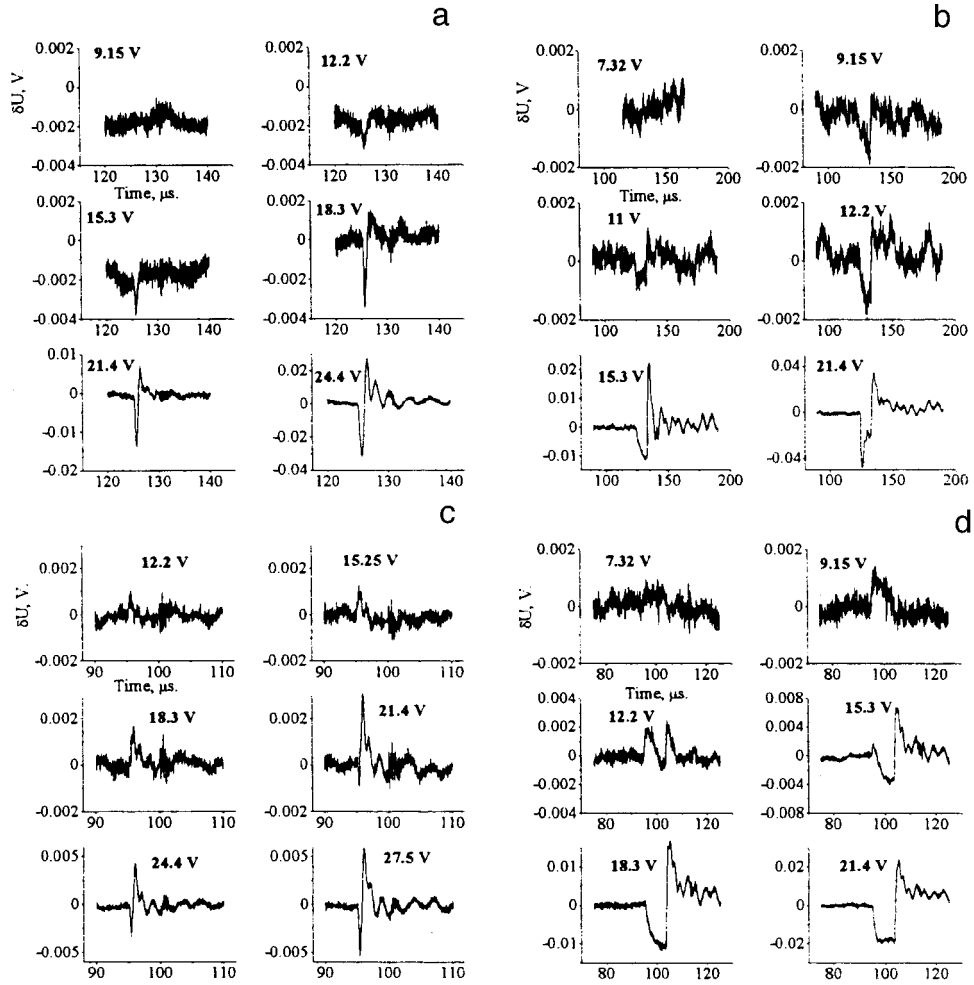
FIG. 1. Evolution of the form of first-sound waves in compressed He-II: $P = 1.05$ atm, $T = 2.031$ K, $\tau = 0.3$ μs (a), $\tau = 10$ μs (b); $P = 13.3$ atm, $T = 1.895$ K, $\tau = 0.3$ μs (c), $\tau = 10$ μs (d). The numbers on the oscillograms indicate the voltage on the heater.

We shall now discuss the results. It is evident from the oscillograms shown in Figs. 1a and 1b that for ~ 0.001 V noise a compression wave with amplitude $A = |\delta U| > 0.001$ V (which corresponds to $|\delta T_1| > 3 \times 10^{-6}$ K) is observed with power above a certain threshold Q_{cr}, whose value decreases with increasing duration of the perturbing pulse. Figure 2 shows $A^{1/2}$ versus the voltage U on the heater. These dependences were calculated from measurements in He-II at $P = 1.05$ atm and $T = 2.013$ K as well as at $T = 2.124$ K. We estimated the values of Q_{cr}, using straight lines to fit the curves $A^{1/2} = f(U)$. It turned out that at constant temperature and pressure in He-II the product $Q_{\mathrm{cr}}\tau^{1/2} \cong$ const with the perturbing pulse duration τ varying by a factor of 30, in agreement with previous observations[4–6] in He-II at saturated-vapor pressure. According to our observations, at pressures $P = 1 - 6$ atm the constant is essentially pressure-independent,
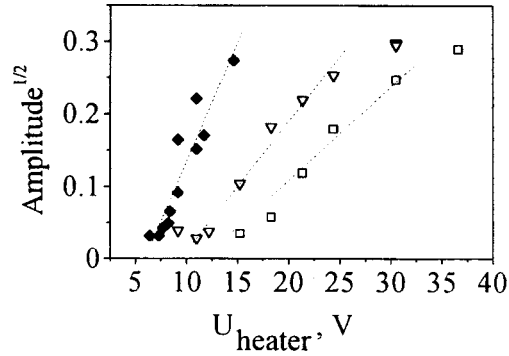
FIG. 2. First-sound amplitude A versus the heater voltage U plotted as $A^{1/2}=f(U)$. $P=1.05$ atm, $T=2.013$ K, $\tau=0.3$ μs — squares, $\tau=10$ μs — triangles, $T=2.124$ K, $\tau=10$ μs — diamonds.

but in contrast to Refs. 4–6 it is strongly temperature-dependent. This indicates that the mechanism leading to the appearance of a compression wave at $P \sim P_{SVP}$ (pulsed boiling up of liquid) is appreciably different from that at high pressures $P \geq 1$ atm. Since compression waves are observed at pressures below and above the critical pressure $P_{cr}=2.26$ atm, where there is no liquid–vapor transition, they can appear primarily only due to the expansion of a normal He-I layer arising at the interface between the heater and He-II for $Q>Q_{cr}$ (in He-I at temperatures $T>T_\lambda+0.006$ K the coefficient $\beta>0$).

The curves $|A|^{1/2}=f(U)$ constructed from measurements at $P=13.3$ atm (Figs. 1c and 1d) are presented in Fig. 3. The filled symbols correspond to a rarefaction wave. As expected, the straight line $|A|^{1/2} \sim U$ drawn through them passes through the origin. The open symbols correspond to a compression wave. The threshold powers Q_{cr}, above which a compression wave is excited, can be estimated from the intersection of the
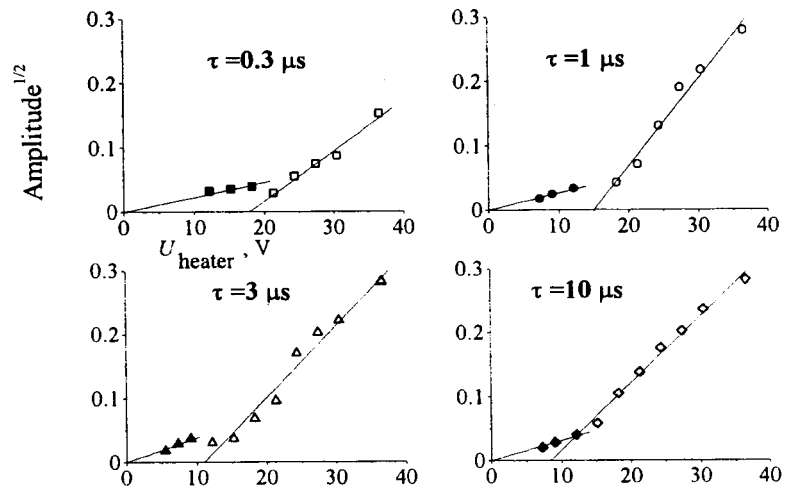
FIG. 3. First-sound amplitude A versus the voltage U on the heater plotted as $A^{1/2}=f(U)$. $P=13.3$ atm, $T=1.895$ K, $\tau=0.3$, 1, 3, and 10 μs; filled symbols — rarefaction waves, open symbols — compression waves.

straight lines drawn through the open symbols with the abscissa. It turned out that, just as at lower pressures, the product $Q_{cr}\tau^{1/2}$ remains essentially unchanged as τ increases from 0.3 to 10 μs.

At the beginning of this letter we noted that in the linear approximation the computed ratio of the amplitudes of temperature oscillations in first- and second-sound waves of heating in He-II at saturated-vapor pressure and temperature $T=1.9$ K is $\delta T_1/\delta T_2 = 2\times 10^{-4}$. Our numerical calculations based on the two-fluid model[1,2] showed that as pressure increases in He-II up to 15 atm the ratio $\delta T_1/\delta T_2$ at $T=1.9$ K must increase by an order of magnitude. To compare the computational predictions with experiment we estimated the ratio of the slopes of the straight lines $A_1^{1/2}=k_1 U$ and $A_2^{1/2}=k_2 U$ drawn through the experimental points describing for small U the dependences of the amplitudes $A_1=f(U)$ and $A_2=f(U)$ of the first- and second-sound waves of heating excited in He-II at $P=13.3$ atm and $T=1.895$ K by heat pulses with durations $\tau=1$, 3, and 10 μs. The ratio of the coefficients lies in the range $k_2/k_1\approx 23\pm 6$, i.e., the results of the measurements agree with the theoretical calculation $k_2/k_1=(\delta T_2/\delta T_1)^{1/2}\approx 23$.

In summary, our investigations have shown that increasing pressure in He-II to 13 atm increases by an order of magnitude the ratio of the amplitudes of temperature oscillations in first- and second-sound waves of heating generated by a pulsed heater in a superfluid liquid at low Q.

For power above a critical level Q_{cr}, which is essentially pressure-independent for $P>1$ atm but increases away from T_λ or with decreasing duration of the perturbing pulse (as $\tau^{-1/2}$), the mechanism of heat transfer at the heater–He-II interface changes qualitatively, which is manifested as excitation of first-sound compression (cooling) waves. The observations of compression waves at pressures below and above P_{cr} indicate that these waves appear mainly as a result of the thermal expansion of a normal He-I liquid layer arising near the surface of the heater with large heat loads. At low pressures $P\approx P_{SVP}$ the film boiling up of liquid, previously thought to be the main mechanism leading to the excitation of first-sound shock waves with pulsed heating of He-II, must also be taken into account.

[1] L. D. Landau and E. M. Lifshitz, *Fluid Mechanics*, 2nd ed. (Pergamon Press, Oxford, 1987) [Russian original, 3rd ed., Nauka, Moscow, 1986].

[2] I. M. Khalatnikov, *Introduction to the Theory of Superfluidity* (Addison-Wesley, New York, 1989) [Russian original, Nauka, Moscow, 1965].

[3] S. Putterman, *Hydrodynamics of Superfluids* (North-Holland, Amsterdam, 1974) [Russian translation, Mir, Moscow, 1978].

[4] A. Yu. Iznankin and L. P. Mezhov-Deglin, Zh. Éksp. Teor. Fiz. **84**, 1378 (1983) [Sov. Phys. JETP **57**, 801 (1983)].

[5] M. Pomerantz, Phys. Rev. Lett. **26**, 362 (1971).

[6] E. V. Ametistov and V. A. Grigor'ev, *Heat Transfer in He-II* [in Russian] (Énergoatomizdat, Moscow, 1986).

[7] V. B. Efimov, L. P. Mezhov-Deglin, A. B. Trusov, and G. V. Kolmakov, Fiz. Nizk. Temp. **25**, 551 (1999) [Low Temp. Phys. **25**, 407 (1999)].

[8] I. Yu. Borisenko, L. P. Mezhov-Deglin, and V. Zh. Rozenflants, Prib. Tekh. Éksp., No. 5, 137 (1987).

Translated by M. E. Alferieff

Instability of the non-Fermi-liquid state in a metal with *d* or *f* impurities

L. A. Manakova

Kurchatov Institute Russian Science Center, 123182 Moscow, Russia

It is shown that the non-Fermi-liquid state is unstable with respect to scattering of multiparticle excitations with different quantum numbers by one another. As a result of the scattering, a multiparticle Fermi-liquid resonance forms at the Fermi level. An anomalous increase in the conductivity occurs as a result of a transition between the non-Fermi-liquid and Fermi-liquid states. © *1999 American Institute of Physics.* [S0021-3640(99)01010-5]

PACS numbers: 71.10.Hf, 71.10.Ay

1. The most popular systems showing non-Fermi-liquid behavior at present are generalized variants of Anderson's impurity model and multichannel, both spin and orbital (quadrupole), Kondo models (see, for example, the review in Ref. 1). As is well known,[2,3] the non-Fermi-liquid (NFL) state is unstable with respect to any excitations that lift the degeneracy with respect to the orbital or spin degrees of freedom. Specifically, in the two-channel quadrupole Kondo model two instability mechanisms were known previously. The first one is an instability with respect to distortions of an impurity center that lower the symmetry of the center (Jahn–Teller or pseudo Jahn–Teller effect)[2] and lift the orbital degeneracy of the impurity level. The second mechanism described[3] the instability of the NFL state with respect to the anisotropy of the scattering channels. The anisotropy of the channels arises in an external magnetic field and the corresponding crossover from the NFL to the FL state has been observed in Ref. 4. A new physical realization of the two-channel quadrupole Kondo model and instability of the NFL state with respect to tunneling-induced interband scattering were described in Ref. 5 for doped quantum-size structures.

In the present letter it is shown that in metals containing an impurity with unfilled *d* or *f* shells there occurs an *instability of the NFL state with respect to the rescattering by one another of multiparticle excitations having different z* projections of the quadrupole moment. A transition between the NFL and FL states occurs as the impurity level becomes deeper.

2. Physical realizations of the two-channel quadrupole Kondo model have been proposed in Ref. 2 for U-based heavy-fermion compounds and for high-T_c superconductors. Keeping this in mind, in the present letter a nonmagnetic quadrupole doublet of the crystal field of $3d$ or Γ_3 symmetry is considered as the deep impurity state. The taking into account of the splitting of the *f* or *d* levels by the crystal field signifies a transition

from the angular momentum representation to the irreducible representations of the point group of the crystal. As is well known, a cubic crystal field splits the $3d$ states of transition-metal ions into a doubly degenerate e_g level and a triply degenerate t_{2g} level. The eigenfunctions and quantum numbers of an electron in an e_g level are, correspondingly, the cubic de_g functions and the row number of the irreducible representation of the μ_{e_g} group is ± 1. It is convenient to describe an e_g doublet with one electron (or hole) by the pseudospin variable $\hat{\tau}_d$, whose projections on the coordinate axes are also the components of the quadrupole moment tensor. The two values of the quantum number $\mu = \pm 1$ correspond to the projections of the quadrupole moment on the z axis: $\hat{\tau}_d^z = (1/12)[3L_z^2 - L(L+1)] = \pm 1/2$ corresponding to occupied d_{z^2} orbitals ($L_z = 0$) and $d_{x^2-y^2}$ orbitals ($|L_z| = 2$), where $\hat{L}$ is the angular momentum operator. The operator $\hat{\tau}_d^x \sim L_x^2 - L_y^2$ rotates the pseudospin. In U-based compounds the ground state of the U^{4+} ion is a $5f^2$ Γ_3 doublet obtained as a result of splitting of a multiplet with total angular momentum $J = 4$ by a cubic crystal field. The Γ_3 doublet possesses a quadrupole moment and has no magnetic dipole moment. The parametrization of the Γ_3 doublet by pseudospin 1/2 is similar to the parametrization for the e_g doublet above, the difference being that the projections of the quadrupole moment can be expressed in terms of the eigenvalues of the operators $\hat{J}^2$ and $\hat{J}_z$. The collection of quantum numbers in a crystal field is denoted below as (Λ, μ), $\Lambda \equiv e_g$, Γ_3. The initial Hamiltonian of the system has the standard form for the generalized Anderson model

$$H = H_{00} + H_h + H_U \quad \text{and} \quad H_{00} = \sum_{\mathbf{kk'}\sigma} \varepsilon_{\mathbf{k}} a_{\mathbf{k}\sigma}^+ a_{\mathbf{k}\sigma} + \sum_{\mu\sigma} \varepsilon_{\Lambda} d_{\Lambda\mu\sigma}^+ d_{\Lambda\mu\sigma},$$

where H_h and H_U are the hybridization and Coulomb repulsion on a deep level and are given by

$$H_h = \sum_{\mathbf{k}\sigma\mu} (T_{\mathbf{k}\mu}^{\Lambda} a_{\mathbf{k}\sigma}^+ d_{\Lambda\sigma\mu} + \text{h.c.}) \quad \text{and} \quad H_U = \sum_{\mu,\mu';\sigma,\sigma'} U_{\mu\mu'} n_{\Lambda\mu\sigma} n_{\Lambda\mu'\sigma'} (1 - \delta_{\mu\mu'}\delta_{\sigma\sigma'}),$$

$$(1)$$

the operators $d_{\Lambda\mu\sigma}^+$ and $d_{\Lambda\mu\sigma}$ describe the quasilocal electronic states of the Λ doublet with z projection of the pseudospin μ and spin σ (spin for the e_g doublet). For a deep impurity level ($\gamma_\Lambda/\varepsilon_\Lambda \ll 1$, $\gamma_\Lambda \sim |T_{k_F\mu}^{\Lambda}|^2 \rho_0$, and ρ_0 is the density of itinerant states) the effective interaction between itinerant electrons and an electron in a deep level is obtained after applying a Schrieffer–Wolf transformation to the Hamiltonian H. The interaction, which is an exchange interaction with respect to the quadrupole moment of the impurity and a ''non-Kondo'' interaction with respect to the spin variables, is studied below. The physical conditions under which this is the predominant interaction have been examined in detail in the second of Refs. 5.

It should also be noted that the states of the Γ_3 doublet hybridize with the band states with Γ_8 symmetry (the partial components are $|\Gamma_8, 2\rangle$ and $|\Gamma_8, 1\rangle$) and $\bar{\Gamma}_8$ (the partial components are $|\Gamma_8, -2\rangle$ and $|\Gamma_8, -1\rangle$). Scattering processes occur only between two partial states within each group.[2] Correspondingly, the complete Hamiltonian is a sum of two terms with $\sigma = 1.2 \equiv \Gamma_8$, $\bar{\Gamma}_8$, corresponding to exchange scattering within each group. On this basis the transformed Hamiltonian has the form $\bar{H} = H_{00} + H_{\text{sc}} + H_{\text{int}}$, where

$$H_{\rm sc} = \sum_{{\bf kk'}\nu\sigma} (T^{\Lambda\nu}_{\bf kk'} a^+_{{\bf k}\nu\sigma} a_{{\bf k'}\nu\sigma} + {\rm h.c.}) \quad {\rm and} \quad H_{\rm int} = \sum_{{\bf kk'}\mu\mu'\nu\sigma} V^{\Lambda\nu}_{\mu\mu'}({\bf kk'}) a^+_{{\bf k}\nu\sigma} a_{{\bf k'}\nu\sigma} d^+_{\Lambda\mu} d_{\Lambda\mu'} .$$

(2)

Here ν enumerates the bands with which the Λ doublet can hybridize.

The Hubbard repulsion $U_{\mu\mu'}$ at a site is the largest parameter in the problem. Therefore the matrix elements satisfy the standard relations:

$$V^{\Lambda\nu}_{\mu\mu'}({\bf kk'}) \sim -\frac{T^{\Lambda\nu*}_{{\bf k}\mu} T^{\Lambda\nu}_{{\bf k'}\mu'}}{E_\Lambda - \varepsilon_F}, \quad T^{\Lambda\nu}_{\bf kk'} \sim \sum_{\mu\mu'} V^{\Lambda\nu}_{\mu\mu'}({\bf kk'}), \quad \varepsilon_F - E_\Lambda \equiv \varepsilon_\Lambda .$$

If the symmetry of the band states is such that the hybridization matrix elements $T^{\Lambda\nu}_{{\bf k}\mu}$ have nonzero values for both components of the Λ doublet, then they are at the same time spatially nonlocal. On account of this, in Eq. (2) the matrix elements of the interaction are spatially nonlocal and possess nonzero values with $\mu \neq \mu'$. These two conditions are sufficient for the Hamiltonian $H_{\rm int}$ in Eq. (2) to be reducible to the Hamiltonian of the two-channel quadrupole Kondo model. For this we expand the operators $a_{{\bf k}\nu\sigma}$ and matrix elements $T^{\Lambda\nu}_{\bf kk'}$ and $V^{\Lambda\nu}_{\mu\mu'}({\bf kk'})$ in terms of the cubic harmonics $K_{\Lambda\beta}(\Omega_{\bf k})$, $\beta = \pm 1$. It is assumed that the conduction electrons can also be described by pseudospin 1/2. Using the partial components $a_{k\beta\nu\sigma}$ the Hamiltonian $\bar{H}$ can be written as

$$\tilde{H} = H_{00} + \sum_{kk'\sigma} \sum_{\beta\beta'\nu} T^{\Lambda\nu}_{\beta\beta'}(kk') a^+_{k\beta\nu\sigma} a_{k'\beta'\nu\sigma}$$

$$+ \sum_{kk'\sigma} \sum_{i=x,y,z} \sum_{\beta,\beta'\nu} V^{\Lambda\nu}_{i\beta\beta'}(kk') a^+_{k\beta\nu\sigma} a_{k'\beta'\nu\sigma} \hat{\tau}^i_\Lambda ,$$

(3)

where the interaction matrix elements and the pseudospin operator are as follows ($\hat{\sigma}^i$ are Pauli matrices):

$$V^{\Lambda\nu}_{\mu\mu'}({\bf kk'}) = \sum_{i=x,y,z} V^{\Lambda\nu}_{\bf kk'} (\hat{\tau}^i_\Lambda)_{\mu\mu'}, \quad \hat{\tau}^i_\Lambda = \sum_{\mu\mu'=\pm 1} d^+_{\Lambda\mu} \sigma^i_{\mu\mu'} d_{\Lambda\mu'},$$

$${\rm and} \sum_{\mu=\pm 1} d^+_{\Lambda\mu} d_{\Lambda\mu} = 1.$$

In the system described by the Hamiltonian $\tilde{H}$ in Eq. (3) there are two physical mechanisms which give rise to resonant states near the Fermi level. The interaction $H_{\rm int}$ is responsible for the formation of multiparticle NFL resonances at the Fermi level. The term $H_{\rm sc}$ describes scattering of multiparticle excitations with quantum numbers $\beta \neq \beta'$ by one another. *This scattering can lead to the formation of an additional and only a Fermi-liquid resonance at the Fermi level.*

According to the formalism developed in Ref. 5, it is convenient to diagonalize the Hamiltonian in Eq. (3) in two steps. At the first step we diagonalize the Hamiltonian $H_0 = H_{00} + H_{\rm int}$ and obtain multiparticle excitations at the Fermi level. Next we take into account the scattering induced between multiparticle excitations by the term $H_{\rm sc}$.

3. In the present letter we shall be interested in the main effect of the interaction — the existence of a multiparticle resonance at the Fermi level. The Green's function G_Λ

corresponding to this resonance can be calculated by the bosonization method, which was introduced in Ref. 6 for an interaction of the type (3). The crux of the method consists in expressing the operators $a_{k\beta\nu\sigma} = \int_{-\infty}^{+\infty} e^{-ikx} \psi_{\beta\sigma}^{(\nu)}(x)$ in terms of collective variables, which are described by the Fourier components of the Bose fields corresponding to charge (c), spin or (equivalently) color (f), pseudospin (s), and mixed (pseudospin–color = spin–quadrupole, sf) density operators. The Hamiltonian $H_0 = H_{00} + H_{int}$ can be represented in terms of these variables as a sum of four terms corresponding to four spinless collective fermion channels. The charge and spin (color) channels are not related with the impurity pseudospin. In the two other channels the interactions in Eq. (3) have the form

$$H_{int} = \sum_{\nu} \frac{V_x^{\Lambda\nu}}{(2a\pi)^{1/2}} [\psi_{sf}^{(\nu)+}(0) + \psi_{sf}^{(\nu)}(0)] \hat{\tau}_\Lambda^x + \tilde{V}_z^{\Lambda\nu} \psi_s^{(\nu)+}(0) \psi_s^{(\nu)}(0) \hat{\tau}_\Lambda^z . \qquad (4)$$

Here a is the lattice constant, $\psi_{s,sf}^{(\nu)}(0) \equiv \psi_{s,sf}^{(\nu)}(x=0)$, x is the spatial coordinate, and $\tilde{V}_z^{\Lambda\nu} = 2(V_z^{\Lambda\nu} - \pi v_F)$. The representation $V_{i\beta\beta'}^{\Lambda\nu}(kk') = V_i^{\Lambda\nu}(\hat{\sigma}^i)_{\beta\beta'}$ was used for the matrix elements of the interaction in Eq. (3).

The resonance level is described by fermion operators d^+ and d, which are related with the pseudospin operator by means of the Majorana representation:[6] $d^+ = \hat{\tau}_\Lambda^+ \hat{\eta}$, $\tau_\Lambda^z = d^+ d - 1/2$, and $\hat{\eta}$ is a Majorana (real) fermion operator, where $\hat{\eta}^2 = 1$. The Green's function of the resonant level possesses both normal ($\sim \langle dd^+ \rangle$) and anomalous ($\sim \langle dd \rangle$, $\sim \langle d^+ d^+ \rangle$) components, since the number of fermions in Eq. (4) is not conserved. The Hamiltonian H_0 with finite interaction constants $\tilde{V}_z^{\Lambda\nu}$ can be diagonalized because the "hybridization" and the interaction in Eq. (4) are "distributed" in different channels. A method for calculating the Green's function of the resonant level with finite interaction constants $\tilde{V}_z^{\Lambda\nu}$ has been proposed in Ref. 5. Using the results of Ref. 5 we obtain

$$\hat{G}_\Lambda^{(\pm)}(z) = A_\pm \Gamma(1-\alpha_s) \tilde{\rho}_0 \left[(\hat{\sigma}_0 - \hat{\sigma}_x) \left(\frac{W}{z + i\Gamma_K^\Lambda} \right)^{1-\alpha_s} + (\hat{\sigma}_0 + \hat{\sigma}_x) \left(\frac{W}{z} \right)^{1-\alpha_s} \right], \qquad (5)$$

$A_\pm$ are phase factors for $\mathrm{Re}\, z \gtrless 0$, $\Gamma(x)$ is the gamma function, $\alpha_s = \sum_\nu \alpha_{s\nu}$, $\alpha_{s\nu} = (\delta_{s\nu}/\pi)^2$, $\delta_{s\nu}$ are phase shifts characterizing the scattering in pseudospin channels, $\tilde{\rho}_0 = \rho_0 (\rho_{01}/\rho_0)^{\alpha_{s1}} (\rho_{02}/\rho_0)^{\alpha_{s2}}$, $\rho_0 \sim 1/W$, $\rho_{0\nu} \sim 1/W_\nu$, $W = \sum_\nu W_\nu$, W_ν are of the order of the band widths, $\Gamma_K^\Lambda \equiv \sum_\nu \Gamma_{K\nu}^\Lambda$, $\Gamma_{K\nu}^\Lambda \sim (V_x^{\Lambda\nu})^2/W_\nu$ (the Fermi level is taken as the reference zero point everywhere), and $\mathrm{Im}\, z < 0$, since we are calculating the retarded Green's function. The NFL resonance of width Γ_K^Λ at the Fermi level is formed by a mixed spin-quadrupole mode, which is charged on account of the quadrupole contribution. The interactions in the pseudospin channels are of a screening character and produce an effective broadening of the NFL resonance. It follows from Eq. (5) that the interference of the resonances from different electron groups also leads to an effective broadening of the total resonance as compared with the single-resonance case.

The Green's functions of the conduction electrons can be obtained by the equations-of-motion method.[7] Their components which are diagonal with respect to the index ν have the form

$$G_{0\mu}^\nu(\mathbf{k}\mathbf{k}'; z) = \delta_{\mathbf{k}\mathbf{k}'} G_{00\mu}^\nu(\mathbf{k}; z) + G_{00\mu}^\nu(\mathbf{k}; z) T_{\mathbf{k}\mu}^{\Lambda\nu*} G_{\Lambda\mu\mu}(z) T_{\mathbf{k}'\mu}^{\Lambda\nu} G_{00\mu}^\nu(\mathbf{k}'; z), \qquad (6)$$

where $G^{\nu}_{00\mu}(\mathbf{k};z)$ is the Green's function of the noninteracting electrons and $G_{\Lambda\mu\mu}(z)$ is the Green's function of the impurity level with the interaction taken into account. To obtain the density of states at the Fermi level, we substitute into Eq. (6) the Green's function of the resonance level $G_\Lambda(z)$ from Eq. (5) and write the Green's function (6) using the partial states $a_{k\nu\beta\sigma}$. Then we obtain

$$\rho_{\Lambda\nu}(\varepsilon)-\rho_{0\nu}(\varepsilon)=-\frac{1}{\pi}A_\rho \operatorname{Im} Sp\hat{G}^{(+)}_\Lambda(\varepsilon)=A_\rho \sum_{i=1,2}\frac{\sin[(1-\alpha_s)\arctan\Gamma_i/\varepsilon]}{W^{\alpha_s}(\varepsilon^2+\Gamma_i^2)^{(1-\alpha_s)/2}}, \quad \varepsilon>0, \tag{7}$$

$A_\rho \sim \gamma_{\Lambda\nu}\rho_{0\nu}$, $\gamma_{\Lambda\nu}=\Sigma_\beta \gamma_{\Lambda\nu\beta}\equiv\Sigma_\beta|T^{\Lambda\nu}_{k_F\beta}|^2\rho_{0\nu}$, and the widths $\Gamma_1=\delta\to0$ and $\Gamma_2=\Gamma^\Lambda_K$ correspond to two terms in the Green's function $\hat{G}^{(+)}_\Lambda$.

4. The scattering induced between multiparticle excitations having different z projections of the quadrupole moment ($\beta\neq\beta'$) by the term H_{sc} in Eqs. (2) and (3) gives rise in the complete Green's functions to a pole corresponding to a Fermi-liquid resonance at the Fermi level. With the scattering taken into account, the Green's function has the form

$$G^\nu_\beta(kk';z)=\delta_{kk'}G^\nu_{0\beta}(k;z)+G^\nu_{0\beta}(k;z)\frac{T^{\Lambda\nu}_{k\beta}T^{\Lambda\nu*}_{k'\beta}\Sigma^{\Lambda\nu}_{\beta'}(z)}{\varepsilon^2_\Lambda D(z)}G^\nu_{0\beta}(\mathbf{k}';z), \quad \beta\neq\beta', \tag{8}$$

(in Eq. (8) all quantities are summed over μ), $G^\nu_{0\beta}(k;z)$ are the Green's functions determined for the spectrum with the density of states $\rho_{\Lambda\nu}(\varepsilon)$,

$$\Sigma^{\Lambda\nu}_\beta(z)=\sum_k\frac{|T^{\Lambda\nu}_{k\beta}|^2 f(\varepsilon_{k\nu})}{z-\varepsilon_{k\nu}}, \quad D(z)=1-\frac{\Sigma^{\Lambda\nu}_\beta(z)\Sigma^{\Lambda\nu}_{\beta'}(z)}{\varepsilon^2_\Lambda}, \quad \beta\neq\beta', \tag{9}$$

and $f(\varepsilon)$ is the Fermi function. The self-energy functions $\Sigma^{\Lambda\nu}_\beta(z)$ have singularities at the Fermi level which correspond to multiparticle peaks in the density of states. For simplicity, the term quadratic in the self-energy functions is retained in $D(z)$, since this term contains the maximum singularity at the Fermi level. This term is present only for $\beta\neq\beta'$. At zero temperature the contribution of the resonance levels to the self-energy functions $\Sigma^{\Lambda\nu}_\beta(z)$ is determined by the expressions

$$\Sigma^{\Lambda\nu}_\beta(z)=|T^{\Lambda\nu}_{k_F\beta}|^2\int_{-\infty}^0 d\varepsilon\frac{\rho_{\Lambda\nu}(\varepsilon)}{z-\varepsilon}\approx A_\nu\gamma_{\Lambda\nu}\gamma_{\Lambda\nu\beta}\tilde{\rho}_0\left(\frac{W}{z+i\Gamma^\Lambda_K}\right)^{1-\alpha_s}(-1)^{\alpha_s-1}, \tag{10}$$

$A_\nu\sim1$. For $\alpha_s=0$ an additional term, which is singular for $|z|\ll\Gamma^\Lambda_K$, appears in $\Sigma^{\Lambda\nu}_\beta(z)$. It corresponds to a δ-like contribution to the spectral function of the impurity degrees of freedom, which are not related with the conduction electrons (see the second term in $G^{(\pm)}_\Lambda$ in Eq. (5) with $\alpha_s=0$, $z=\varepsilon+i\delta$), and it has the form

$$\Sigma^\nu_\beta(z)\sim 1/z, \quad |z|\ll\Gamma^\Lambda_K. \tag{11}$$

The poles of the Green's functions in Eq. (8) and, correspondingly, the new Fermi-liquid resonances with energy $z_r=\varepsilon_r+i\gamma_r$ at the Fermi level are determined by the solutions of the equation $D(z_r)=0$.

Using expressions (10) is it easy to show that for all $\alpha_s\leq1/3$, including $\alpha_s=0$, there exist FL resonances with widths $|\gamma_r-\Gamma^\Lambda_K|\ll\Gamma^\Lambda_K$, which for $\gamma_r\gg|\varepsilon_r|$ are determined by the expression

$$\frac{|\gamma_r - \Gamma_K^\Lambda|}{W} = A_r \left(\frac{\gamma_{\Lambda\nu}^2 \tilde{\rho}_0}{\varepsilon_\Lambda} \right)^{1/(1-\alpha_s)} \left(\frac{\gamma_{\Lambda\nu\beta}\gamma_{\Lambda\nu\beta'}}{\gamma_{\Lambda\nu}^2} \right)^{1/2(1-\alpha_s)}, \tag{12}$$

$A_r \sim 1$. This expression determines two resonances with close widths: $\gamma_r^\pm \equiv \Gamma_K^\Lambda \pm \delta\gamma$, $\delta\gamma \ll \Gamma_K^\Lambda$. For $\alpha_s = 1/3$ both resonances lie at the Fermi level, forming a total resonance with a weakly non-Lorentzian shape. For $\alpha_s < 1/3$ the resonances are ''separated'' by an amount $2\varepsilon_r$ symmetrically with respect to the Fermi level. The maximum splitting with $\varepsilon_r = \delta\gamma$ occurs for $\alpha_s = 0$. The width of the NFL resonance at the Fermi level, i.e., the characteristic binding energy of the collective states comprising it, decreases as the impurity level becomes deeper. Correspondingly, the FL resonances, whose existence requires decay of the NFL collective states, can exist for a sufficiently deep impurity level. Specifically, for equivalent parameters for both groups of electrons the position of the level should satisfy

$$\varepsilon_\Lambda / W \gg (\gamma_\Lambda / W)^{2\alpha_s}, \tag{13}$$

and as α_s decreases, the FL resonance exists for increasingly deeper levels.

Using Eq. (11) we obtain that on account of scattering due to H_{sc} the impurity degrees of freedom which are not related with the conduction electrons engender a localized state with energy $\varepsilon_b = \delta\gamma$ above the Fermi level.

We see that scattering of multiparticle excitations having different z projections of the quadrupole moment by one another *leads to a transition between NFL and Fermi-liquid states as the impurity level becomes deeper*. The former corresponds to a power-law singularity in $G_{0\mu}^\nu(\mathbf{kk'}; z)$ in Eq. (6) and the latter corresponds to a simple pole in $G_\beta^\nu(kk'; z)$ from Eq. (8).

5. The transition rate for scattering from $|\mathbf{k}\nu\rangle$ into $|\mathbf{k'}\nu\rangle$ is determined by the expression

$$W(\mathbf{k}, \varepsilon_{\mathbf{k}\nu}; \mathbf{k'}, \varepsilon_{\mathbf{k'}\nu}) = 2\pi |\mathcal{T}(\mathbf{k}, \varepsilon_{\mathbf{k}\nu}; \mathbf{k'}, \varepsilon_{\mathbf{k'}\nu})|^2 \delta(\varepsilon_{\mathbf{k}\nu} - \varepsilon_{\mathbf{k'}\nu})$$

with the scattering amplitude

$$\mathcal{T}(\mathbf{k}, \varepsilon_{\mathbf{k}\nu}; \mathbf{k'}, \varepsilon_{\mathbf{k'}\nu}) = \sum_{\mathbf{pp'}\sigma} \langle a_{\mathbf{k}\nu\sigma} | H_{sc} | a_{\mathbf{p}\nu\sigma} \rangle \langle a_{\mathbf{p}\nu\sigma} | G | a_{\mathbf{p'}\nu\sigma} \rangle \langle a_{\mathbf{p'}\sigma\nu} | H_{sc} | a_{\mathbf{k'}\nu\sigma} \rangle, \tag{14}$$

where $G_{\mathbf{pp'}}^\nu$ is the Green's function determined in Eq. (8). Using a Landauer-type formula for the conductivity and comparing the resonant and non-Fermi-liquid contributions to the transition rate, it is easy to obtain the following relation for the maximum values of the conductivities:

$$\sigma_r^{max}(0) \gg \sigma_{NFL}^{max}(0) \tag{15}$$

for all values of the parameters for which an FL resonance exists. This relation means that *a transition between the NFL and FL states is accompanied by an anomalous increase in the conductivity.*

The term H_{sc} with potential scattering is obtained, simultaneously with the effective interaction, as a result of a Schrieffer–Wolf transformation. In this sense the instability considered above is ''primary'' as compared with the previously known instabilities.[2,3] For fixed α_s the existence of this instability depends only on the depth of the level. This

is also true when the scale of the $h\tau_\Lambda^z$-type tetragonal distortions of the impurity site is less than the characteristic energy γ_Λ associated with scattering. The *key condition* for the existence of an instability is spatial nonlocality of the hybridization matrix elements.

A direct experimental method making it possible to observe instability is tunneling spectroscopy, specifically, the determination of the current–voltage characteristic in the presence of tunneling through a barrier containing orbitally degenerate local states.

[1] P. Schlottmann and P. D. Sacramento, Physica B **206–207**, 95 (1995).
[2] D. J. Cox *et al.*, Phys. Rev. Lett. **59**, 1240 (1987); **62**, 2188 (1989).
[3] M. Fabrizio, A. O. Gogolin, and Ph. Nozieres, Phys. Rev. Lett. **74**, 4503 (1995).
[4] D. C. Ralph and B. A. Buhrman, Phys. Rev. Lett. **72**, 3401 (1994).
[5] L. A. Manakova, JETP Lett. **67**, 1069 (1998); Zh. Éksp. Teor. Fiz. **114**, 1466 (1998) [JETP **87**, 796 (1998)].
[6] V. J. Emery and S. Kivelson, Phys. Rev. B **46**, 10812 (1992).
[7] A. C. Hewson, *The Kondo Problem to Heavy Fermions* (Cambridge University Press, New York, 1993).

Translated by M. E. Alferieff

Above-barrier excitons: first magnetooptic investigation

M. R. Vladimirova, A. V. Kavokin, M. A. Kaliteevskiĭ, S. I. Kokhanovskiĭ, M. E. Sasin, and R. P. Seĭsyan*⁾

A. F. Ioffe Physicotechnical Institute, Russian Academy of Sciences, 194021 St. Petersburg, Russia

An above-barrier localized excitonic state in a Bragg confining semiconductor superstructure based on an (In, Ga)As/GaAs heterosystem is observed experimentally. A sharp excitonic resonance corresponding to the interference mechanism of localization is observed in the absorption spectrum of this structure at 1.548 eV, i.e., 33 meV above the energy of a bulk exciton in GaAs. The oscillator strength of the above-barrier exciton is twice that of the main excitonic state in the system, and the above-barrier exciton gives rise to sharp Landau oscillations in the magnetoabsorption spectra. © *1999 American Institute of Physics.* [S0021-3640(99)01110-X]

PACS numbers: 71.35.Cc, 78.20.Ls, 73.40.Kp

1. LOCALIZATION IN A REPULSIVE POTENTIAL

More than 60 years ago Wigner and von Neumann[1] predicted theoretically that an electron can be spatially localized not only by an attractive but also by a repulsive potential if this potential has a special form. Localization for positive energies arises because of repeated above-barrier reflection of the electronic wave function on the bends of the potential. In 1975 Stillinger[2] proposed semiconductor superstructures (complex multilayer heterostructures) as an object where Wigner–von Neumann localization is possible. Superlattices with built-in thick layers and ideally smooth interfaces were required to observe such localized states experimentally.

In the last five years a series of observations of above-barrier localized electrons and excitons in superlattices with thick layers have been reported.[3-8] The nature of these states can be easily understood by drawing an analogy between a superlattice and an ordinary crystal lattice. A superlattice, as a quasicrystal, possesses its own band structure, different from that of its constituent semiconductor crystals. The band structure of a superlattice is characterized by alternation of one-dimensional allowed and forbidden minibands, possessing energies both above and below the barrier. A thick layer in a superlattice is the analog of an impurity center in a crystal lattice. Discrete levels associated with these ''impurities,'' including in the presence of above-barrier energies, arise in the forbidden minibands. Bragg-ordered superlattices, where the layer thicknesses equal one-fourth the de Broglie wavelength of an electron with energy corresponding to the above-barrier state, are optimal from the standpoint of spatial localization of above-barrier electrons. The thickness of the thick barrier equals half the de Broglie wavelength.

The penetration depth of the electron wave function into the region of the superlattice ''mirrors'' can be easily calculated by the transfer matrix method. It is given by

$$L = d \ln^{-1}\left[\frac{m_B E}{m_A (E-V)}\right], \qquad (1)$$

where d is the superlattice period, E is the electron energy measured from the conduction-band bottom in the ''well'' material, V is the barrier height, and m_A and m_B are the effective electron masses in the ''well'' and ''barrier'' materials, respectively. It is obvious that the penetration depth of an electron into the effective barrier vanishes at $E = V$. Thus interference above-barrier localization of an electron can be more effective than localization in an ordinary quantum well. We have shown previously[7,8] that the oscillator strength of an exciton localized above a barrier can be an order of magnitude greater than that of a bulk exciton.

Excitonic states formed by above-barrier electron and hole have been studied experimentally thus far primarily by photoexcitation of luminescence and Raman spectroscopy[4,6] in GaAs/(Al,Ga)As-based periodic structures. In the present work we investigated the system (In, Ga)As/GaAs, which is more suitable for identifying an above-barrier excitonic transition, since in this system the barrier height determined by the offset of the bands in GaAs is known exactly.[8] Moreover, the excitonic absorption-edge spectra as well as the electron and hole dispersion laws have been studied thoroughly in GaAs.

The structure grown by molecular-beam epitaxy at the A. F. Ioffe Physicotechnical Institute consisted of 10.5 periods, each of which included a 13 nm thick GaAs layer surrounded by 10 periods of an $In_{0.1}Ga_{0.9}As$/GaAs superlattice with 3.4 and 6.5 nm thick layers, respectively. The GaAs substrate was completely etched off, which made it possible to measure the transmission spectra of the sample directly. According to calculations, an above-barrier exciton should be formed in this structure by an electron and a hole occupying the first forbidden minibands of the superlattice. Figure 1 shows a section of the sample and the band scheme of the structure as well as the electron and hole wave-function envelopes, calculated by the transfer matrix method, at energies corresponding to the localized above-barrier states. It is evident that both the electron and hole possess compact wave functions which are localized as a result of Bragg interference in the superlattices. Strictly speaking, the Bragg condition holds in this structure only for an electron, but hole confinement by the forbidden valence minibands is just as effective as electron confinement, since the hole mass is larger. The overlap integral between the electron and hole wave functions is $I_{eh} = 0.98$.

2. EXPERIMENT AND ANALYSIS

The light transmission spectra of the sample were measured at liquid-helium temperature in magnetic fields up to 7 T. Figure 2 demonstrates the transmission spectrum in zero field (solid line). Three excitonic resonances, corresponding to transitions marked by arrows in Fig. 1, are clearly seen. These are peaks due to transitions between the first electron and hole minibands (SLE_1), an above-barrier localized exciton (UBE), and also (see Fig. 3) an above-barrier transition between the second allowed minibands for an electron and hole in the superlattice (SLE_2). It is evident that the energy of a localized above-barrier exciton is approximately 30 meV greater than the band gap in GaAs. It is
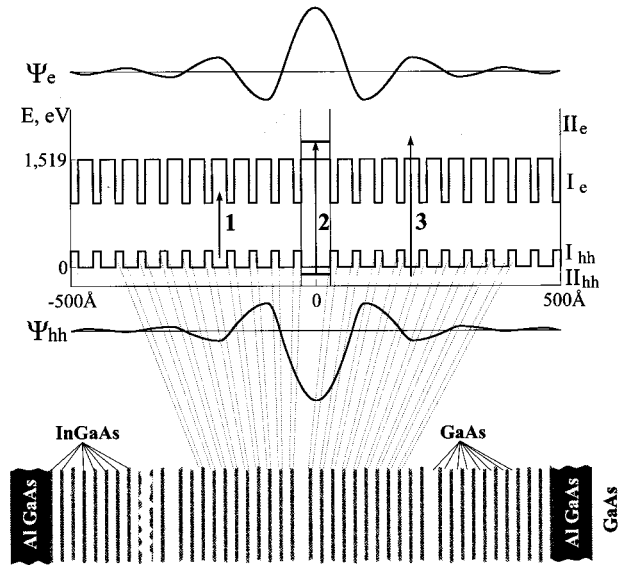
FIG. 1. Schematic band structure and cross section of the sample. At the top and bottom of the band scheme — computed electron and hole envelopes of the wave functions for above-barrier states.
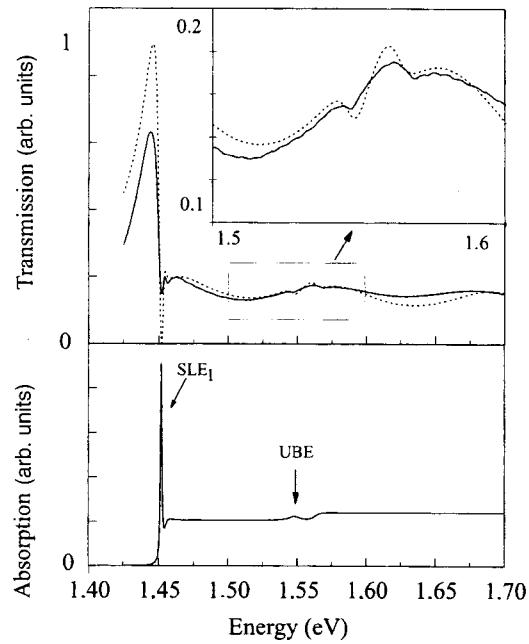

FIG. 2. Light transmission spectrum of the structure: experiment (solid lines) and theory (dotted lines).
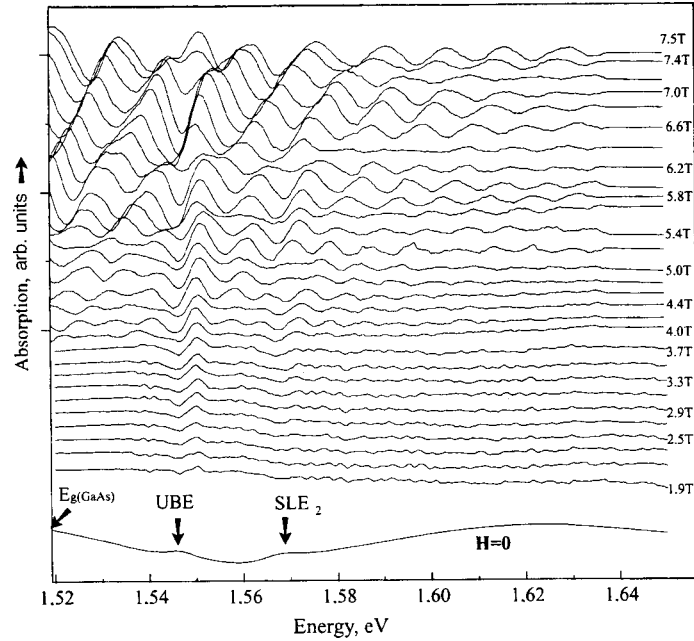
FIG. 3. Absorption spectra in a magnetic field. The arrows mark excitonic transitions, due to an above-barrier state (UBE) and the second minibands of the superlattice (SLE_2), as well as the band gap in GaAs ($E_{g(GaAs)}$).

also important to note that no resonance features in the spectrum are seen at the energy of a bulk exciton in GaAs. This means that the artificial band structure of the superlattice completely dominates the band structure of the constituent crystalline materials. The narrow excitonic lines attest to a high quality of the structure grown, much higher than that of the samples investigated in previous works on an above-barrier exciton.[3-6]

The dotted lines in Fig. 2 show the theoretically computed spectra, obtained by the transfer matrix method with a complex dielectric function containing three resonant terms describing different excitonic transitions as well as an imaginary part with a small frequency dependence, describing interband absorption. The excitonic parameters giving the best agreement with experiment were obtained. The energy $\hbar\omega_0$ of an exciton in the first miniband was found to be 1.452 eV. Its longitudinal–transverse splitting $\hbar\omega_{LT}$ was 0.12 meV, and the damping $\hbar\Gamma$ was 0.5 meV. For the above-barrier exciton these parameters were: $\hbar\omega_0 = 1.548$ eV, $\hbar\omega_{LT} = 0.14$ meV, and $\hbar\Gamma = 5$ meV.

Let us compare the results of first-principles calculations and the excitonic characteristics obtained by fitting the spectra. In this calculation we employed the single-particle electron and hole envelopes, shown in Fig. 1, and the corresponding energies obtained by solving the one-dimensional Schrödinger equation by the transfer-matrix method. The technique which we employed is described in detail in Ref. 7. Using the single-particle functions, we calculated the excitonic state by a variational method using a very simple trial function describing the relative motion of an electron and a hole in the plane:

$$f(\rho) = \sqrt{\frac{2}{\pi}} \frac{1}{a} \exp\left(-\frac{\rho}{a}\right), \tag{2}$$

where a is the variational parameter (the details of the calculation in a magnetic field are given in Ref. 9). To solve the excitonic problem in a superlattice we employed the two-parameter trial function

$$f(\rho,z) = (\pi a_\rho^2 a_z)^{-1/2} \exp\left[-\left(\frac{\rho^2}{a_\rho^2} + \frac{z^2}{a_z^2}\right)^{1/2}\right] \tag{3}$$

and we made use of the approximate method of an effective mass in a miniband. This procedure reduced to elaborating the formalism of Ref. 10 for magnetoexcitons.

The excitonic parameters calculated in this manner were found to be $\hbar\omega_0 = 1.456$ eV, $\hbar\omega_{LT} = 0.13$ meV, and $\hbar\Gamma = 4.8$ meV for an exciton in the first miniband and $\hbar\omega_0 = 1.544$ eV, $\hbar\omega_{LT} = 0.14$ meV, and $\hbar\Gamma = 6$ meV for an above-barrier exciton. Comparing these results with the data presented above it is obvious that the calculation and experiment agree very well, which attests once again to the high quality of the experimental structure.[1)] It is important to note that, as follows from the calculations, the above-barrier exciton possesses binding energy and oscillator strength *greater than* those of the main excitonic state in a superlattice. This confirms the extraordinary efficiency of above-barrier interference localization by the Wigner–von Neumann scenario.

Figures 3 and 4 show the magnetooptic spectra of the structure and the corresponding ''fan diagram,'' i.e., the magnetic field dependence of the energies of the peaks. The initial spectrum in Fig. 3 ($\mathbf{H}=0$) shows two wide smooth maxima, which are the result of interference accompanying reflections at the interfaces of a thin sample and the vacuum. This ''parasitic'' interference can be easily eliminated by dividing the transmission in a field by the transmission without a field (the series of spectra lying below). We underscore the complete absence of any spectral features in the region of the absorption edge of GaAs, the thick-barrier material. Landau quantization is clearly seen for the superlattice exciton and for the above-barrier exciton. Correcting the ''fan diagrams'' by adding the excitonic binding energies to the energies of the absorption peaks, we extracted the true electron cyclotron energies. Further, reconstructing the fan diagrams in reduced-field coordinates with allowance for the numbers of the electron Landau levels, $x = \hbar\omega_0(l+1/2)$, where ω_0 is the electron cyclotron frequency in vacuum, we obtain the curves presented in Fig. 4 which can be described by the following regression laws: $E_1(x) = 1.4553 + 18.04x - 189x^2$ and $E_2(x) = 1.5509 + 14.25x - 13.3x^2$. The cyclotron masses presented, which correspond to the reciprocal of the linear coefficient, were $\mu = 0.054m_0$ for the superlattice exciton and $\mu = 0.07m_0$ for the above-barrier exciton. The latter value agrees well with the effective mass of an electron in GaAs with energy ~ 30 meV above E_g. This means that the mass of the heavy hole forming the above-barrier exciton is infinite in the plane of the layers, which indicates that the above-barrier hole is localized in the plane. Such localization is probably due to monolayer interfacial fluctuations in the structure. If the hole is localized in a plane, the standard selection rules for transitions between electron and hole Landau levels break down and transitions from a lower hole level to all electronic Landau levels contribute to the ''fan.'' This means that the cyclotron mass of the exciton becomes equal to the electron mass.
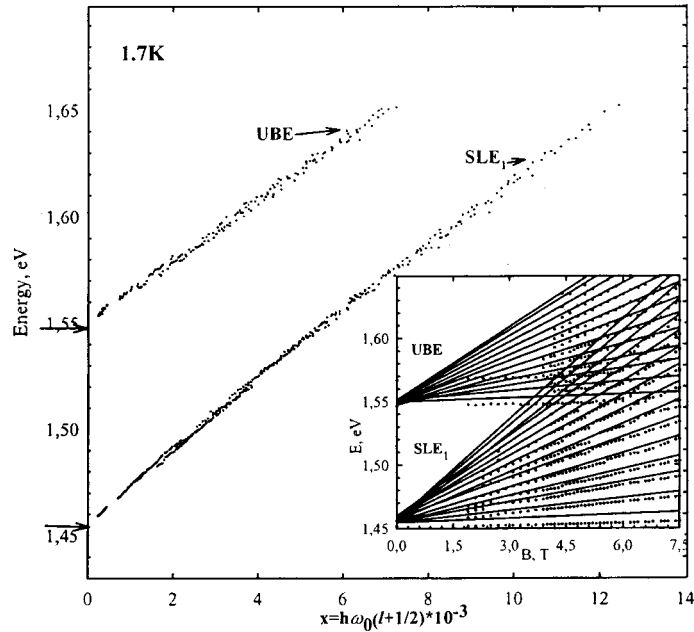
FIG. 4. Fan diagram formed by the main excitonic state (SLE_1) and an above-barrier exciton (UBE) in the coordinates $x = \hbar\omega_0(l + \frac{1}{2})$. The diagram was constructed according to the energies of the experimental peaks adjusted by the computed binding energies of excitons (see inset). The slope of these lines gives the reduced cyclotron mass as a function of the transition energy.

*)e-mail: rseis@ffm.ioffe.rssi.ru
1)V. M. Ustinov (A. F. Ioffe Physicotechnical Institute) prepared and kindly provided the samples.

[1] J. von Neumann and E. Wigner, Phys. Z. **30**, 465 (1929).

[2] F. H. Stillinger and D. R. Herrick, Phys. Rev. A **11**, 446 (1975).

[3] C. Sirtori, F. Capasso, J. Faist *et al.*, Appl. Phys. Lett. **61**, 898 (1992).

[4] M. Zahler, I. Brener, G. Lenz *et al.*, Appl. Phys. Lett. **61**, 949 (1992).

[5] F. Capasso, C. Sirtori, J. Faist *et al.*, Nature (London) **358**, 565 (1992).

[6] M. Zahler, E. Cohen, J. Salzman *et al.*, Phys. Rev. Lett. **71**, 420 (1993).

[7] M. R. Vladimirova and A. V. Kavokin, Fiz. Tverd. Tela (St. Petersburg) **37**, 2163 (1995) [Phys. Solid State **37**, 1178 (1995)].

[8] A. V. Kavokin, M. R. Vladimirova, R. P. Seisyan *et al.*, in *Semiconductor Heteroepitaxy: Growth, Characterization and Device Applications*, edited by B. Gil and R.-L. Aulombard (World Scientific, Singapore, 1995), p. 482.

[9] A. V. Kavokin, A. I. Nesvizhskii, and R. P. Seisyan, Fiz. Tekh. Poluprovodn. **27**, 977 (1993) [Semiconductors **27**, 530 (1993)].

[10] E. L. Ivchenko and A. V. Kavokin, Fiz. Tekh. Poluprovodn. **25**, 1780 (1981) [Sov. Phys. Semicond. **25**, 1070 (1991).

Translated by M. E. Alferieff

Anomalous magnetic properties of the complex $(ET)_2C_{60}$

S. V. Demishev, A. A. Pronin, and N. E. Sluchanko

Institute of General Physics, Russian Academy of Sciences, 117942 Moscow, Russia

L. Weckhuysen and V. V. Moshchalkov

Laboratorium voor Vaste-Stoffysica en Magnetisme, K. U. Leuven, B-3001 Leuven, Belgium

N. G. Spitsina and É. B. Yagubskiĭ

Institute of Chemical Physics, Russian Academy of Sciences, 142432 Chernogolovka, Moscow Region, Russia

Investigations of the temperature dependences of the magnetic permeability and dielectric permittivity in the temperature range $4.2 \text{ K} \leq T \leq 300 \text{ K}$ and the field dependence of the magnetization $M(B)$ in fields $B \leq 50$ T show that the magnetic properties of the complex $(ET)_2C_{60}$ cannot be described on the basis of the standard model, which assumes that the paramagnetic oxygen impurity makes the dominant contribution. It is found that the magnetism in $(ET)_2C_{60}$ is due to the diamagnetic properties of the C_{60} and ET molecules and to specific paramagnetic centers of the type C_{60}^-, which possess an anomalously low g factor $|g| \approx 0.14$. An *experimentum crucis* is proposed for checking the oxygen paramagnetic center model for pure C_{60} films. © *1999 American Institute of Physics.* [S0021-3640(99)01210-4]

PACS numbers: 81.05.Tp, 81.40.Rs, 75.20.Ck, 77.22.Ch

1. According to the conventional point of view, the magnetic[1,2] and dielectric[3] properties of C_{60} fullerene are determined by oxygen impurity. For example, the experimental data on the temperature dependence of the magnetic susceptibility[1,2] can be represented as a sum of two terms

$$\chi(T) = \chi_{\text{dia}} + \chi_{\text{para}}(T), \tag{1}$$

where χ_{dia} is a negative constant and χ_{para} is positive and increases with decreasing temperature, following the Curie law $\chi_{\text{para}} \sim 1/T$. It is the existence of the paramagnetic contribution $\chi_{\text{para}}(T)$ that is ordinarily attributed to oxygen impurity, while the diamagnetic contribution χ_{dia} is due to the internal properties of the C_{60} molecule.[1,2] In the opinion of the authors of Ref. 3 the dipole moments of the oxygen molecules also completely determine the temperature and frequency dependences of the permittivity.

It should be noted that the dielectric and magnetic characteristics of C_{60} films depend strongly on the preparation and annealing conditions:[1-4] Annealing can change the oxygen impurity density and the properties of the C_{60} matrix, making it difficult
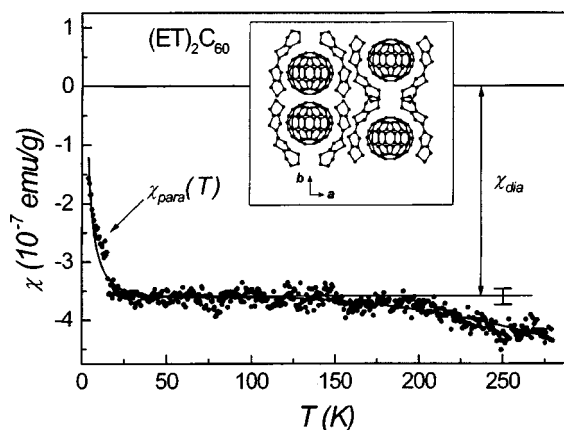
785

FIG. 1. Temperature dependence of the magnetic susceptibility in $(ET)_2C_{60}$ for $B < 6$ T. Dots — experiment; solid line — fit using Eq. (2). The statistical fitting error for the parameters presented in the text is shown on the straight line corresponding to the χ_{dia} = const region. Inset: $(ET)_2C_{60}$ structure in the crystallographic **ab** plane.

to distinguish these effects unequivocally. Single crystals of fullerene–organic donor complexes, characterized by small charge transfer, may be more promising from this standpoint.[5,6] This situation occurs in $(ET)_2C_{60}$, where ET is bis(ethylenedithio)tetrathiafulvalene.[5,6]

In the present letter we shall show that for $(ET)_2C_{60}$, even though the temperature dependence of the magnetic susceptibility has the form (1) and a substantial correlation remains between the magnetic and dielectric properties, the magnetic properties cannot be satisfactorily described in a model based on oxygen impurity. Moreover, experiments performed in a strong magnetic field $B < 50$ T show that the characteristics of the hypothetical paramagnetic center must be either substantially modified or this model cannot be used at all to explain the magnetic properties. We note that the magnetic properties of C_{60}-based compounds and C_{60} molecular complexes in strong magnetic fields have, for all practical purposes, not been studied.

2. The experiments were performed on $2 \times 1 \times 0.5$ mm $(ET)_2C_{60}$ single crystals. The structural characteristics of the samples were identical to those obtained previously in Refs. 5 and 6. During the investigation of the magnetization the magnetic field vector lay in the crystallographic **ab** plane (the arrangement of the C_{60} and ET molecules in this plane is shown in the inset in Fig. 1).

The temperature dependence of the magnetization $M(T)$ in fields $B \leqslant 6$ T was measured in the temperature range 4.2–300 K on an Oxford Instruments vibrating coil magnetometer. The field dependence of the magnetization $M(B)$ in fields up to 50 T at liquid-helium temperatures was investigated on the pulsed-field apparatus at Catholic University in Leuven (Belgium). An induction method was used to determine $M(B)$ in strong fields,[7] and both electronic compensation and control experiments with an empty measuring coil were used to distinguish accurately the signal due to the sample. The measurements of the dielectric properties of $(ET)_2C_{60}$ in the range 10–100 MHz were performed using an apparatus based on a NR-4191 A impedance meter, described in Ref. 8.
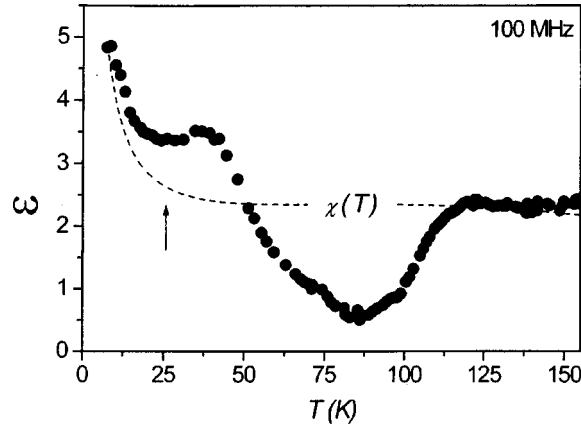
FIG. 2. Temperature dependence of the permittivity at 100 MHz in $(ET)_2C_{60}$. The dashed curve shows the temperature dependence of χ [the results of fitting Eq. (2)]. The arrow marks the low-temperature section of growth of $\chi(T)$ and $\epsilon(T)$.

3. The temperature dependence of the magnetic susceptibility for $(ET)_2C_{60}$ is shown in Fig. 1. One can see that qualitatively the curve $\chi(T)$ corresponds to Eq. (1): At room temperature $\chi(T)<0$, while for $T<25$ K ''paramagnetic'' growth of χ is observed. At the same time, χ_{dia} remains constant only in the range $25<T<200$ K, while for $T>200$ K the susceptibility decreases somewhat with temperature (Fig. 1). In the entire temperature range $1.8<T<300$ K the empirical formula

$$\chi(T)=a+bT+cT^2+p/T, \tag{2}$$

where $a=-4.03\times10^{-7}$, $b=5.6\times10^{-10}$, $c=-2.42\times10^{-12}$, $p=1.05\times10^{-6}$, and $\chi(T)$ is measured in cm^3/g (emu/g) and T in K, can be used to fit the experimental data on $\chi(T)$.

It is interesting that $\chi\approx-3.5\times10^{-7}$ cm^3/g in the plateau region 25 K$<T$ <200 K. This value is essentially identical to the value of χ_{dia} for C_{60}.[1,2] However, 1 g of C_{60} contains 8.6×10^{20} C_{60} molecules, while $(ET)_2C_{60}$ is a dilute system, 1 g of which contains 4×10^{20} C_{60} molecules. As a result, the diamagnetic response per C_{60} molecule for $(ET)_2C_{60}$ is approximately two times stronger than for pure C_{60}. It is natural to infer that the ''additional diamagnetism'' in $(ET)_2C_{60}$ is due to ET molecules with completely filled electron shells and occupying the ground state. This situation agrees with the idea of small charge transfer in the $(ET)_2C_{60}$ complex,[5,6] since for a chemical bond with strong charge transfer the ET molecules will exhibit not diamagnetic but rather paramagnetic properties.[9]

We note that the ''paramagnetic'' contribution to $\chi(T)$ in $(ET)_2C_{60}$ is much smaller than for pure C_{60}, as a result of which the experimental samples remained diamagnetic even at liquid-helium temperatures (Fig. 1). At first glance such behavior can be attributed to the lower oxygen impurity density in $(ET)_2C_{60}$ single crystals compared with C_{60} films.

The correlation between the temperature dependences of the permittivity $\epsilon(T)$ and magnetic susceptibility also agrees qualitatively with the ''oxygen model'' (Fig. 2). For
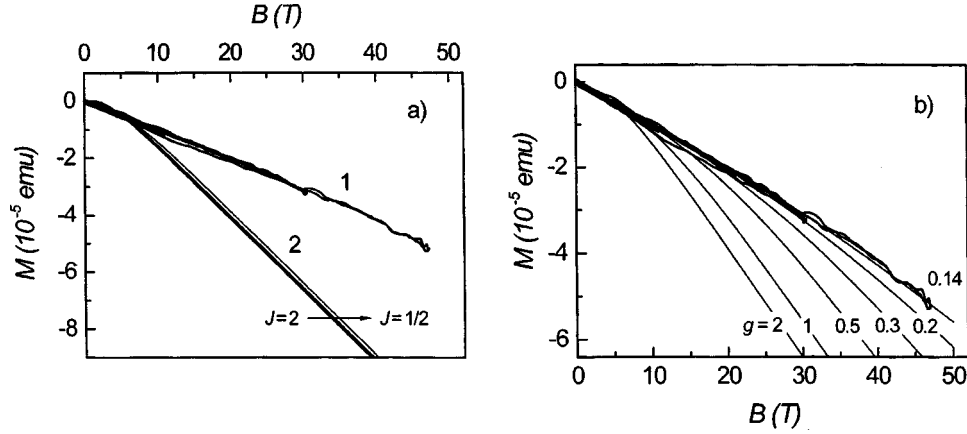
FIG. 3. a) Experimental field dependence of the magnetic moment at $T=4.2$ K (*1*) and computational results obtained in the paramagnetic oxygen impurity model (*2*). b) Model calculation for a paramagnetic center with a renormalized g factor (see text); the numbers on the curves correspond to the values of the g factor.

$T>100$ K $\epsilon\approx$ const, while for $T<25$ K a kink is observed in the curve $\epsilon(T)$, and the permittivity and magnetic susceptibility increase with decreasing temperature. We note that the minimum of $\epsilon(T)$ near $T\approx80$ K (Fig. 2) is apparently due to the fact that the rotation of C_{60} molecules is ''frozen'' (order–disorder transition[1]) in this temperature range. According to the data of Ref. 10, the frequency of dipole transitions in this range is of the order of the measurement frequency $f\approx10-100$ MHz. This is what leads to the features in the temperature dependence $e(T)$. A more detailed description of dielectric relaxation in $(ET)_2C_{60}$ will be given in a separate report.

4. If the oxygen paramagnetic impurity model is valid, then the field dependence of the magnetization of $(ET)_2C_{60}$ at low temperatures should be strongly nonlinear. From Eq. (1) follows the expression

$$M(B,T)=M(B,T)_{\text{para}}+M(B,T)_{\text{dia}}\equiv\frac{3\chi_{\text{para}}(T)k_BT}{(J+1)g\mu_B}B_J\left(\frac{g\mu_BJB}{k_BT}\right)+M_{\text{dia}}(B,T), \quad (3)$$

where $M_{\text{dia}}(B,T)=\chi_{\text{dia}}B$ to a first approximation. In Eq. (3) $B_J(\chi)$ is the Brillouin function, the Landé g factor and total angular momentum J set the characteristics of the paramagnetic impurity, and $\chi_{\text{para}}(T)$ is described by the Curie law. However, although for $T\leqslant25$ K the amplitudes χ_{para} and χ_{dia} in $(ET)_2C_{60}$ are comparable (Fig. 1), it was found that right up to the field $B=6$ T reached in a vibrating coil magnetometer the magnetization of the sample was proportional to the field $M\sim B$.

Measurements of $M(B)$ at $T=4.2$ K performed in pulsed fields up to 50 T showed that the field dependence of the magnetic moment remains linear for $B\leqslant30$ T, while for $B>30$ T a small deviation downwards from linear asymptotic behavior is observed (Fig. 3a, curve *1*).

Since the ESR data[4] for oxygen impurity in C_{60} show that $g\approx2$, it can be assumed that the orbital angular momentum is frozen.[11] Then, in the most general case the parameter J in Eq. (3) can vary from $J=1/2$ (O^- ion) to $J=2$ (O_2 molecule). Since the values

of χ_{para} and χ_{dia} at $T = 4.2$ K are known (Fig. 1), Eq. (3) contains no free parameters other than the total angular momentum J. The family of curves $M(B, T = 4.2$ K) calculated using Eq. (3) for various values of J ($J = 1/2, 1, 3/2, 2$) is presented in Fig. 3a (curves *2*). Comparing the computational results with experiment (Fig. 3a, curves *1* and *2*), it is easy to see that the experimental data on the field dependence of the magnetization cannot be explained on the basis of the paramagnetic oxygen impurity hypothesis.

Nonetheless, the paramagnetic center model [Eq. (3)] can be used to give a quantitative description of the $M(B)$ data if the possibility of strong renormalization of the g factor is admitted. To obtain an estimate we set $J = 1/2$. Then it follows from the data in Fig. 3b that for $(ET)_2C_{60}$ $g \approx 0.14$. We note that Eq. (3) correctly describes the curvature of the experimental curve $M(B)$ (Fig. 3).

In summary, the hypothetical paramagnetic center in $(ET)_2C_{60}$ apparently must possess anomalously small values of the g factor. In principle, for $(ET)_2C_{60}$ a charged ET molecule could play the role of such a center, but at present there are no experimental data attesting to a low g factor for these molecules. At the same time, a strong renormalization of the g factor is predicted for the C_{60}^- ion, in whose ground state a small negative g factor $g \approx -0.1$ can be expected as a result of the dynamic Jahn–Teller effect.[12] For $(ET)_2C_{60}$ it is known that the excess electron density is localized on the C_{60} molecule,[13] so that the existence of C_{60}^- type defects seems to us to be very likely. We note that Eq. (3) does not depend on the sign of the g factor, and therefore the data in Fig. 3b can be interpreted as confirming the model where the C_{60}^- ion plays the role of a paramagnetic center. The g value $|g| \approx 0.14$ found is close to the theoretical value $|g| \approx 0.1$ calculated in Ref. 12 from first principles.

The exotic characteristics of the hypothetical paramagnetic center that are necessary in order to use Eq. (3) to give a quantitative description of the experiment show that alternative physical mechanisms giving rise to the anomalies in the magnetic properties of C_{60} and not related with the magnetic impurities can be realized. As an example, let us consider the classical expression for the diamagnetic susceptibility of a molecule[14]

$$\chi = -\frac{Ne^2}{6mc^2} \sum_{k=1}^{z} \langle nm | r_k^2 | nm \rangle + \frac{3}{2} \sum_{n',m'} \frac{|\langle n,m|\hat{M}(0)|n',m'\rangle|^2}{E_{n',m'} - E_{nm}}, \tag{4}$$

where the second term describes van Vleck paramagnetism (the notations used in Eq. (4) are identical to those of Ref. 14). It is known that for spherically symmetric states all off-diagonal elements with $n'm' = nm$ are zero, and the second term in Eq. (4) vanishes.[14] For this reason, χ can be related with the symmetry and spatial characteristics of the wave functions of the molecules forming the complex. From this standpoint the data in Fig. 1 reflect a possible change in the geometry of the bonds in C_{60} and (or) ET molecules in the crystals with decreasing temperature, leading to an increase in van Vleck paramagnetism that compensates the first term in Eq. (4). It is important that in the range of applicability of relation (4) $M(B) = \chi B$ (Ref. 14) and the field dependence of the magnetization should be close to linear in the entire experimental temperature range (including in the range $T < 25$ K, where partial compensation of the diamagnetic contribution by the paramagnetic contribution is observed). Therefore this mechanism makes it
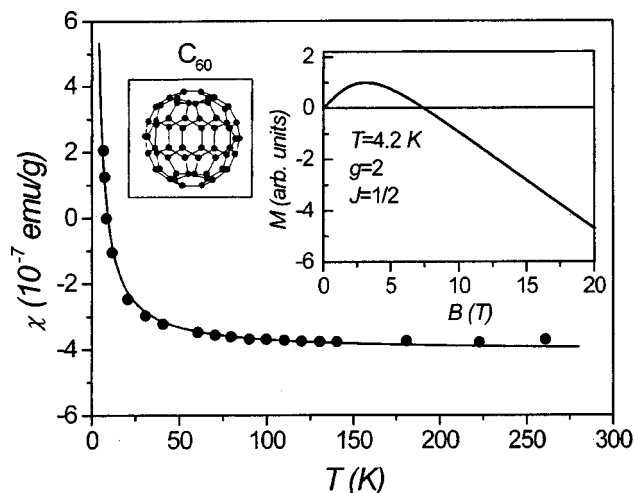
FIG. 4. Temperature dependence of the magnetic susceptibility of pure C_{60} according to the data from Refs. 1 and 2 and the expected behavior of the curve $M(B)$ in the paramagnetic center model with $g = 2$ and $J = 1/2$.

possible to explain the weak nonlinearity of the field dependence $M(B)$ at liquid-helium temperatures (Fig. 3), but the reason for possible changes in the structure of the bonds in $(ET)_2C_{60}$ at low temperatures remains undetermined.

5. The above analysis of the experimental results shows that the magnetic properties of $(ET)_2C_{60}$ are not related with the paramagnetic oxygen impurity and reflect the internal properties of the crystal. The most likely situation is one in which the diamagnetism is due to the properties of the neutral C_{60} and ET molecules and the paramagnetism is due to specific paramagnetic defects, such as a C_{60}^- ion, which possess an anomalously low g factor $|g| \approx 0.14$. In such a situation the correlation between the magnetic and dielectric properties of $(ET)_2C_{60}$ indicates that even the permittivity does not depend on the oxygen impurity but rather it is determined by the internal properties of the material. We note that the authors of Ref. 10, where the dielectric properties of C_{60} films were investigated, arrived at a similar conclusion.

The data from the present investigation cast doubt on the adequacy of the "oxygen" interpretation of the magnetic properties of pure C_{60}. Using Eq. (3) and the published data[1,2] on $\chi(T)$ for C_{60}, it is easy to calculate the possible form of the field dependence of the magnetization for a paramagnetic impurity with $g = 2$ and $J = 1/2$ (Fig. 4). It is evident that at liquid-helium temperatures a strong nonlinearity and a change in sign of M should occur near $B \approx 7$ T (inset in Fig. 4). At the same time, if the ideas developed in the present letter are applicable for pure C_{60}, then a weaker, closer to linear, dependence $M(B)$ can probably be expected. Thus, the investigation of the magnetic properties of fullerenes in strong magnetic field becomes an experimentum crucis for the paramagnetic oxygen impurity model. Further experiments in this field are therefore crucial.

[1] M. S. Dresselhaus, G. Dresselhaus, and P. C. Eclund, *Science of Fullerenes and Carbon Nanotubes*, (Academic Press, San Diego, 1996), p. 739.

[2] V. Buntar, H. W. Weber, and M. Ricco, Solid State Commun. **98**, 175 (1995).

[3] B. Pevzner, A. F. Hebard, and M. S. Dresselhaus, Phys. Rev. B **55**, 16439 (1997).

[4] Y. Ishijima and T. Ishiguro, J. Phys. Soc. Jpn. **66**, 2948 (1997).

[5] A. Izuoka, T. Tachikawa, T. Sugowara *et al.*, J. Chem. Soc., Chem. Commun., No. 19, 1472 (1992).

[6] N. G. Spitsina, V. N. Semkin, and A. Graja, Acta Phys. Pol. A **87**, 869 (1995).

[7] F. Herlach, C. C. Agosta, R. Bogaerts *et al.*, Physica B **216**, 161 (1996).

[8] S. V. Demishev, A. A. Pronin, N. E. Sluchanko *et al.*, JETP Lett. **65**, 342 (1997).

[9] J. Woznitsa, in *Springer Tracts in Modern Physics*, Vol. 134, Springer-Verlag, New York, 1996.

[10] P. Mondal, P. Lunkenheimer, and A. Loidl, Z. Phys. B **99**, 527 (1996).

[11] K. A. Maklochlan, *Magnetic Resonance* [in Russian] (Khimiya, Moscow, 1976), p. 55.

[12] E. Tosatti, N. Manini, and O. Gunnarson, Phys. Rev. B **54**, 17184 (1996).

[13] Yu. M. Shul'ga, V. I. Rubtsov, and N. G. Spitsina, Zh. Fiz. Khim. **70**, 564 (1996).

[14] S. V. Vonsovskiĭ, *The Modern Science of Magnetism* [in Russian] (Gos. Izd. Tekh.-Teor. Lit., Moscow, 1951), p. 97.

Translated by M. E. Alferieff

Antiferromagnetism in hydrated 123 compounds

A. V. Dooglav

Magnetic Resonance Laboratory, Kazan State University, 420008 Kazan, Russia;
Laboratoire de Physique des Solides, Universite de Paris-Sud, 91405 Orsay, France

A. V. Egorov, I. R. Mukhamedshin, and A. V. Savinkov

Magnetic Resonance Laboratory, Kazan State University, 420008 Kazan, Russia

H. Alloul, J. Bobroff, W. A. MacFarlane, and P. Mendels

Laboratoire de Physique des Solides, Universite de Paris-Sud, 91405 Orsay, France

G. Collin, N. Blanchard, and P. G. Picard

Laboratoire de Leon Brillouin, CE Saclay, CEA-CNRS, 91191 Gif-sur-Yvette, France

Copper nuclear quadrupole resonance and zero-field nuclear magnetic resonance (ZFNMR) studies of $YBa_2Cu_3O_{6.5}$ show that a magnetic phase appears in underdoped 123 superconductors treated in ambient moist air. The studies give convincing evidence that the ''empty'' CuO chains play the role of easy water insertion channels. The reaction occurs first in ordered regions of the crystallites. The final product of the reaction is a nonsuperconducting antiferromagnetic compound characterized by at least two types of magnetically ordered copper ions, with ZFNMR spectra in the frequency ranges 46–96 and 96–135 MHz, respectively. Even for powder samples fixed in an epoxy resin, this reaction is found to have partially occurred after a few years. © *1999 American Institute of Physics.* [S0021-3640(99)01310-9]

PACS numbers: 74.72.Bk, 74.25.Ha, 75.50.Gg, 76.60.Gv

The idea of coexistence of superconductivity and local antiferromagnetism in high-temperature superconductors (HTSCs) is appearing more and more frequently in theoretical and experimental papers. Recently we found[1] that in aged samples of $YBa_2Cu_3O_{6+x}$ with $x < 0.8$, which had been packed in paraffin and kept at room temperature for about 6 years, the superconducting volume fraction had decreased substantially. We also found that, along with the typical copper nuclear quadrupole resonance (NQR) spectrum of the superconducting 1-2-3 system, these samples also exhibited copper zero-field nuclear magnetic resonance (ZFNMR) spectra in the frequency range 46–135 MHz, indicating the presence of a magnetically ordered phase which remains observable up to 200 K.

The initial goal of this study was to find a way of artificially aging the compound to produce the magnetic phase. At the time of our previous report,[1] we considered the presence of the magnetic phase to be the result of stripe pinning due to the Ortho-III

phase, which was well-ordered during the very long-term room-temperature annealing, so we began the artificial aging experiments with attempts to accelerate the oxygen ordering process. It is known[2] that the temperature boundary of the Ortho-III phase is about 75 °C, so the first experiments were devoted to annealing at 55–60 °C for a few weeks, but this failed to produce the magnetic phase. Further attempts were therefore undertaken at somewhat higher temperatures. Finally we managed to get a small amount of magnetic phase exhibiting the characteristic ZFNMR spectra.[1] However, the mass of the samples during the ambient air annealing had increased, and controlled annealing of dry powder sealed in an ampoule showed neither the mass changes nor the appearance of the magnetic phase.

The most natural explanation for the mass increase is the occurrence of a chemical reaction of YBCO with components of the air, in particular, with water vapor, since the significant reactivity of 123 with water is well established. Most of the early papers on the reaction of 123 with water reported reaction products such as Y_2BaCuO_5 (''green phase''), CuO, $BaCO_3$, and some others. Some of these compounds are antiferromagnets having either low Néel temperatures (15–30 K) or ZFNMR spectra very different from the one we observed in Ref. 1. More recent studies (see Ref. 3 and references therein) using high-resolution electron microscopy and x rays have shown that the 123 superconductors react with water vapor via a topotactic mechanism. The final product of this reaction, which occurs in a bulk material at 75–250 °C, is a so-called pseudo-248 phase $H_{2z}YBa_2Cu_3O_{6+x+z}$ (isostructural with the familiar 248 structure but with 50% of the $Cu(1)$ sites vacant; it is referred to as phase *B* in Ref. 3).

For NQR and NMR studies of the changes occuring in 123 HTSCs under reaction with water vapor, a number of samples with different water contents were prepared. As the starting material we used samples of $YBa_2Cu_3O_{6.5}$ ($T_c = 56$ K) in the form of a free powder with a particle size of about 30 μm, freshly synthesized using the conventional solid-state reaction of powdered Y_2O_3, BaO, and CuO at about 940 °C, with periodic interruptions for grinding. The free powder was annealed in air at 150 °C. A vapor pressure (about 35 mbar at 150 °C) was established in a closed furnace by evaporation. The samples were weighed periodically to measure the water uptake. After annealing all samples were packed in Stycast 1266A epoxy. With this procedure, we obtained a number of samples of $YBa_2Cu_3O_{6.5}(H_2O)_z$ with water concentrations $z = 0$, 0.14, 0.24, 0.55, and 1.2, the last value being the maximum water uptake, beyond which further annealing did not yield a mass increase.

Home-built pulsed NMR spectrometers were used to measure NQR and ZFNMR spectra at 4.2 K. The copper NQR spectra of the annealed free-powder samples are shown in Fig. 1. Since the nuclear spin–lattice relaxation rate of the ''chain'' copper is significantly slower than that of the ''plane'' copper,[1] it is possible to separate their spectra (Fig. 1b and 1c). The large difference in their transverse relaxation rates can also be used for separation of the spectra. The assignment of different NQR lines to the nuclei of $Cu(1)$ residing in different oxygen coordinations is done in Ref. 4. The rapidly relaxing part of the copper NQR spectrum (Fig. 1c) is usually assigned to the plane copper nuclei. It consists of two groups of lines at frequencies 30.8 and 28 MHz for the isotope $^{63}Cu(2)$. To simplify the discussion, hereafter we will discuss only the frequencies and intensities of the NQR lines for this isotope; naturally, the corresponding ^{65}Cu lines are also observed.
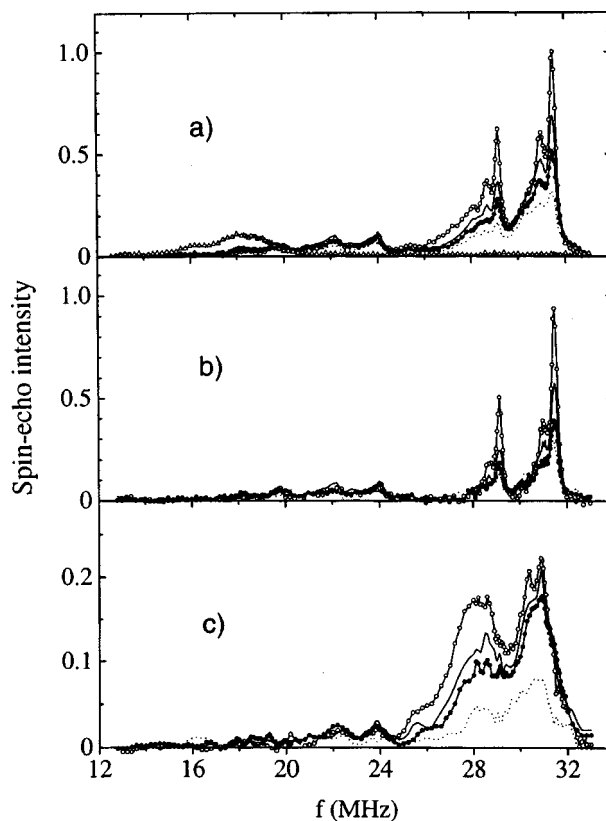
FIG. 1. Copper NQR spectra for $YBa_2Cu_3O_{6.5}$ with different water uptake z (open circles, solid line, solid circles, dotted line, and open triangles correspond to $z = 0$, 0.14, 0.24, 0.55, and 1.2, respectively): a) as-taken spectra; b) slowly relaxing part of the spectra (Cu(1) spectra); c) rapidly relaxing part. For details see text.

One can see in Fig. 1 that the intensity of the copper NQR spectrum decreases with increasing water uptake. It is remarkable that at the initial stage of the reaction (at a small water uptake) the narrow ^{63}Cu NQR lines at 31.5 and 31 MHz, i.e., the lines of $^{63}Cu^+$ nuclei belonging to the "empty" ... – Cu – Cu – ... chains located between two "full" ... – Cu – O – Cu – ... chains (31.5 MHz, Ortho-II phase) and between "full" and "empty" chains,[4] begin to disappear first. At the same time the broad, rapidly relaxing line at 28 MHz (the plane $^{63}Cu^{2+}(2)$) also decreases. At water uptake of approximately 0.5 molecules of H_2O per $YBa_2Cu_3O_{6.5}$, the narrow lines of Cu(1) and the Cu(2) line at 28 MHz are practically absent in the NQR spectrum, and the intensity of the NQR line of Cu(2) at 30.8 MHz has decreased by a factor of 2 compared to the unreacted compound. The intensity of the NQR line belonging to the threefold-coordinated copper nuclei (located at the ends of the chains, 24 MHz) doesn't change significantly, though a small increase of its intensity at the first stages of water uptake was noted. At maximum water uptake (1.2 molecules) the copper NQR spectrum typical for $YBa_2Cu_3O_{6.5}$ has disappeared, giving way to a broad copper NQR line at 18.4 MHz.

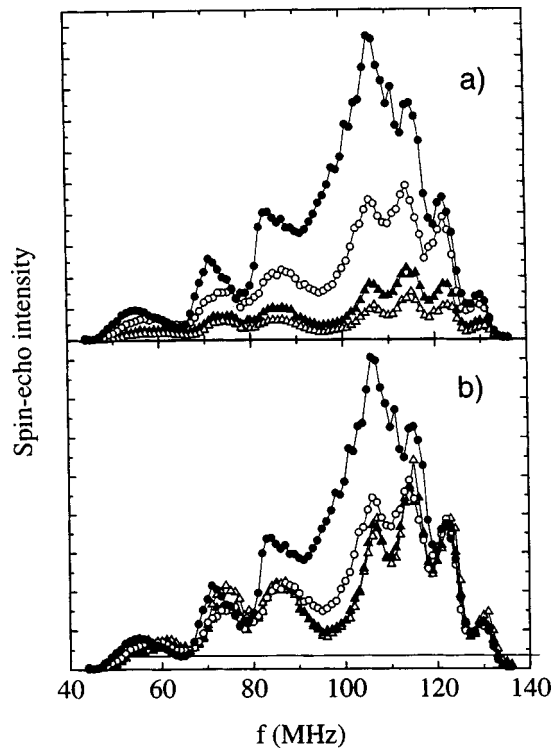The copper ZFNMR spectra of annealed free-powder samples are shown in Fig. 2.

FIG. 2. Copper ZFNMR spectra for $YBa_2Cu_3O_{6.5}$ with different water uptake z (open and solid triangles and open and solid circles correspond to $z = 0.14$, 0.24, 0.55, and 1.2, respectively): a) as-taken spectra; b) spectra normalized by water uptake; the spectrum for $z = 1.2$ is normalized by 0.6.

At low water uptake ($z < 0.5$) the spectrum, as in Ref. 1, consists of two groups of well-resolved lines. The low-frequency group (46–96 MHz) resembles the Cu(2) ZFNMR spectrum of antiferromagnetic $PrBa_2Cu_3O_7$ (Ref. 5) and corresponds to a hyperfine magnetic field of ~ 64 kOe at the copper nucleus and to a quadrupolar frequency of $\nu_Q \approx 30$ MHz. A field of about 103 kOe and $\nu_Q \approx 16$ MHz produces a high-frequency group (96–135 MHz), this part of the spectrum is practically identical to that[6] of the antiferromagnet Nd_2CuO_4. The relative intensity of the two groups, corrected for the difference in transverse relaxation rate and the (square) frequency dependence, is estimated to be $I_{\text{LFG}}/I_{\text{HFG}} = 1 \pm 0.5$.

The intensities of both groups of the spectrum scale with water uptake for $z < 0.5$ (Fig. 2b), while for $z > 0.5$ a new component appears and grows to maximum intensity in the sample with the maximum water uptake. Although the separate lines of this component are not well resolved, it can be assigned to copper nuclei located in a hyperfine field of approximately 80 kOe, just as in the compound $YBa_2Cu_3O_6$.

Changes in the superconducting volume fraction were determined by measuring the ac diamagnetic susceptibility ($H_1 \approx 1$ Oe, $f = 1$ kHz). The superconducting volume fraction decreases with water uptake (Fig. 3), while T_c remains practically unchanged. The sample with maximum water uptake is completely nonsuperconducting.
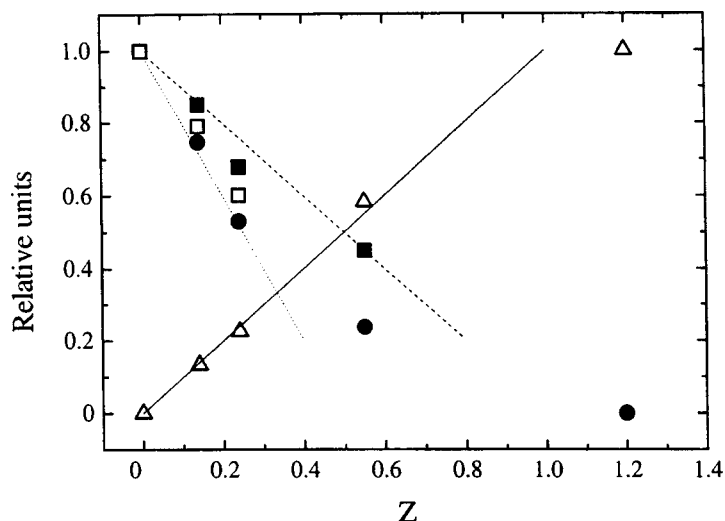
FIG. 3. Superconducting volume fraction (solid circles), copper NQR spectra intensity (solid squares), NQR intensity of slowly relaxing Cu(1) nuclei (open squares), and ZFNMR intensity (triangles) versus water uptake z. The straight lines represent the functions $y = z$ (solid line), $y = 1 - z$ (dashed line), and $y = 1 - 2z$ (dotted line).

So, in accordance with Ref. 3, we conclude that insertion of water into a 123 compound proceeds in two stages. The first stage ($z < 0.5$) is characterized by the presence of two types of magnetically ordered copper ions, whose nuclei experience internal magnetic fields of 64 and 100 kOe. The changes of the copper NQR spectra described above provide straightforward evidence that Cu(1) chains that contain no oxygen and belong to the well-developed Ortho-II phase present an easy diffusion path for the insertion of water or other related species (e.g., hydroxide ions). The superconducting volume fraction decreases at this stage approximately at the same rate as the sharp Cu(1) NQR lines do, but twice as fast as the total NQR intensity in the 21–33 MHz range (Fig. 3). The superconducting volume fraction for the sample with $z = 0.55$ is only 14% of that for $z = 0$. The simultaneous disappearance of the broad, rapidly relaxing NQR line at 28 MHz allows us to assign it to Cu(2) nuclei belonging to the well-developed Ortho-II phase. It is quite reasonable to suppose[3] that water diffusion is hampered in areas of oxygen disorder within the crystallites, i.e., in areas where the empty-chain diffusion channels are blocked by oxygen in O5 positions, twin boundaries, etc. From this, we assign the ''residual'' NQR spectrum of the $z = 0.55$ sample primarily to such areas. A small increase of the intensity of the terminating Cu(1) NQR line (at 24 MHz) at the initial stage of the reaction is thus most likely due to the destruction of long Cu(1) chains.

Our studies of water insertion allow us to tentatively clarify the often debated question: Do all the nuclei from the superconducting regions of 123 contribute to the NQR/NMR signal, i.e., does the rf field fully penetrate superconducting 123? The observed correlation of the copper NQR intensity, superconducting volume fraction, and water uptake allows us to conclude that *all* superconducting regions contribute to the NQR signal in the case of underdoped $YBa_2Cu_3O_{6.5}$ in the form of 30-μm powder packed in Stycast. For comparison, our attempt to insert water (two hours 200 °C annealing) into $YBa_2Cu_3O_7$ lead to a 30% decrease of the superconducting volume fraction, but due to

better rf field penetration into a ''spoiled'' superconductor we observed a 20% *increase* of the observed Cu(2) NQR intensity.

The second stage of the reaction ($z > 0.5$) leads to total disappearance of superconductivity and to dramatic changes in the NQR spectrum (Fig. 1). At maximum water uptake $z_{max} = 1.2$ (different from $z_{max} = 1$ in Ref. 3) two new copper centers arise: one characterized by a hyperfine field ~ 80 kOe at the Cu nuclei, and another with a nuclear quadrupole frequency of 18.4 MHz and a lack of magnetic ordering. It should be mentioned that magnetically ordered areas which have appeared at $z < 0.5$ are still present and become even larger at $z = 1.2$. As estimated by relative intensities of ZFNMR spectra, they represent about 70–80% of the total number of Cu ions participating in well-ordered magnetic phase(s), which corresponds to about one water molecule ($z \approx 1$) involved in producing this phase.

X-ray diffraction spectra taken for the sample with a maximum water uptake show that the final product of the reaction in our case is identical to the one considered in Ref. 3 as the tetragonal pseudo-248 structure with 50% defects at chain copper positions (phase *B* in Ref. 3). In this structure there are 3 inequivalent Cu sites. We could identify at least 3 in the magnetically ordered phase, and we find an additional relatively weak copper NQR line at 18.4 MHz (not far from the 19.8 MHz Cu(1) NQR line in $YBa_2Cu_4O_8$). Further studies are necessary to relate the NMR spectra in detail to the structure.

Our copper NQR/ZFNMR studies of the reaction of $YBa_2Cu_3O_{6.5}$ compound with water vapor give straightforward evidence that ''empty'' CuO chains play the role of easy water insertion channels. The most highly ordered regions of the crystallites react most easily. The water insertion reaction proceeds very slowly at room temperature, but over 6 years in air, water reaches even samples packed in paraffin.[1] At 100–200 °C the reaction proceeds quickly (in few days). The final product of the reaction is a nonsuperconducting antiferromagnet characterized by at least two types of magnetically ordered copper ions, with ZFNMR spectra in the frequency ranges 46–96 and 96–135 MHz. This antiferromagnetic signal, indicating decomposition of the superconductor, was even detected in samples packed in Stycast and left at room temperature (normally deemed a safe storage procedure) for a few years.

[1] A. V. Dooglav, H. Alloul, O. N. Bakharev *et al.*, Phys. Rev. B **57**, 11792 (1998).

[2] P. Schleger, H. Casalta, R. Hadfield *et al.*, Physica C **241**, 103 (1995).

[3] W. Günther and R. Schöllhorn, Physica C **271**, 241 (1996); W. Günther, R. Schöllhorn, H. Siegle, and C. Thomsen, Solid State Ionics **84**, 23 (1996).

[4] I. Heinmaa, H. Lütgemeier, S. Pekker *et al.*, Appl. Magn. Reson. **3**, 689 (1992).

[5] D. E. MacLaughlin, A. P. Reyes, M. Takigawa *et al.*, Physica B **171**, 245 (1991).

[6] M. Abe, K. Kumagai, S. Awaji, and T. Fujita, Physica C **160**, 8 (1989); Y. Kohori, T. Sugata, H. Takenaka *et al.*, J. Phys. Soc. Jpn. **58**, 3493 (1989); Y. Yoshinari, H. Yasuoka, T. Shimizu *et al.*, J. Phys. Soc. Jpn. **59**, 36 (1990).

Anomalous electrodynamic response in the mixed-valence superconductor CeRu$_2$

N. E. Sluchanko,*) V. V. Glushkov, S. V. Demishev, N. A. Samarin, and I. B. Voskoboinikov

General Physics Institute, Russian Academy of Sciences, 117942 Moscow, Russia

O. D. Chystiakov

Institute of Metallurgy, Russian Academy of Sciences, 117334 Moscow, Russia

Y. Bruynseraede and V. V. Moshchalkov

Laboratorium voor Vaste-Stoffysica en Magnetisme, B-3001 Leuven, Belgium

We report the first results of microwave magnetoabsorption measurements (35–140 GHz) in the intermediate-valence superconductor CeRu$_2$. The anomalous electrodynamic response is found to derive from a transition from a weak to a strong pinning regime in the superconducting mixed state of this unusual metal. The experimental results strongly support the appearance in the CeRu$_2$ mixed state of a first-order phase transition that may be explained in terms of Fulde–Ferrel–Larkin–Ovchinnikov state formation. © *1999 American Institute of Physics.* [S0021-3640(99)01410-3]

PACS numbers: 74.60.Ec, 74.70.Ad, 74.25.Ha

1. Recently much attention has been drawn to the mixed state of the superconducting C-15 Laves phase compound CeRu$_2$, which exhibits an anomalous magnetic response in the vicinity of the upper critical field H_{c2} at temperatures $T \leqslant 0.9 T_C$ (Refs. 1–6). The unconventional peak effect is observed for samples of different origin,[2] including metallurgically clean samples and high-quality single crystals, contrary to the classical peak effect[7] studied extensively since the 1960s. The unconventional peak effect in CeRu$_2$ is very similar to that found in the heavy-fermion superconductors UPd$_2$Al$_3$ (Ref. 8) and UPt$_3$ (Ref. 9). However, contrary to the widely discussed unconventional superconducting state (SCS) with a multiple-component order parameter in UPt$_3$ (Ref. 10), the SCS in CeRu$_2$ may be interpreted in terms of a single-component order parameter (s-wave pairing) in the framework of the strong-coupling BCS model.[2]

The origin of the anomalous peak effect in CeRu$_2$ should be sought within the nature of the phase transition inside the mixed state. In particular, the Fulde–Ferrell[11] and Larkin–Ovchinnikov[12] models, in which the superconducting order parameter is spatially modulated as a function of magnetic field, can be used to consider the first-order phase transition between a weak and a strong pinning regime. More systematic studies of the peak effect, in particular, by means of direct and microscopic techniques, are needed to

reveal which intriguing pinning phenomenon accompanies this transition in the mixed state.

The electrodynamic response of type-II superconductors in the mixed state is strongly affected by vortex dynamics, as has been shown by extensive dc-transport and microwave-frequency studies of both low- and high-T_C superconductors.[13–15] Additionally it has been reported recently[16,17] that microwave magnetoabsorption (reflection) methods are very convenient experimental tools to study the magnetic phase transitions in Ce-based Kondo-lattice compounds.

The aim of the present work is to investigate the features of the unconventional pinning phenomenon. The electrodynamic response has been studied in the frequency range 35–120 GHz in magnetic fields up to 7 T for the normal and superconducting states of CeRu$_2$. For example, microwave magnetoabsorption measurements have been performed for frequencies well below the energy-gap value $(2\Delta \approx 4.0 k_B T_C)$[18] within the mixed state of the Ce-based superconductor. Simultaneously, direct measurements of the hysteretic peak effect and magnetic susceptibility have been carried out for the same samples of CeRu$_2$.

2. Polycrystalline samples of CeRu$_2$ were synthesized by the arc melting of stoichiometric amounts of the constituent elements $4N(99.99\%$ pure)-Ce and $3N(99.9\%$ pure)-Ru in an argon atmosphere. The sample was annealed in an evacuated quartz tube for two weeks at $900\,°C$. The longitudinal resistance was measured using dc four-probe techniques with isothermal magnetic field sweeps ($\mathbf{H} \perp \mathbf{J}$) at different rates.

Measurements of the microwave radiation power $P(H)$ absorbed in the sample were performed on a magnetooptical spectrometer[17] in a magnetic field up to 7 T. The microwave radiation sources used were BWT-generators ($\nu = 35$–140 GHz, about 10 mW output). The experimental setup allowed us to carry out magnetoabsorption measurements at temperatures of 1.8–4.4 K. The low-frequency-modulated ($f = 23$ Hz) radiation was transmitted by a waveguide into a cryostat containing a vertical magnet. A combination of waveguide accessories and movable quasioptical Teflon lenses was used to focus microwave radiation on the surface of sample. The polycrystalline CeRu$_2$ sample was mounted on a thin silver diaphragm located on the cold finger. A miniature carbon thermometer for detecting low-frequency-modulated microwave absorption was glued on the opposite (''dark'') surface of sample for better thermal contact. To avoid the influence of heat-release effects, different rates of magnetic field sweeps were used.

3. The family of resistivity $\rho(H)$ isotherms is shown in Fig. 1a for liquid-helium temperature and different current densities J in the interval 0–200 A/cm^2. The increase of J is accompanied by a dramatic elevation of the $\rho(H)$ amplitude in intermediate magnetic fields $H < H_{c2}$, and additionally the resistivity anomaly spreads out over a wide interval of magnetic fields (Fig. 1a). Contrary to the classical peak-effect phenomenon there is no ''peak-effect region'' for $H < 0.7$ T, which rules out the scaling-law behavior found empirically for the classical peak effect.[7] Moreover, the state I (Fig. 1b) is much more reversible than in the classical cases, for which the critical current remains everywhere at least a few percent of its value at the peak height. The electrical resistivity isotherms Fig. 1a and 1b are similar to the results obtained in Refs. 19 and 20 for thin films and polycrystalline samples of CeRu$_2$.

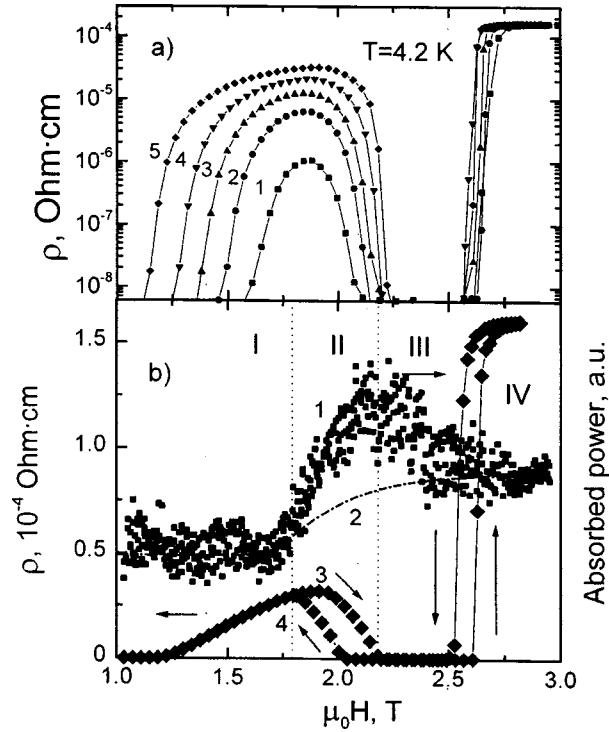The hysteresis in $\rho(H)$ (Fig. 1b, region II on curves *3–4*) is accompanied by the

FIG. 1. a) Magnetic field dependences of the resistivity $\rho(H)$ at liquid-helium temperature for different current densities: *(1)* $J=96.5$ A/cm², *(2)* $J=115.5$ A/cm², *(3)* $J=131.0$ A/cm², *(4)* $J=153.9$ A/cm², *(5)* $J=192.3$ A/cm². b) Magnetic field dependence of the microwave absorption ($\nu=45.43$ GHz, curve *1*) and resistivity isotherms $\rho(H,J=192.3$ A/cm²) (curves *3* and *4*) at liquid-helium temperature; I–III — superconducting state for weak and strong pinning regions, IV — normal state.

appearance of a substantial nonmonotonic microwave magnetoabsorption signal in the mixed state of CeRu₂. The typical field dependence of the microwave absorption at $T=4.2$ K is presented in Fig. 1b for $\nu\approx45.4$ GHz (curve *1*) together with magnetoresistance data $\rho(H,T=4.2$ K) for $J=192.3$ A/cm² (curves *2* and *3*). Note that hysteresis (region II in Fig. 1b) is always present at the onset of the anomalous pinning region, and hence the related nonmonotonic magnetoabsorption in the CeRu₂ mixed state (Fig. 1b, intervals II–III of curve *1*) can be regarded as a characteristic feature of a strong pinning regime below $H_{c2}(T)$.

In Fig. 2 we present the family of magnetoabsorption $P(H)$ curves obtained at different temperatures between 1.8–4.4 K for microwave frequencies of 37.2 GHz and 99.4 GHz. Note that the magnitude of the SCS $P(H)$ anomaly increases substantially as the temperature decreases, and at the same time an enlargement of the interval of this mixed-state electrodynamic response is also observed. To summarize the $P(H)$ data taken at different temperatures, we have plotted the characteristic parameters of the SCS magnetoabsorption (the initial H^* and final H_{c2} values of the $P(H)$ maxima) in Fig. 3a. The magnetic $H-T$ phase diagram deduced in the aforementioned manner from our microwave absorption data is presented in Fig. 3a. This phase diagram is in good agree-
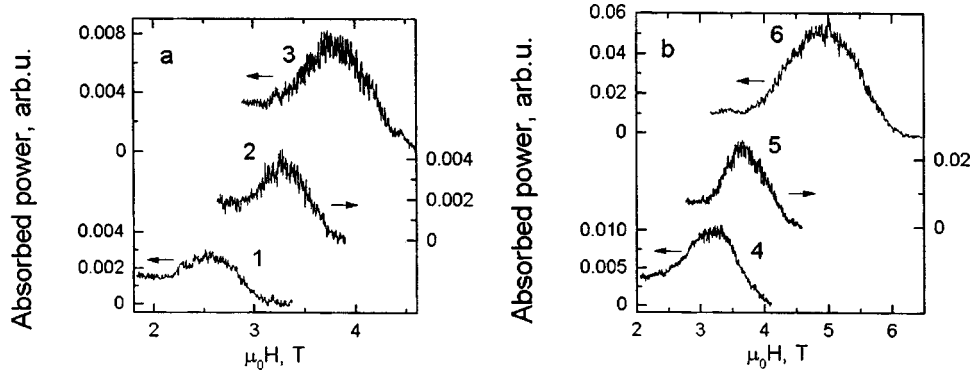
FIG. 2. Microwave magnetoabsorption in CeRu$_2$ in the mixed state for $\nu = 37.2$ GHz (a) and $\nu = 99.4$ GHz (b) at different temperatures: *(1)* 4.35 K, *(2)* 3.66 K, *(3)* 3.23 K, *(4)* 3.68 K, *(5)* 3.26 K, *(6)* 2.19 K.

ment with results published previously.[1–6] In addition, the temperature of the $P(H)$ maximum is plotted on the H—T plane (Fig. 3a).

It is well established for conventional type-II superconductors that microwave measurements are not hindered by pinning effects.[21] Since the depinning frequency is found to be in the MHz range for several low-T_C superconductors,[22,23] we can expect that for the SCS in CeRu$_2$ the microwave magnetoabsorption at frequencies 35–120 GHz, well below the energy gap $(2\Delta \approx 4.0 \ k_B T_C)$,[18] will contain basic information about the power absorption (the time-averaged rate of energy dissipation per unit area) and the penetration depth. However, the penetration depth usually varies monotonically with magnetic field and frequency,[19,24] and it is therefore natural to expect a smooth variation of $P(H)$ in the vicinity of the transition region (see curve *2* in Fig. 1b). Since experiment shows a strongly nonmonotonic behavior of the magnetoabsorption, the anomalous $P(H)$ peak in Figs. 1 and 2 can be attributed mostly to the effect of an additional power absorption during the phase transformation in the mixed state.

From this point of view it is very difficult to attribute our microwave magnetoab-
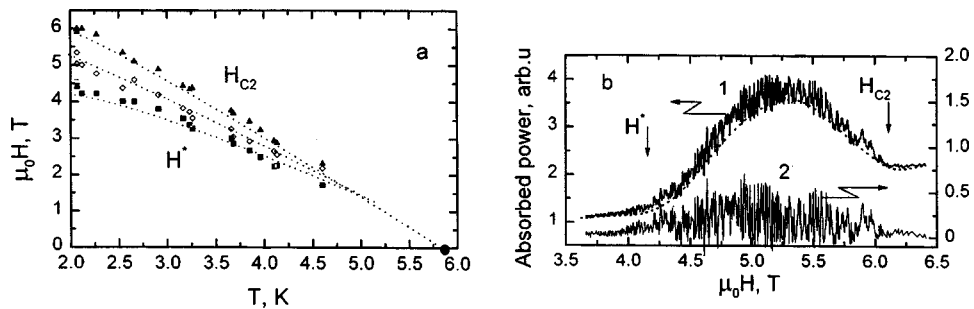

FIG. 3. a) Magnetic H–T phase diagram as deduced from $P(H,T_0)$ results obtained at different temperatures (1.8–4.4 K) and microwave radiation frequencies (35–120 GHz): ●—T_C value from the magnetic susceptibility measurements of the same CeRu$_2$ sample. b) Superconducting mixed-state anomaly of the microwave magnetoabsorption signal $P(H,T_0 = 2.12$ K), $\nu = 37.2$ GHz *(1)* and its ''fine structure'' *(2)* (see text).

sorption results (Figs. 2 and 3) to the presence of the microstructure containing slightly different superconducting characteristics, as was recently suggested for $CeRu_2$ from small-angle neutron scattering investigations.[25] Moreover, our x-ray diffraction measurements, together with the magnetic susceptibility and resistivity data and also preliminary results of Hall coefficient and thermopower experiments, allow us to consider the $CeRu_2$ samples investigated here as homogeneous superconductors with only a small variance of T_C (the detailed description of these results will be published elsewhere).

It is very interesting to note that there is an additional ''fine structure'' of the magnetoabsorption signal inside the interval $H^* \leq H \leq H_{c2}$, which can be interpreted in terms of an enhanced noise in the vicinity of the $P(H)$ maxima (Fig. 3b, curves *1* and *2*). In this situation one cannot rule out the appearance in the $P(H)$ signal of an additional contribution due to collective pinning effects arising from the presence of the superconductive layered structure consisting of periodic sheets with a vanishing order parameter perpendicular to the applied field.[26] Another possible explanation for the anomalous microwave magnetoabsorption (Figs. 2 and 3) could be the formation of a long-wavelength magnetic order which might also evolve with temperature and field, but at present there is not enough experimental evidence[27] to support this kind of interpretation.

To summarize, we have reported the first results of microwave magnetoabsorption measurements in $CeRu_2$ in the superconducting mixed state. An anomalous electrodynamic response is found in the frequency range (35–140 GHz), well below the superconducting gap in this intermediate-valence compound, and can be attributed to a transition from a weak to a strong pinning regime. The experimental results may be explained in terms of a first-order phase transition in the $CeRu_2$ mixed state, which is not inconsistent with the Fulde–Ferrel–Larkin–Ovchinnikov state formation in this unusual superconductor.

*)e-mail: nes@lt.gpi.ru

[1] S. B. Roy and P. Chaddah, J. Phys.: Condens. Matter **9**, L629 (1997).
[2] A. D. Huxley, C. Paulsen, O. Laborde *et al.*, J. Phys.: Condens. Matter **5**, 3825 (1993).
[3] H. Goshima, T. Suzuki, T. Fujita *et al.*, Physica B **206–207**, 193 (1995).
[4] R. Modler *et al.*, Phys. Rev. Lett. **76**, 1292 (1996).
[5] F. Steglich *et al.*, Physica C **263**, 498 (1996).
[6] K. Kadowaki, H. Takeya, and K. Hirata, Phys. Rev. B **54**, 462 (1996).
[7] A. M. Campbell and J. E. Evetts, *Critical Currents in Superconductors*, Taylor and Francis, London, 1987.
[8] K. Gloos, R. Modler, H. Shimanski *et al.*, Phys. Rev. Lett. **70**, 501 (1993).
[9] K. Tenya, M. Ikeda, T. Tayama *et al.*, Phys. Rev. Lett. **77**, 3193 (1996).
[10] L. Taillefer, J. Flouquet, and G. G. Louzarich, Physica B **169**, 257 (1991).
[11] P. Fulde and R. A. Ferrell, Phys. Rev. **135**, A550 (1964).
[12] A. I. Larkin and Yu. N. Ovchinnikov, Zh. Éksp. Teor. Fiz. **47**, 1136 (1964) [Sov. Phys. JETP **20**, 762 (1964)].
[13] M. W. Coffey and J. R. Chem, Phys. Rev. Lett. **67**, 386 (1991).
[14] M. Golosovsky *et al.*, Phys. Rev. B **50**, 470 (1994).
[15] S. Revenaz *et al.*, Phys. Rev. B **50**, 1178 (1994).
[16] G. Hampel, Phys. Rev. Lett. **72**, 3386 (1994).

[17] N. E. Sluchanko, S. V. Demishev, A. V. Semeno *et al.*, JETP Lett. **63**, 453 (1996).
[18] K. Matsuda, Y. Kohori, and T. Kohara, Physica B **223&224**, 166 (1996).
[19] N. R. Dilley, J. Herrmann, S. H. Han, and M. B. Maple, Physica B **230−232**, 332 (1997).
[20] D. Groten, S. Ramakrishnan, B. Becker *et al.*, Physica B **230−232**, 377 (1997).
[21] M. Tinkham, *Introduction to Superconductivity*, McGraw-Hill, New York, 1975.
[22] J. L. Gittleman and B. Rosenblum, Phys. Rev. Lett. **16**, 734 (1966).
[23] J.le G. Gilchrist and P. Monceau, Philos. Mag. **18**, 237 (1968).
[24] N. Belk, D. E. Oates, D. A. Feld *et al.*, Phys. Rev. B **53**, 3459 (1996).
[25] J. Suzuki, N. Metoki, Y. Haga *et al.*, Physica B **241−243**, 871 (1998).
[26] M. Tachiki, S. Takahashi, P. Gegenwart *et al.*, Z. Phys. B **100**, 369 (1996).
[27] A. D. Huxley, P. Dalmas de Reotier, A. Yaouanc *et al.*, Phys. Rev. B **54**, R9666 (1996).

The near-field effect in a quantum computer

O. N. Gadomskiĭ*) and Yu. Yu. Voronov

Ulyanovsk State University, 432700 Ulyanovsk, Russia

It is shown that in principle it is possible to write optical information on individual quasiresonant atoms in a concentrated system by changing the angle of incidence of an external light wave. © *1999 American Institute of Physics.* [S0021-3640(99)01510-8]

PACS numbers: 03.67.Lx

The near-field effect was predicted theoretically in Ref. 1, and its properties have been investigated in detail in certain boundary-value problems of classical,[2] nonlinear,[3] and quantum[4] optics. The crux of the method is that the self-consistent interaction of polarizing fields of closely arranged atoms substantially changes the field of these atoms at any point of observation located in the near or wave zone with respect to these atoms. This effect is the basis of the idea, advanced in Refs. 5 and 6, of using optical radiation to investigate the structure of small objects with linear dimensions $a \ll \lambda$, where λ is the wavelength of the light wave.[5,6] In Refs. 5 and 6 the interaction of a light wave whose wave vector was directed along an axis connecting two dipole atoms was studied. The microscopic field at the location of the atoms and the field in the wave zone, which, as shown in Refs. 5 and 6, depends strongly on the interatomic distance, the polarizability of the atoms, the frequency of the external field, and so on, was calculated. In the present letter it is suggested that the near-field effect be used to write information on individual atoms in a concentrated system of two-level atoms by varying the angle of incidence of the external light wave. To demonstrate this method we examine a system of two close quasiresonant atoms (small object) in the field of an intense light wave that can change substantially the inversion of the atomic states. We shall fix the location of each atom by means of a corresponding phase factor of the resulting microscopic field.

Three basic problems can be distinguished in a quantum computer.[7–9] **1.** Identifying in a system of atoms an individual qubit atom which carries definite information for a sufficiently long period of time. In the method of Ref. 9, which is based on the use of a system of cold atoms in optical traps, the qubit atoms are located at distances $a \ll \lambda$ and despite this, as will be shown below, they can be distinguished according to the magnitude of the field at the location of each qubit atom. As specific qubit atoms we can consider Cr^{3+} ions in ruby with energy relaxation time $T_1 = (4\omega_0^3 d^2/3\hbar c^3)^{-1}$, where $d = 4.8 \times 10^{-21}$ cgs esu is the transition dipole moment and ω_0 is the transition frequency, corresponding to the R_1 line in ruby.[10] **2.** Encoding information and performing basic logical operations. In the method proposed, this can be done by using different angles of incidence of an external light wave, which can be changed using acoustooptic or elec-

trooptic modulators. **3.** A method for reading information after the calculations have been performed. In our analysis probe radiation can be used for this purpose. It was shown in Ref. 5 that the near-field effect also occurs when a weak light wave acts on a system of dipole atoms, which were treated as Lorentzian oscillators.

We shall determine the microscopic field $\mathbf{E}(\mathbf{r},t)$ of a light wave at an observation point $\mathbf{r}$ at time t by the equation[3,11]

$$\mathbf{E}(\mathbf{r},t) = \mathbf{E}_I(\mathbf{r},t) + \sum_{j=1}^{2} \text{curl curl} \frac{\mathbf{p}_j(t-R/c)}{R_j}, \tag{1}$$

where $\mathbf{E}_I(\mathbf{r},t)$ is the intensity of the electric field of the external light wave propagating with the speed of light c and $\mathbf{p}_j$ is the induced dipole moment of the jth atom. The distance $R_j = |\mathbf{r}-\mathbf{r}_j|$, where $\mathbf{r}_j$ is the radius vector of the jth atom relative to the origin of the coordinate system, which is placed, for example, at the center of the first atom. The differentiation in Eq. (1) is performed with respect to the coordinates of the observation point.

Let us consider the interaction of atoms with the field of an external light wave

$$\mathbf{E}_I(\mathbf{r},t) = \mathbf{e}E_0 \exp(-i[\mathbf{k}_0 \cdot \mathbf{r} - \omega t]) + \text{c.c.} \tag{2}$$

where $\mathbf{e}$ is a unit polarization vector of the electric field, E_0 is the real amplitude of the wave, and ω and $\mathbf{k}_0$ are the frequency and wave vector ($k_0 = \omega/c$) of the external wave. Then we represent the dipole moment of the jth atom as

$$\mathbf{p}_j = (1/2)\mathbf{d}_j(u_j + iv_j)\exp(i\omega t) + \text{c.c.} \tag{3}$$

where $\mathbf{d}_j$ is the transition dipole moment between two chosen quantum states of the jth atom, and the quantities u_j and v_j satisfy the equations[3,10]

$$\dot{u}_j = -(\omega_{0j} - \omega)v_j - \frac{2}{\hbar}(\mathbf{d}_j \cdot \mathbf{E}_{0j}'')w_j - \frac{u_j}{T_2'},$$

$$\dot{v}_j = (\omega_{0j} - \omega)u_j + \frac{2}{\hbar}(\mathbf{d}_j \cdot \mathbf{E}_{0j}')w_j - \frac{v_j}{T_2'}, \tag{4}$$

$$\dot{w}_j = \frac{2}{\hbar}(\mathbf{d}_j \cdot \mathbf{E}_{0j}'')u_j - \frac{2}{\hbar}(\mathbf{d}_j \cdot \mathbf{E}_{0j}')v_j - \frac{w_j - w_0}{T_1},$$

where ω_{0j} is the resonance transition frequency in the spectrum of the jth atom, w_j is the inversion of the quantum states of the jth atom which are coupled by the resident transition, w_0 is the initial inversion, and T_1 and T_2' are relaxation times.[10] The quantities $\mathbf{E}_{0j}'$ and $\mathbf{E}_{0j}''$ are the real and imaginary parts of the amplitude of the electric field at the jth atom:

$$\mathbf{E}(\mathbf{r}_j,t) = (\mathbf{E}_{0j}' + i\mathbf{E}_{0j}'')\exp(i\omega t) + \text{c.c.} \tag{5}$$

This determines the system of equations that will be used to solve the self-consistent problem of the interaction of two dipole atoms with an external field.

We shall assume that the time elapsed from the moment the external field is switched on $t \gg T_1, T_2'$, i.e., all processes occurring in the system can be assumed to be

steady. This limitation makes it possible to express the atomic variables in terms of the field variables. Indeed, setting in Eq. (4) $\dot{u}_j = \dot{v}_i = \dot{w}_j = 0$ and solving the system of linear algebraic equations obtained we have

$$u_j = -w_0 \kappa T_2' \frac{(\omega_{0j} - \omega) T_2' (\mathbf{e} \cdot \mathbf{E}_{0j}') + (\mathbf{e} \cdot \mathbf{E}_{0j}'')}{\Delta_j},$$

$$v_j = w_0 \kappa T_2' \frac{(\mathbf{e} \cdot \mathbf{E}_{0j}') - (\omega_{0j} - \omega) T_2' (\mathbf{e} \cdot \mathbf{E}_{0j}'')}{\Delta_j}, \qquad (6)$$

$$w_j = w_0 \frac{1 + ((\omega_{0j} - \omega) T_2')^2}{\Delta_j},$$

where

$$\Delta_j = 1 + ((\omega_{0j} - \omega) T_2')^2 + \kappa^2 T_1 T_2' [(\mathbf{e} \cdot \mathbf{E}_{0j}')^2 + (\mathbf{e} \cdot \mathbf{E}_{0j}'')^2], \quad \kappa = 2d/\hbar.$$

In deriving these expressions we assumed that $|\mathbf{d}_1| = |\mathbf{d}_2| = d$, and the corresponding vectors are directed along the vector $\mathbf{e}$.

Let us place the origin of the coordinate system at the point $\mathbf{r}_1$. Then we obtain (0; 0; 0) for the coordinates of the first atom and (0; R; 0) for the coordinates of the second atom. Let us assume also that the vectors $\mathbf{k}_0$ and $\mathbf{e}$ lie in the yz plane, and φ is the angle between $\mathbf{k}_0$ and the y axis. Now, studying Eq. (1) only for observation points located on the atoms, we obtain the equations

$$E_{01}'^{(y)} + iE_{01}''^{(y)} = e^{(y)} E_0 + \frac{1}{2} B d (u_2 + i v_2) \exp(i k_0 R), \qquad (7)$$

$$E_{01}'^{(z)} + iE_{01}''^{(z)} = e^{(z)} E_0 + \frac{1}{2} A d (u_2 + i v_2) \exp(i k_0 R),$$

$$E_{02}'^{(y)} + iE_{02}''^{(y)} = e^{(y)} E_0 \exp(-i \mathbf{k}_0 \cdot \mathbf{r}_2) + \frac{1}{2} B d (u_1 + i v_1) \exp(i k_0 R),$$

$$E_{02}'^{(z)} + iE_{02}''^{(z)} = e^{(z)} E_0 \exp(-i \mathbf{k}_0 \cdot \mathbf{r}_2) + \frac{1}{2} A d (u_1 + i v_1) \exp(i k_0 R),$$

where $\mathbf{e} = (0; -\sin\varphi; \cos\varphi)$, $A = -1/R^3 - ik_0/R^2 + k_0^2/R$, and $B = 2/R^3 + i2k_0/R^2$. Substituting expression (6) into Eq. (7) we obtain a system of four complex nonlinear algebraic equations for the same number of variables.

In the calculations below we shall use the following values of the parameters in Eqs. (6) and (7):

$$T_1 = 10^{-3} \text{ s}, \quad T_2' = 10^{-8} \text{ s}, \quad d = 1.38 \times 10^{-18} \text{ cgs esu}, \quad R = 1 \text{ nm}.$$

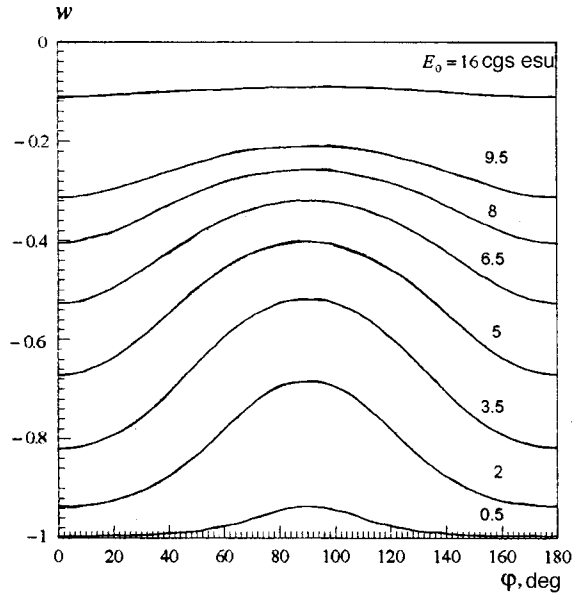We shall investigate the solutions of the system (7) for various values of the angle φ.

FIG. 1. Inversion on the atoms versus the angle for the case where the resonant frequencies of the atoms are the same, $k_0 = 9.985 \times 10^{-3}$ nm^{-1}, and the external field assumes a series of values.

CASE A. THE ATOMS POSSESS THE SAME RESONANT FREQUENCIES

Let $\omega_{01}/c = \omega_{02}/c = 0.01$ nm^{-1}. In this case, numerical calculations show that the inversions of the resonant levels on the first and second atoms have the same value. Figure 1 shows $w = w_1 = w_2$ versus the angle φ between the vector $\mathbf{k}_0$ and the y axis for various values of the amplitude of the external field. Changing the angle produces large changes of the inversion at the atoms, indicating the possibility of writing information on the atoms of a small object. As E_0 increases, the width of the writing region, i.e., the difference between the maximum and minimum values of the inversion, at first increases to approximately 0.3 and then decreases to 0. This property can be used to improve the quality of the writing. Large changes in w are possible only if k_0 differs from ω_{01}/c by not more than 10^{-4} nm^{-1}. However, if this difference becomes less than 10^{-6} nm^{-1}, then multistability appears: For fixed values of the parameters the system has more than one solution, the realization of any particular physical state being determined by the initial values of u_j, v_j, and w_j, i.e., the initial conditions. Figure 2 shows the corresponding dependences for this case. Two types of solutions are possible here. First, there are solutions for which the inversions on the atoms are different. Such solutions are possible for any angle. Second, for angles $0° < \varphi < 26°$ and $154° < \varphi < 180°$ there exist solutions with different values of the inversion on the atoms. This makes it possible to write nonidentical information on the atoms of a small object. It is important to note that, together with the solutions for which inversion on the first atom is greater than on the second atom, there exist solutions with the opposite ratio of the inversions. The existence of such solutions already follows from the form of the system (7). Indeed, since in our case $\mathbf{k}_0 \cdot \mathbf{r}_2 \approx 10^{-2}$, we can set approximately $e^{-i\mathbf{k}_0 \cdot \mathbf{r}_2} = 1$, and then it is easy to see that the system (7) transforms into itself when $\mathbf{E}_{01}$ and $\mathbf{E}_{02}$ are interchanged.
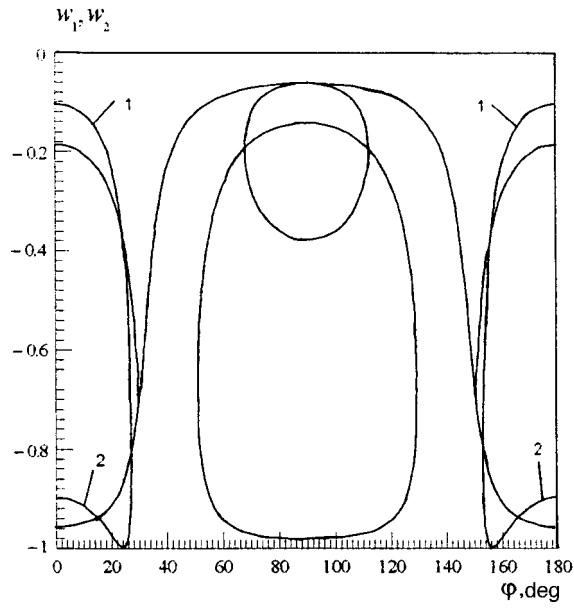
FIG. 2. Inversion on the atoms versus the angle for the case where the resonant frequencies of the atoms are the same, $k_0 = 9.999 \times 10^{-3}$ nm^{-1} and $E_0 = 0.5$ cgs esu. The branches 1 and 2 correspond to different atoms.
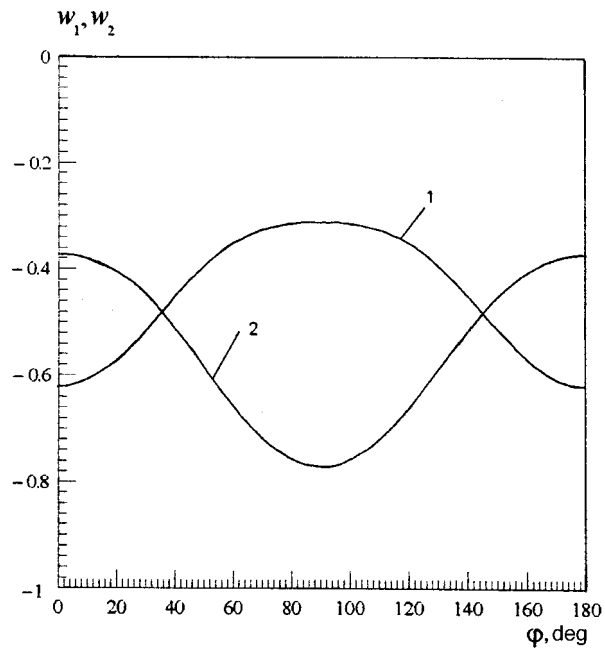

FIG. 3. Inversion on the atoms versus the angle for the case where the resonant frequencies of the atoms are different, $k_0 = 10^{-2}$ nm^{-1} and $E_0 = 4$ cgs esu. Curve 1 — inversion on the first atom, curve 2 — inversion on the second atom.

CASE B. THE ATOMS HAVE DIFFERENT TRANSITION FREQUENCIES

Let $k_0 = 0.01$ nm^{-1}, while $\omega_{01}/c = (1-10^{-3})k_0$ and $\omega_{02}/c = (1+10^{-3})k_0$. Then (Fig. 3) the inversions on the atoms are different for all angles except angles at which the plots of the angular dependences of the inversions intersect. This shows that it is possible to write nonidentical information on the atoms of a small object using the entire angular range. It should be noted that this method of writing becomes impossible when the difference of the resonant frequencies is large.

In summary, it has been shown in this letter that the near-field effect makes it possible to change the inversion of the individual atoms of a concentrated system in a wide range of values depending on the angle of incidence of the external wave. Only the stationary solution of the equations of motion (6) was used to show only the fundamental possibility of writing information on individual atoms. The optimal method for encoding information on individual atoms by varying the angles of incidence of the writing light beams can be chosen by decreasing the transition dipole moment, thereby increasing the time T_1, and using the impulsive solution of equations (6).

We thank K. A. Valiev, for calling our attention to the possibility of using the near-field effect in a quantum computer, as well as the participants of the scientific seminar at the Physicotechnical Institute of the Academy of Sciences for a helpful discussion of this possibility.

*)e-mail: qed_group@mail.ru

---

[1] O. N. Gadomskiĭ and K. V. Krutitskiĭ, Zh. Éksp. Teor. Fiz. **106**, 936 (1994) [JETP **79**, 513 (1994)].

[2] O. N. Gadomsky and K. V. Krutitsky, J. Opt. Soc. Am. B **13**, 1679 (1996).

[3] O. N. Gadomskiĭ and S. V. Sukhov, Kvantovaya Élektron. (Moscow) **25**, 529 (1998).

[4] O. N. Gadomskiĭ and S. G. Moiseev, Zh. Éksp. Teor. Fiz. **113**, 471 (1998) [JETP **86**, 259 (1998)].

[5] O. N. Gadomskiĭ and Yu. Yu. Voronov, Zh. Prikl. Spektrosk., in press.

[6] O. N. Gadomskiĭ and Yu. Yu. Voronov, Zh. Prikl. Spektrosk., in press.

[7] P. A. Benioff, Int. J. Theor. Phys. **21**, 177 (1982).

[8] R. P. Feynman, Found. Phys. **16**, 507 (1986).

[9] J. I. Cirac and P. Zoller, Phys. Rev. Lett. **74**, 4094 (1995).

[10] A. Allen and J. H. Eberly, *Optical Resonance and Two-Level Atoms* (Wiley, New York, 1975) [Russian translation, Atomizdat, Moscow, 1978].

[11] M. Born and E. Wolf, *Principles of Optics*, 4th edition (Pergamon Press, Oxford, 1969) [Russian translation, Nauka, Moscow, 1973].

Translated by M. E. Alferieff